MODELING AND EXPERIMENTAL VALIDATION OF ELECTRICAL CONDUCTIVITY AND PIEZORESISTIVITY OF CONDUCTIVE-FILLER-REINFORCED POLYMER NANOCOMPOSITES AND FOAMS

TRONG LINH HOANG

A dissertation submitted to the Faculty of Graduate Studies
in partial fulfillment of the requirements for the degree of
DOCTOR OF PHILOSOPHY

Graduate Program in Physics and Astronomy
York University
Toronto, Ontario
December 2020

ABSTRACT

Conductive-filler-reinforced polymer nanocomposite (CPN) has become increasingly popular because of the combined flexibility and low cost of the polymer paired with the enhanced electrical and mechanical properties of the conductive nano-filler. The presence of a conductive filler network is reconfigurable by applied strain. It can be used in sensors such as strain gauges (for example, force sensors, pressure sensors). This research seeks to identify the underlying mechanisms that govern the electrical and mechanical properties of CPN, both theoretically and experimentally. The study theoretically elucidates the electrical conductivity and experimentally demonstrates piezo-resistivity of CPN based on phase morphological structure as well as types of polymers and conductive fillers. Experiments with controlled processing conditions and material compositions of popular polymers and conductive fillers were conducted. Comparisons were made between the experimental and simulation results of nanocomposites' electrical conductivity. Consequently, adjustments were made to the simulation model until the experimental outcomes agreed satisfactorily with the simulation results. The selected fabricated samples are characterized in terms of their electrical conductivity and piezo-resistivity. Experimental results showed that the materials developed possess enhanced conductive networks and can be applied in the biomedical field where flexible non-invasive sensors can be worn outside the body to monitor vitals such as heart rate and movement.

DEDICATION

To my newborn son, Christopher.

ACKNOWLEDGEMENTS

I would like to express my sincere appreciation to many people for their supports and encouragement. I am grateful for funding from the Natural Sciences and Engineering Research Council of Canada (NSERC), and from York University.

First, I would like to thank my co-supervisors, Professor Zheng Hong (George) Zhu and Professor Siu N. (Sunny) Leung. Without their supervision and guidance, this dissertation would never have been possible. I will appreciate forever the knowledge shared and their recommendations when needed.

I also would like to thank Professor Anantharaman Kumarakrishnan for being my committee member and advising me during the research period and dissertation writing phase. Another thank is given to Dr. Jane Colwell for her language polishing service.

In addition, I am thankful for the fundamentals learned from Weiqing Fang (an M.Sc. graduate from Prof. Leung's group) and Dr. Shen Gong. My research models build on their work during the early stages of my research. Their findings and discussion assisted me with polymer-simulation during my studies. Next, I acknowledge the work done by many researchers in foaming models, particularly the works in [1, 2], which inspired me to develop comprehensively my foaming simulation models.

Furthermore, I want to extend thanks to my lab-mates and summer-students. The Ph.D. would have been more stressful and difficult without their kindness. In particular, I

warmly thank Mohammadmehdi Aghelinejad, Maryam Fashandi, Kyra McLellan for their assistance in several sub-projects of the research.

Finally, I am grateful to my family and friends who live in Canada and overseas. Living-aboard life is hard without their support and encouragement. My friends were there for me at all times and especially when I needed it the most. Especially, I need to thank Lena, Uncle Kim, and Aunty Tina for their enormous help.

Wish you all the best, faithfully.

TABLE OF CONTENTS

LIST OF TABLES

LIST OF FIGURES

LIST OF ABBREVIATIONS

ABS	Acrylonitrile butadiene styrene
CNT	Carbon nanotube
CPN	Conductive-filler-reinforced polymer nanocomposite
GNP, GnP	Graphene nanoplatelet
HDPE	High-density polyethylene
MWCNT, MW-CNT	Multi-wall carbon nanotube
PC	Polycarbonate
PP	Polypropylene
RVE	Representative volume element
$ScCO_2$	Supercritical carbon dioxide
SEM	Scanning electron microscopy
SWCNT, SW-CNT	Single-wall carbon nanotube
TPU	Thermoplastic polyurethane
vf. (vf.%)	Volume fraction (percentage)
vol.%	Volume fraction in percentage
wt. (wt.%)	Weight fraction (percentage)
σ	Electrical conductivity

Chapter 1 INTRODUCTION

Summary: This chapter presents an introduction to the application of CPNs and foams, which provides justification for the research activities, defines the research objectives, and outlines the research methodology. At the end, the structure of this dissertation is presented.

1.1 Conductive-filler-reinforced Polymer Nanocomposites and Foams

Polymers are popular and exist in many forms in modern life because it is cheap, lightweight, and can be made either rigid or flexible. Common types of polymers have good processability and are not electrically conductive. An insulating polymer can be turned into conductive polymer nanocomposites (CPN) by filling polymer matrices with conductive fillers such as carbon nanotubes (CNT) [3] and graphene nanoplatelets (GNP) [4] above a threshold loading [5] as illustrated in Figure 1.1.

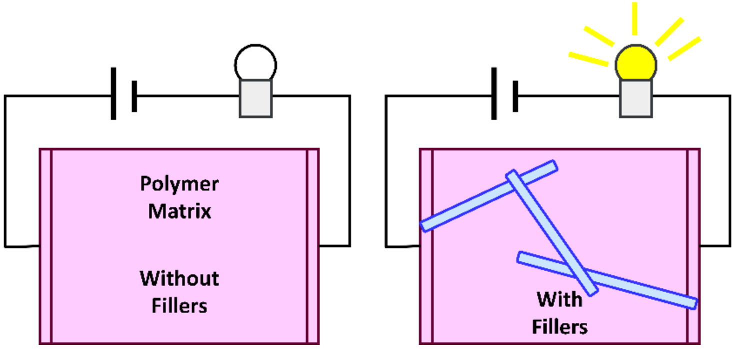

Figure 1.1 Demonstration of polymer turned to conductive by reinforcing with conductive fillers.

CNT, which possesses an extremely high aspect ratio, is a well-known effective filler for enhancing multifunctional properties of polymer nanocomposites such as sensitive temperature/strain sensors [6]; or electromagnetic-wave interference materials [7], at low loading. Similarly, graphene nanoplatelet is popular in reinforcing polymers [8] due to its low processing cost and high availability. These properties can further be improved by foaming the nanocomposites to control the alignments of CNT in the polymer matrix. In addition, nanocomposite foams are lighter than their solid counterparts and can lower the manufacturing cost by saving materials [9]. For example, using carbon dioxide (CO_2) to physically foam nanocomposites would alter the embedded conductive network, leading to a change in its electrical conductivity [10]. Figure 1.2 demonstrates the different configurations of fillers resulted from a different level of volume expansion during the foaming process. The foam cell, i.e., void space, can either promote or disrupt the conductive network and change the electrical conductivity of the nanocomposite. The direction of change in its electrical conductivity depends on the size and shape of the expanded void.

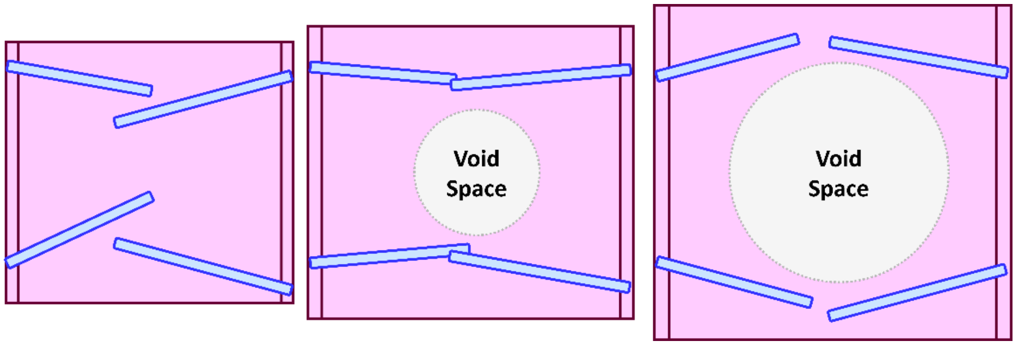

Figure 1.2 Configurations of fillers changed during the foaming process.

Furthermore, applying a mechanical strain to a conductive polymer nanocomposite would disrupt its conductive network, leading to a change in its electrical resistivity. This behaviour is commonly known as piezoresistivity, which is illustrated in Figure 1.3. Piezoresistive materials are very promising in the field of robotics (e.g., used in skin sensors) [11, 12]. Flexible polymers, such as thermoplastic polyurethane (TPU), are popular choices of matrix materials to fabricate nanocomposites due to their flexibility. At moderate loading of CNTs as the filler, the electrical conductivity of TPU can be improved, yet remain flexible [13]. These changes in material characteristics are one of the main focuses in this research.

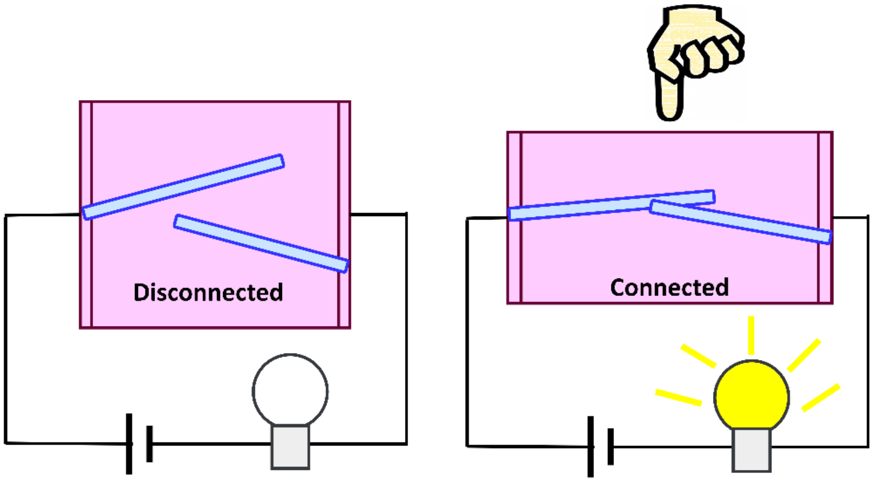

Figure 1.3 By applying a strain, i.e., pressing, on the material, the configuration of fillers changes and the material is conductive.

1.2 Justification of the Research

Understanding these extraordinary characteristics of polymer nanocomposites and the underlying processing-structure-property relationships are critical to both the research community and the industry. As a result, extensive research has been conducted both experimentally and theoretically. Various research has extended simple simulation models [14] to more sophisticated ones with the advancement in both assumptions and simulation methodologies such as CNT deformation consideration [15], and/or agglomeration effect [16], and they have been verified experimentally. In addition to electrical conductivity, these models are able to explain other behaviours such as piezoresistivity when a composite is being strained [17, 18], or electrical conductive property changes before and after foaming processes [19]. It is noted that these studies use different approaches to model the conductive CNT networks, leading to significant differences in the simulation results. Various discrepancies and underlying bias in existing models may also lead to uncertainty in the analysis of experimental results, especially at low loadings of CNT.

In the context of polymer nanocomposite foams, research was conducted by either visualizing or simulating the foaming process and to evaluate the foaming-induced alignments of fillers in the polymer matrix. However, existing theoretical research has mostly been conducted by only simulating the ultimate stage of foaming processes [19, 20]. In these studies, the pores were introduced in the polymer matrix before the generation of fillers in the numerical simulation. In other words, the evolution of the filler network caused by the bubble expansion has been neglected. Furthermore, the phase morphologies of polymer nanocomposite foams and the structures of the filler network are strongly dependent on many processing and material parameters. These include the types of polymer and blowing agents, the foaming temperature and pressure, as well as the stabilization process at the end of the foaming process. This leads to a wide variety of foam structures, which would significantly affect the electrical conductivity and the piezoresistivity of the polymer nanocomposite foams. Therefore, a new model that can account for the effect of foam expansion on filler alignment and dispersion and track the evolution of the phase morphologies during foaming is needed to advance the research in this field. While some of the recent researches have attempted to address this need [1, 2], these models consider the voids in the polymer nanocomposite foams to be spherical in shape. Such assumption is impossible to simulate the properties of polymer nanocomposite foams with high volume-expansion ratios. Scanning electron microscopy (SEM) has also revealed that the voids in polymer nanocomposite foams with high volume-expansion ratios are polyhedral. Therefore, it is critical to conduct research to fill such knowledge gap by developing a modified simulation model in order to elucidate the processing-structure-property relationship of these multifunctional materials.

1.3 Objectives of the Research

The objectives of this study are to investigate, both theoretically and experimentally, the mechanical and electrical properties of CPNs and their foams. This research develops a modified simulation model that can address the challenges and limitations of existing simulation models and methodologies. The developed models are verified by experimental results of CPNs and their foams fabricated under various experimental conditions. An overview of the research methodology of this research is illustrated in Figure 1.4. The research uses two parallel streams to cross-validate theoretical simulations with experimental testing.

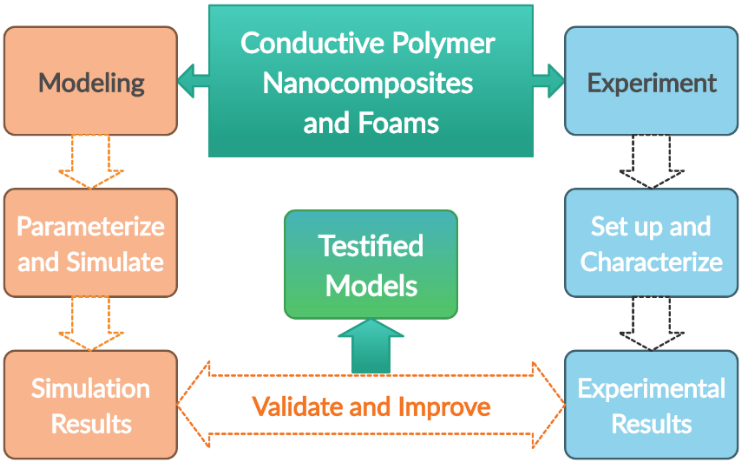

Figure 1.4 Model methodology.

- **Modeling**: Develop models to characterize electrical properties of CPNs and their foams; modify models to improve the precision and eliminate biases in simulations. In the foaming process, the model takes into account high-volume-expansion-ratio cases. Multiple simulations are configured based on factual dimension determined experimentally.
- **Experimenting**: Fabricate and characterize samples and compare experimental results with simulation results for both foamed and unfoamed polymer nanocomposites.
- **Validating**: Analyze experimental measurements to compare, inform and enhance various theoretical models.
- **Application**: Fabricate CPNs and foams and use a dynamic mechanical analyzer to

reveal the predictive piezoresistive properties of the fabricated materials, and to demonstrate their potentials use in force/pressure sensors.

1.4 Methodology

The initial phase of this research was an investigation of common biases when using universal hypotheses in modeling CPNs. At first, conventional models of electrical conductivity of CPNs were investigated to inspect the model biases and consider how to eliminate them. Next, foaming effects were modeled based on different volume-expansion ratios, and models were developed to simulate the electrical conductivity of the nanocomposite foams. In particular, this research focuses on developing a modified model to investigate nanocomposite foams with high volume-expansion ratios, which has never been reported in existing literature to my best knowledge.

Since safety was a priority for the experimental activities, the conductive-polymer-nanocomposite masterbatches, instead of dry MWCNT powders, were chosen and diluted to desired MWCNT loadings by the melt-compounding technique. In particular, commercially available HDPE/MWCNT nanocomposite masterbatch, loaded with 15 wt.% MWCNT, and neat HDPE were melt-compounded to prepare HDPE/MWCNT nanocomposites of lower MWCNT loadings. In addition, carbon dioxide (CO_2) was used as the physical foaming agent in this study to introduce voids in the nanocomposites, which could reduce material consumption and therefore reduce the carbon footprint to the environment. This technique was used throughout this thesis research, and the method of the foaming process was thermodynamic instability. The solid samples were, at first, soaked and saturated with CO_2 at high pressure and temperature. The gas was then rapidly released, leading to a thermodynamic instability, and resulted in cell nucleation and the growth of CO_2 bubbles in the polymer nanocomposite matrix.

1.5 Outline of this Dissertation

The dissertation is subdivided into eight chapters. Following the introduction and justification of this thesis research in Chapter 1, a detailed literature review of the CPNs and the state-of-the-art modeling of their electrical conductivity is conducted in Chapter 2. Then, the modeling of CPNs is presented in Chapter 3, including the technical challenges and the approaches developed in this research to eliminate the common biases. A foaming model is reported in Chapter 4 to set up the initial hypothesis to simulate the foams of CPNs at low and high volume-expansion ratios. In particular, modified foaming modeling was developed to handle foams with high volume-expansion ratios, which had never been reported in the literature to my best knowledge. Chapter 5 presents experimental studies that help to validate and improve the models. The electrical conductivity of fabricated nanocomposite samples, with and without foams, were characterized and the results were compared with theoretical models in Chapter 6. Following the electrical conductivity studies, the piezoresistivity of nanocomposites and their foams is considered in Chapter 7 to evaluate their applications as sensors. Finally, Chapter 8 concludes the contribution of this work and some future research directions in this field.

Chapter 2 LITERATURE REVIEW

Summary: The literature on CPNs and foaming in both experimental and simulation modeling are reviewed. Modeling approaches of solid CPNs and their foams are evaluated and discussed.

2.1 Conductive-filler-reinforced Polymer Nanocomposites

Conductive-filler-reinforced Polymer Nanocomposites (CPNs), including, polymer/carbon nanotube (CNT) nanocomposites, are of interest to researchers and industry because of their low density, superior chemical resistance, good manufacturability, and tunable multifunctional properties. This versatile material system has been used in a wide spectrum of applications including electromagnetic interference shielding [21-23], energy harvesting [24-26], energy storage [27, 28], sensing [6, 18, 29], thermal management [30-32], force/pressure sensors [12, 33, 34], smart wearable textiles and flexible electronics [35-38], and thin-film transistor [39]. CNT's exceptionally high intrinsic electrical conductivity (σ) and high aspect ratio make it an ideal filler to prepare CPNs.

Recent studies have suggested foaming polymer nanocomposites as a promising fabrication strategy to tailor their micro-and-nanostructures. Through foaming-induced biaxial stress fields, it is possible to align both one-dimensional (1D) and two-dimensional (2D) multifunctional fillers and thereby enhance the mechanical [40-42], electrical [42, 43], and thermal [44, 45] properties. The foaming process can be conducted by using physical foaming agents such as supercritical carbon dioxide (ScCO$_2$) [46], microspheres expanded under high temperature [47], or chemical foaming agents, such as AIBN [22], which decomposes and releases nitrogen gas under high temperature.

The electrical conductivity of a polymer/CNT nanocomposite can be drastically improved once its CNT loading has been increased above a critical level, denoted as percolation threshold (p_c). While high CNT loading promotes nanocomposites' electrical conductivity, it is detrimental to the weight, processability, and mechanical properties of polymer/CNT nanocomposites. Extensive studies were conducted to develop strategies for promoting polymer/CNT nanocomposite's electrical conductivity with lower CNT loading and to investigate the effects of CNT's dispersion, alignment, and aspect ratio on CPN's σ and p_c, which is the minimum CNT loading to initiate long-range connectivity among them [48-50]. These include the utilization of hybrid conductive fillers with distinct types, sizes, and/or shapes as well as using immiscible polymer blends. Park et al. [23] investigated the effect of hybrid fillers on the electrical conductivity of the polypropylene (PP) composite. In their investigation, the inclusion of both MWCNT and carbon fiber in the PP matrix led to higher electrical conductivity than those filled solely with carbon fiber. In another study [51], acrylonitrile butadiene styrene (ABS) was melt-blended with polycarbonate (PC)/MWCNT nanocomposite. Due to the partial solubility of ABS in PC, the selective dispersion of the MWCNTs in the ABS phase significantly promoted the electrical conductivity while reducing p_c.

2.2 Modeling Conductive-filler-reinforced Polymer Nanocomposites

Extensive theoretical studies were conducted to improve the fundamental understanding of the structure-to-property relationships of CPNs filled with CNT. They commonly modelled CNT as random resistor networks in a polymer matrix. A representative volume element (RVE), usually cubic, was used to model the CPNs by simplifying the CNT conductive networks as if they follow a periodic pattern [15, 52]. CNT are randomly assigned their positions and orientations in the RVE. Any CNTs that protrude out of the RVE's boundary surface are cut and relocated to point into the RVE from the opposite boundary surface.

Despite the periodic assumption, the size of RVE has been identified as a governing factor to the accuracy and efficiency of the simulation. Hu *et al*. used a relatively large cubic RVE (i.e., dimension ~5 times the CNT length (L_{CNT})) to help achieve numerical convergence [52], but a larger RVE would increase the computational demand. This led to a challenge in simulating CPNs with high CNT loadings. In this context, Bao *et al.* considered periodically connective paths on each pair of opposite boundary surfaces of RVE [14]. Fang *et al*. proposed a two-box RVE model to account for the interconnectivity of CNT across the boundary surface between two adjacent RVE [53]. Both approaches could reduce the size of RVE without compromising simulation accuracy. While most numerical studies adopted the "cut-and-relocate" approach to assign CNT into the RV, the potential biases and impacts induced by such approach have yet to be investigated. The present work aims to fill this gap and provide guidance to eliminate these biases.

2.3 Foaming Model Approaches

Although modeling solid CPNs has been broadly studied and the results have explained the variety of applications of CPNs, the foaming models of CPNs have not been researched comprehensively. Foaming CPNs can be classified into two classes derived from the changes in their morphologies, low and high volume-expansion ratios. Volume-expansion ratio is defined as the ratio of the volume of a foamed sample to that of an unfoamed sample.

At low expansion, the shapes of voids are spherical because the foam cells do not interfere with each other during the foaming process. Using a simple cubic (SC) model to describe the distribution of spherical foam cells in the polymer matrix, the maximum volume-expansion ratio is 2.1 times (note: the ratio of the volume of the spherical void to the total volume of the cubic foam is $\boldsymbol{\pi/6}$**).** However, considering the cases of other closely packing schemes (e.g., face-centred cubic (FCC) and hexagonal close packing (HCP)), the maximum ratio spherical void's volume to the total volume is $\boldsymbol{\pi/3\sqrt{2} \approx 0.74}$. This represents a foam with a maximum volume-expansion ratio up to 3.9 times [54, 55]. The illustrations of these maximum values of expansion ratios are presented in Figure 2.1. These volume-expansion ratios are smaller than most of the nanocomposite foam samples fabricated in this study, which ranged between 5 and 20 times. Throughout this dissertation, a volume-expansion ratio over 3.9 times is considered to be a high volume-expansion ratio, which cannot be realistically modelled by considering the voids to be spherical. Details of the experimental studies in the characterization of samples' volume expansion can be found in Section 5.4: Effects of Foaming Conditions on Volume-Expansion Ratios

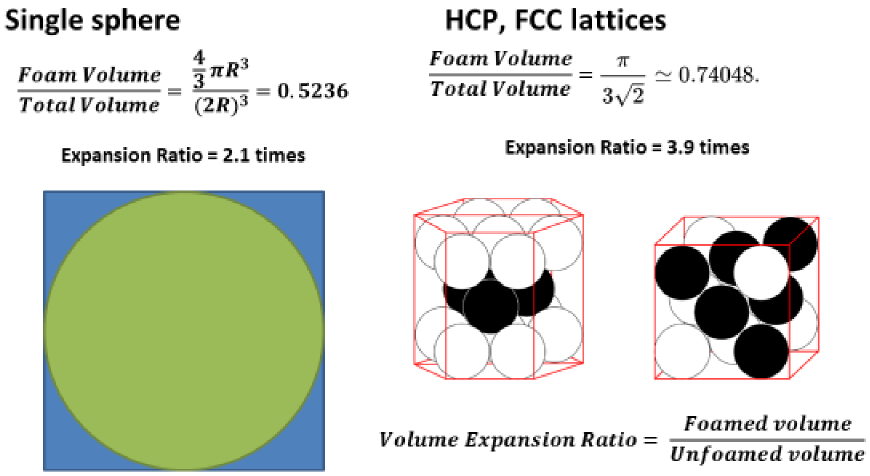

Figure 2.1 Maximum values of volume-expansion ratio in cases of spherical model

In the existing literature, the sizes of voids in polymer nanocomposite foams are on a comparable scale to the length of conductive fillers, making it possible to be modeled and simulated with manageable computational resources [19, 56, 57]. In the existing literature, a common approach to model the dispersion of MWCNT in polymer nanocomposite foam was to randomly introduce these conductive fillers in the matrix of a foamed structure such that the fillers would not penetrate into the cell walls. The distribution of fillers was not uniform because of the restricted generation of fillers. Since MWCNT was introduced into a structure with pre-existing voids, these models could not simulate the realistic situation and did not provide any information about the evolution of the MWCNT network structures during the foaming process. As a result, a significant knowledge gap exists in the use of foaming technology to alter the electrical conductivity of nanocomposite foams. Recently, some researchers have tracked the translational and rotational motions of fillers during foaming based on the incompressible property of a polymer matrix [1, 2]. However, the dependence of electrical conductivity on the micro-and-nanostructures of CPN foams was not simulated. The existing technology gap has led to the motivation of this dissertation to develop new approaches to simulate the dependence of the electrical conductivity of CPN foams on their volume expansion behaviours during the foaming process. The details about the development of such new simulation approaches are reported in Chapter 4: Modeling Foaming of CPNs.

Furthermore, existing literature has not reported any theoretical studies of the electrical conductivity of CPN foams with high volume-expansion ratios. It is believed that there exist two major challenges that hinder researchers from such theoretical studies. These challenges include the large dimension of a representative volume that can simulate the CPN foam structure and the difficulty to handle the motion of fillers during foam expansion. First, the dimension of a foam cell is much larger than the average length of the fillers. This would lead to a severe demand on computing power in the simulation work. Second, as the volume-expansion ratio increases to 3.9 times, the expanding voids are closely packed. Further expansion would lead to the interference of these expanding cells and thereby result in the distortions of their shapes in polyhedral (i.e., cubic, octahedral, or dodecahedral). Such interference would affect both the translational and rotational motions of the fillers, leading to additional challenges in related theoretical studies.

In this study, modified models were developed to overcome these challenges. The incompressible property of the material is used as a basis to simulate the fillers before and after the foaming process and is applied for modeling at both low and high volume-expansion ratios.

2.4 Experimental Validation

Experimental validation is a critical step to develop models of CPNs and foams to simulate the effects of their structures on their electrical conductivity. To address this, experiments were set up to fabricate and characterize samples in order to provide data to verify the simulation results obtained theoretically.

Experimental verification of simulation results was widely conducted by theoretical researchers for both unfoamed and foamed polymer nanocomposites. For the case of unfoamed nanocomposites, theoretical simulation of the electrical conductivity of polymer nanocomposites filled with CNTs had been validated by experimental studies using polymer nanocomposites with various matrix materials such as epoxy resins [16, 52, 58], polystyrene (PS) [56, 57], polypropylene (PP) [2, 59]. In contrast, the theoretical studies for polymer nanocomposite foams were limited and were focused on foams with low volume-expansion ratios. Experimental verifications were done by characterizing polymer nanocomposite foams prepared by different foaming techniques, including high-pressure foam injection molding [2, 59], chemical blowing agent [56], and salt leaching method [57]. In other words, there exists a clear technology gap regarding the theoretical studies about the effect of foam morphology on the evolution of the conductive network during foam expansion and the resultant electrical conductivity of the foams with a high volume-expansion ratio. In particular, this research would use high-density polyethylene (HDPE)/multi-walled carbon nanotube (MWCNT) nanocomposites and their foams as case examples for the study to fill the aforementioned knowledge gap. Supercritical carbon dioxide ($ScCO_2$) would be used as the physical foaming agent. The outcomes of this research would provide insights to elucidate the processing-structure-property relationship of polymer nanocomposite foams with high volume-expansion ratios.

Chapter 3 MODELING CONDUCTIVE-FILLER-REINFORCED POLYMER NANOCOMPOSITES AND BIASES

Summary: This chapter reports the modeling of CPNs in terms of their electrical conductivities. The difficulties in simulations and the underlying biases in the common simulation approach found in existing literature have been discussed. As a result, a modified simulation approach is being suggested to avoid biases.

3.1 Introduction

Challenges to accurately model the electrical conductivity of carbon-nanotubes (CNT)-polymer nanocomposites include the need for high computational power [14, 58]. A common approach to circumvent this challenge is by using a small cubic representative volume element (RVE) to simulate CNT conductive network in a polymer matrix [14, 52, 53, 58, 60]. By assuming these networks follow a periodic pattern, researchers [14, 52] cut any randomly dispersed CNT that protrudes outside the RVE and relocated it to point into the RVE from the opposite boundary surface of the element. Representing dispersed CNT by a random resistor network, Monte Carlo simulations revealed that this "cut-and-relocate" approach led to significantly higher CNT concentration in the proximity of RVE's walls and shorter CNT length [61]. These biases result in an inaccurate representation of CNT-polymer nanocomposites and affect the simulated electrical conductivity [61]. This work focused on effective strategies to eliminate the biases and to improve the accuracy in modeling of CNT/polymer nanocomposites.

3.2 Technical Challenges

The simulation programs are developed from a program coded by Weiqing Fang during his master's studies, supervised by Professor Siu N. Leung and reported in [17, 53]. Originally, the program was preliminary and limited. It could not perform a high loading of CNTs due to the enormous size of the RVE and was only verified using experimental studies of unfoamed polymer nanocomposites.

In this research, distinct boundary conditions were implemented to inspect the effect of tube generation on the formation of resistor networks because of the finite size of RVE while mimicking the actual CPNs. Furthermore, the program was optimized in the resistor-network finder and conductance-matrix solver to improve the performance. Most importantly, models that represent polymer nanocomposite were developed to investigate the effect of the experimental process on the nanocomposite's electrical conductivity. To validate the models, simulation parameters (e.g., size of diameter and length of CNT) were set to be consistent with those observed from the experimental studies.

3.3 Percolation Threshold of Electrical Conductivity

Experimental measurements of the electrical conductivity of conductive-filler/polymer nanocomposites were found to follow the trend predicted by the exponential percolation theory [62, 63]. The percolation-threshold value p_c of the MWCNT nanocomposites, which is the minimum MWCNT loading that would transform the nanocomposites from insulating to conductive, was estimated by fitting the percolation model (i.e., Equation **(3.3.1)**) to the experimentally obtained electrical conductivity data.

$$\boldsymbol{\sigma = \sigma_0 (p - p_c)^t} \tag{3.3.1}$$

where σ is the electrical conductivity of the nanocomposite and *p* is the volume fraction of MWCNT; σ_0, p_c, and *t* were fitting coefficients and achieved by curve fitting using the root-mean-square-error method. The critical exponent *t* is relevant to the system dimensionality. For example, in the system of three-dimension, the *t* value is expected to be 2 [64, 65].

3.4 Modeling Conductive-filler-reinforced Polymer Nanocomposites

3.4.1 Simulation Volume

MWCNT nanocomposites were modeled by using the conventional cubic RVE and the two-box RVE [53]. The dimensions of a cubic RVE or each box in the two-box RVE were denoted as $\boldsymbol{L_x}$, $\boldsymbol{L_y}$, and $\boldsymbol{L_z}$, where electrodes were on the opposite boundary surfaces across the x-axis and illustrated in Figure 3.1. The flow of electric current is considered propagating from the left boundary surface (i.e., high voltage electrode) to the right boundary surface (i.e., low voltage electrode) that is parallel to the x-axis. Consequently, the y- and z-planes are perpendicular to the current flow. The RVE is started from the origin (i.e., O (0, 0, 0)) in the coordinate system spans towards the positive directions of individual coordinate axes. In a two-box RVE model, the other child (i.e., the bottom RVE) spans towards the negative direction of the z-axis.

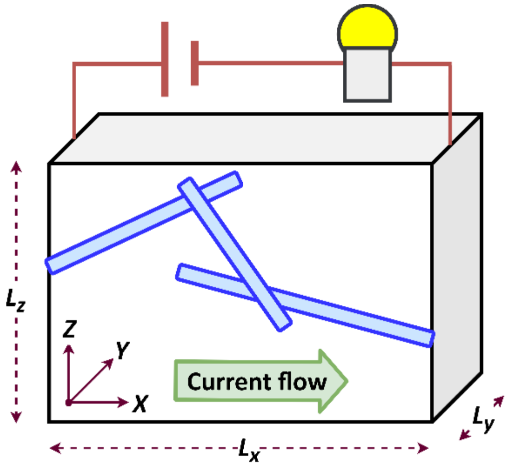

Figure 3.1 Schematic of randomly dispersed CNTs.

3.4.2 Tube Generation

Each MWCNT was modeled as a rigid rod and its position was represented by a line segment in the three-dimensional Cartesian coordinate system. The length of CNT was approximated by a Weibull distribution [66]. A random function was used to determine the starting coordinates as well as the azimuthal and polar angles of the line segment [17, 53] as displayed in Figure 3.2. This mimicked the random distribution of MWCNT.

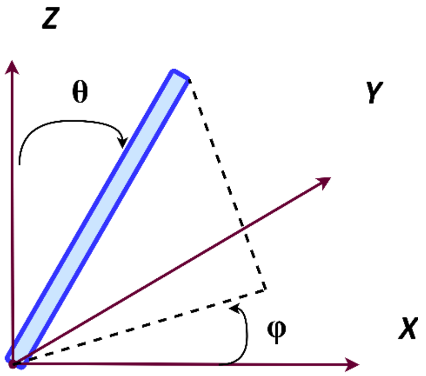

Figure 3.2 The generation of tube in coordinate system.

In the generation of a tube, the first endpoint is created randomly P_1 (x_1,y_1,z_1) within the RVE, equivalently, produced in Equation **(3.4.1)** where ***rand*** is the uniform-distributed-random function which generates randomly between 0 and 1.

$$x_1 = L_x \times rand \tag{3.4.1a}$$

$$y_1 = L_y \times rand \tag{3.4.1b}$$

$$z_1 = L_z \times rand \tag{3.4.1c}$$

Next, the other endpoint P_2 (x_2,y_2,z_2) is generated based on the generation of $\cos(\theta) = 1 - 2\times rand$ and angle $\varphi = 2\pi\, rand$

$$x_2 = x_1 + L_{CNT} \times \sin(\theta) \times cos(\varphi) \tag{3.4.2a}$$

$$y_2 = y_1 + L_{CNT} \times \sin(\theta) \times \sin(\varphi) \tag{3.4.2b}$$

$$z_2 = z_1 + L_{CNT} \times \cos(\theta) \tag{3.4.2c}$$

where L_{CNT} is the length of the CNT; φ is the azimuthal angle; and θ is the polar angle. To let CNTs occupy evenly and uniformly in space, the **cos(θ)** is generated uniformly instead of **θ**. Depending on the distribution of length of CNTs, the L_{CNT} can be fixed or different from each other.

3.4.3 Boundary Condition Handling

Simulations based on the cubic RVE were conducted with or without using the "cut-and-relocate" approach. When this approach was used [14, 52], any MWCNT protruding outside the RVE was cut and relocated to another opposite wall-side. In contrast, simulations based on the two-box RVE were done only by the "cut-and-remove" approach where any outside MWCNT was cut and just removed (i.e. ignoring the outer parts) [17, 53]. Figure 3.3 (a) through (c) illustrate the schematics for the original randomly distributed MWCNT in a polymer matrix, and the resultant distribution after either the "cut-and-relocate" or "cut-and-remove" approach has been adopted.

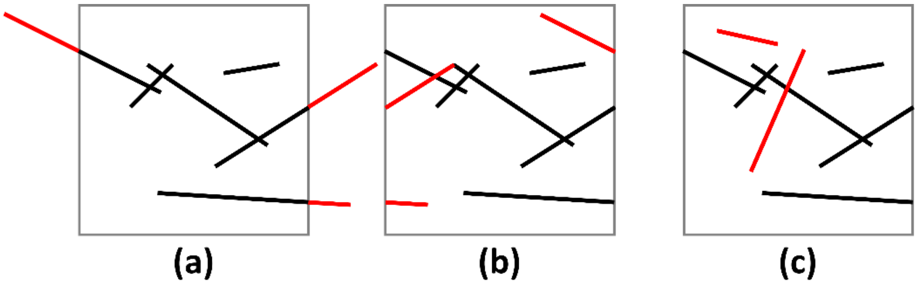

Figure 3.3 Schematics of randomly distributed MWCNT in a polymer matrix:

(a) initial random assignment;

(b) "cut-and-relocate" approach for protruded MWCNT; and

(c) "cut-and-remove" approach for protruded MWCNT replaced by new random MWCNT.

3.4.4 Identification of the Resistor Networks and Calculation of Resistance

In simulations, all interconnecting MWCNT that bridged the two electrodes in the

RVE were identified to be part of the random resistor network. The network consisted of two types of resistances as illustrated in Figure 3.4: (i) intrinsic resistance ($\boldsymbol{R_{int}}$) along a MWCNT; and (ii) contact resistance ($\boldsymbol{R_{cont}}$) between two interacting MWCNT [17, 53]. Equations **(3.4.3)** and **(3.4.4)** express the mathematical models to determine the $\boldsymbol{R_{int}}$ along individual MWCNT and $\boldsymbol{R_{cont}}$ at the junctions between interconnecting MWCNT which can be estimated by solving the Schrodinger equation with a rectangular potential barrier or from the Wentzel–Kramers–Brillouin approximation [67, 68]. Two MWCNT are considered connecting with each other when the shortest distance between them is shorter than the cut-off distance ($\boldsymbol{d_{cutoff}}$). Detailed mathematical models and simulation procedures to determine these resistances can be found in reference [53, 69, 70].

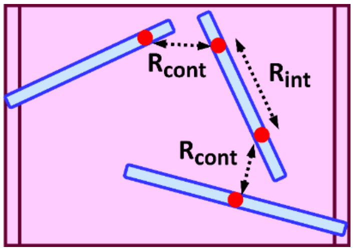

Figure 3.4 Types of schematic connections in resistor networks formed by connected CNTs.

$$\boldsymbol{R_{int} = \frac{4l}{\pi\sigma_{CNT}D^2}} \tag{3.4.3}$$

$$\boldsymbol{R_{cont} = \frac{h}{2e^2}\frac{1}{MT}} \tag{3.4.4a}$$

$$\boldsymbol{T = \begin{cases} exp\left(-\dfrac{d_{vdw}}{d_{tunnel}}\right) & for\ 0 \le d \le D + d_{vdw} \\ exp\left(-\dfrac{d-D}{d_{tunnel}}\right) & for\ d \le \left|D + d_{cutoff}\right| \end{cases}} \tag{3.4.4b}$$

$$\boldsymbol{d_{tunnel}} = \frac{\boldsymbol{h}}{2\pi}\frac{\mathbf{1}}{\sqrt{\mathbf{2}\boldsymbol{m_e}\Delta\boldsymbol{E}}} \qquad \mathbf{(3.4.4c)}$$

where $\boldsymbol{\sigma_{CNT}}$ is the intrinsic electrical conductivity of a nanotube itself, $\boldsymbol{h}$ is the Planck constant, $\boldsymbol{e}$ and $\boldsymbol{m_e}$ are the charge and mass of an electron, $\boldsymbol{D}$ is the diameter of a nanotube, $\boldsymbol{M}$ is the number of conduction channels, $\boldsymbol{d}$ is the distance between CNTs, $\boldsymbol{d_{vdw}}$ is the minimum distance between any pair of tubes which are separate by repulsive Van der Waals force, and is $\Delta\boldsymbol{E}$ the height of energy barrier when an electron jumps from a tube to another tube, hence, $\boldsymbol{T}$ is the electron transmission probability.

To simplify, the following terminologies are used to describe the process of simulation. First, a **node** in a network is the junction of any two tubes that are sufficiently close to each other, i.e., smaller than the cut-off distance $\boldsymbol{d_{cutoff}}$. Next, a **cluster** is a group of nodes in which an electron can move from a tube to other tubes within the group. A **conductive path** is represented by a set of nodes that forms a conductive path connecting the two terminals. In other words, it is a cluster that connects the two electrodes.

3.4.5 Convergence Check of Iteration

The simulation was performed under the Monte Carlo method, meaning the electrical conductivity is the average value of many trials. In each trial, the simulation starts with the generation and distribution of tubes in polymer matrices and ends with the calculation of electrical conductivity. After a trial, the convergence of outcomes is checked before terminating the simulation. Despite the fact that the error reduces by a factor of $1/\sqrt{N}$ where N is the number of trials [71]; the standard deviation was determined to observe its fluctuation over time. For nanocomposites loaded with a high volume-fraction of MWCNT, the fluctuation among different trials was small and the average electrical conductivity calculated from the trials approached to a constant value after hundreds to thousands of iterations. In contrast, for composites loaded with a low volume-fraction of MWCNT (i.e., close to percolation threshold), due to the frequent occurrence of trials that did not possess any continuous conductive path that bridged the two electrodes, the required number of trials to achieve convergence could surge to tens to hundreds of thousands of trials. Figure 3.5 (a) and (b, c) illustrate the change of average electrical conductivity versus the number of simulation trials for the two aforementioned cases.

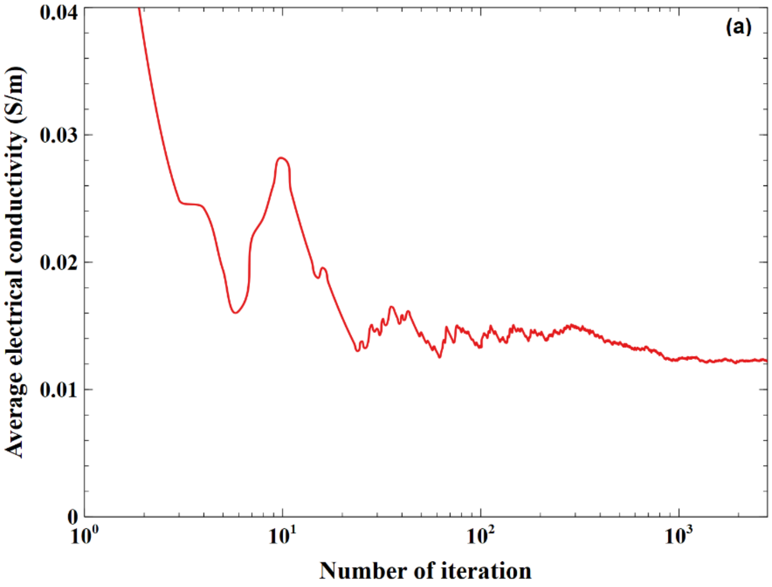

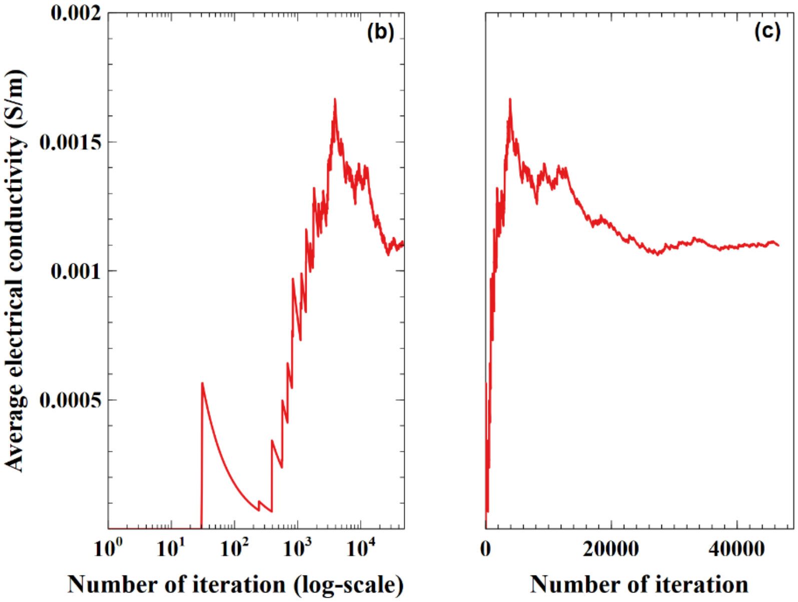

Figure 3.5 Average value of electrical conductivity over iterations at cases of (a) high vf. and (b) low vf. in both log-scale and (c) normal-scale axes of iterations.

3.4.6 Summary

Figure 3.7 illustrates a schematic that describes the flow of the simulation program, including how the program initializes input parameters and runs, as well as how outcomes are checked for convergence. The input configurations refer to the input parameters of the simulation program, which are based on experimental values and relevant reported values from literature. The input parameters refer to the choice of boundary condition and other parameters such as volume-fraction, aspect-ratio of fillers, or scale of RVE. In each simulation trial, a desired loading of MWCNT is first generated and distributed randomly in the RVE. Consequently, the program searches and identifies all nodes on cut-off distance and the resistance of resistor clusters were then calculated. Based on these clusters, matrices of conductance values are constructed to be solved and converted to conductivity derived from the dimension of the RVE. Finally, a determination of convergence is made for the simulation result by calculating its average value and evaluating its standard deviation in which the Monte Carlo method is implemented.

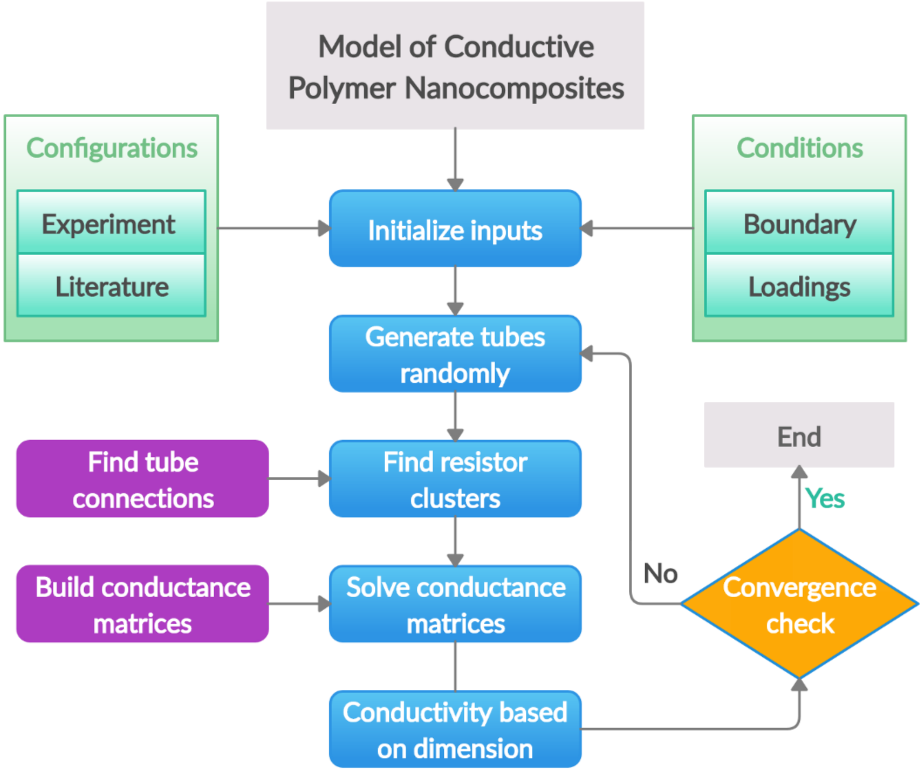

Figure 3.6 Flow chart of simulation program modeling CPNs.

3.5 Biases in Simulation and Improvements

3.5.1 Dimension of Simulation Volume

In general, a larger RVE would help to improve the precision and accuracy of simulation but it also leads to a surge in the required computational power. Therefore, in order to relax the demand in computational power, this study investigates the effect of the length dimensions of the RVE in the x, y, and z-directions on the predicted electrical conductivity of the nanocomposites. Simulation results using RVEs with different sizes are plotted in Figure 3.7 and compared with experimental data reported by Y. Ono et al. [72] and N. Grossiord et al [73]. Lx5.0_Ly2.0_Lz2.0 means the size of RVE [$\boldsymbol{L_x}$, $\boldsymbol{L_y}$, $\boldsymbol{L_z}$] is in a scale of [5.0, 2.0, 2.0] times of $\boldsymbol{L_{CNT}}$ in the three orthogonal directions. It is observed that the simulation results have a higher dependence on the length scale in the x-direction than on the y- or z-direction. Therefore, the electrical conductivity could be simulated precisely with lower computational cost by reducing the length dimensions in the y- and z-direction while keeping that in the x-direction to be at least five times longer than the length of MWCNT.

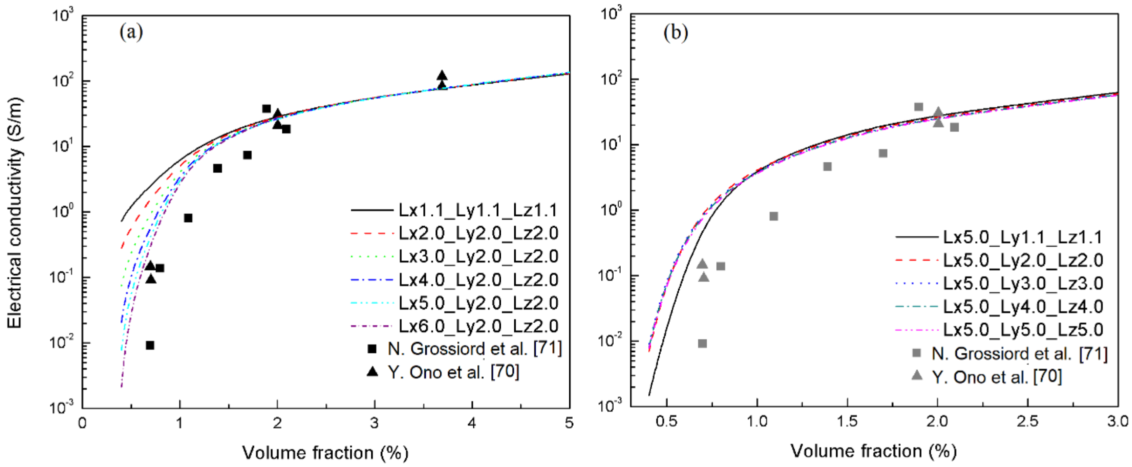

Figure 3.7 Effect of dimension of RVE on electrical conductivity where (a) variation of x-axis; and (b) variation of y- and z- axes. Lx1.1 means the $L_x = 1.1 \times L_{cnt.}$

3.5.2 Boundary Conditions

Figure 3.8 (a) through (d) compare the simulated MWCNT's length distributions and the number of nodes (i.e., the interacting junction of MWCNT) in the resistor network per unit volume, respectively, based on different approaches of boundary conditions and RVE's sizes. It can be observed in Figure 3.8 (a) and (b) that a smaller RVE size would significantly reduce the MWCNT length in CPNs loaded with either 0.5 vf.% or 3 vf.% MWCNT. The "cut-and-relocate" approach would also slightly reduce the average MWCNT length. Figure 3.8 (c) shows that at 0.5 vf.% MWCNT, by increasing the RVE's size, it significantly reduced the node density because of the lower probability for the MWCNT network to span over a longer distance. Although the "cut-and-relocate" approach led to the shortest average MWCNT length, the simulated node density was in fact slightly higher than the result obtained from the "cut-and-remove" approach. It is believed the severe bias in the number of nodes on the electrodes when adopting the "cut-and-relocate" approach compensated for the lower probability of shorter MWCNT to create a conductive network. Therefore, despite the similar final simulated node density, the biased phase morphology gave a false representation of CPNs and would lead to a problematic interpretation of simulation results and fundamental understanding.

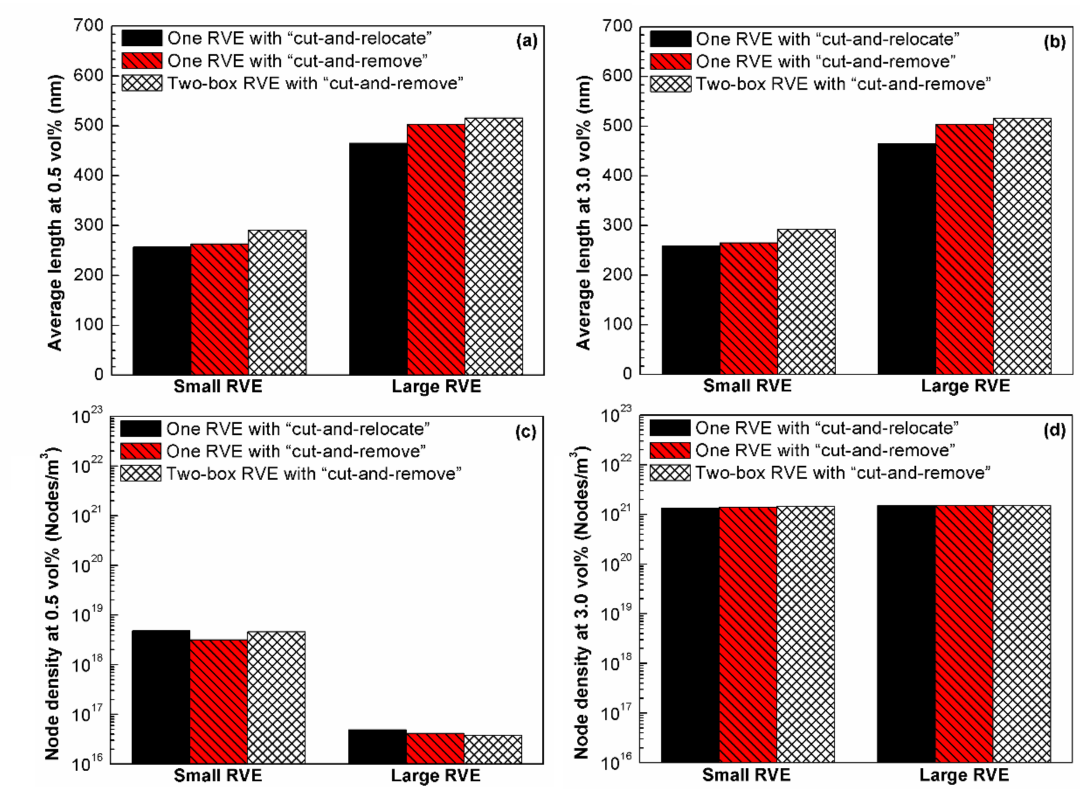

Figure 3.8 Average MWCNT length in RVE loaded with different MWCNT: contents

(a) 0.5 vf.% and (b) 3 vf.%;

and number of nodes per unit volume of RVE loaded with different MWCNT contents:

(b) 0.5 vf.% and (d) 3 vf.%.

[Note: $L_x = L_y = L_z = 1.1 \times L_{CNT}$ *and* $5 \times L_{CNT}$ *in small RVE and large RVE, respectively.*

Most importantly, Figure 3.9 (a) indicates that at low MWCNT loading (e.g., ≤ 0.6 vol.%), the simulated σ obtained from the “cut-and-relocate” approach was an order of magnitude higher than those obtained by the “cut-and-remove” approach. This confirms the significant impact made by the bias of high MWCNT concentration in the proximity of the boundary walls. Figure 3.9 (b) reveals that the “cut-and-relocate” approach also doubled the number of conductive paths per unit volume. Since CPNs with low MWCNT loadings are an important class of multifunctional materials (e.g., piezoresistive CPNs), it is important to eliminate the biases caused by the "cut-and-relocate" approach in the simulation of CPN's σ.

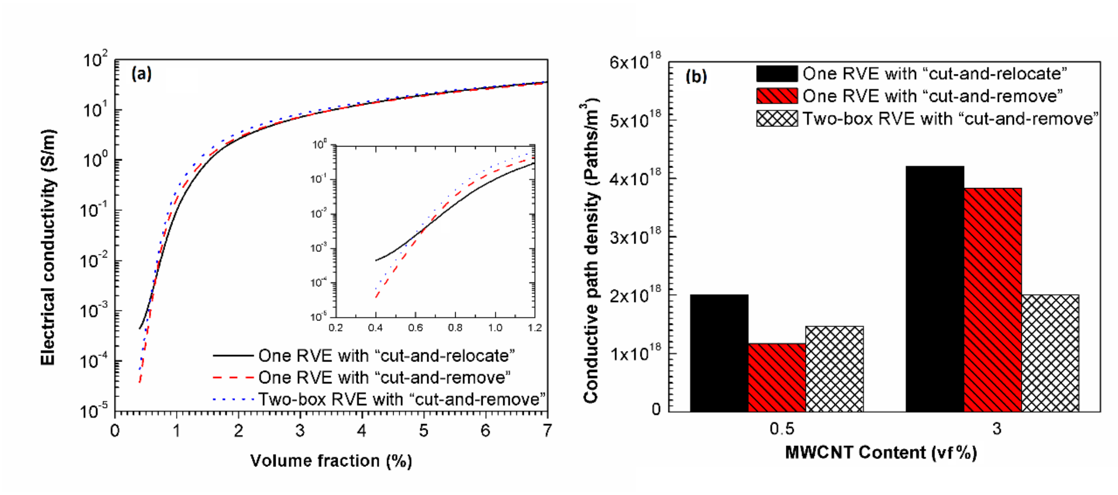

Figure 3.9 (a) simulated σ using the smallest RVE that yielded numerical convergence; and (b) simulated conductive path density using different models and MWCNT loadings.

3.5.3 Length Distribution of CNTs

The fixed length of filler is widely adopted in modeling fillers in CPNs, which simplifies the simulation and executes it faster. In fact, the length of CNT is not uniform and was accurately measured in [74-76] which was elucidated to obey the Weibull distribution [66]. The shape of the distribution looked like the Gaussian distribution, yet, there is a difference in the tail on the right of the Weibull distribution indicating that the length of CNT could be very long and it was difficult to measure the longest nanotubes [74]. The effect of length distributions on electrical conductivity in different models was graphed in Figure 3.10 which emphasizes the differences at low volume fractions. The

Weibull distribution generates adequate CNTs, which are long enough to form connections of CNTs between electrode terminals. These long CNTs impact explicitly on the “cut-and-relocate” model which relocates the part of CNTs generated out of RVE. Therefore, the length of tubes is retained and have greater chances to connect with other CNTs or electrode terminals, leading to an abnormal increase of electrical conductivity at extremely low volume fractions.

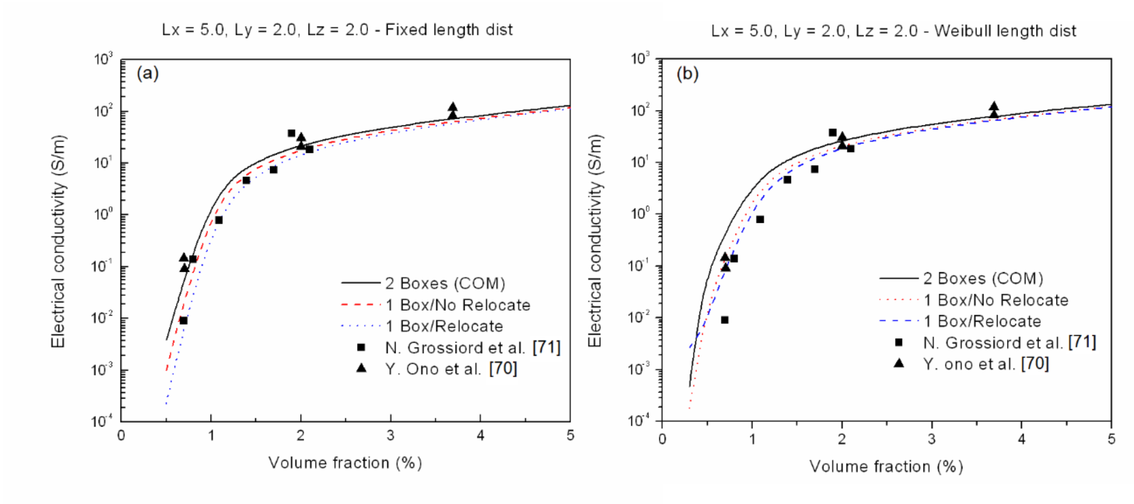

Figure 3.10 Effect of length distributions, including (a) fixed-length distribution and (b) Weibull distribution, on electrical conductivity in different models in a scale of RVE of [5.0, 2.0, 2.0].

Nevertheless, due to the finite size of RVE, there is a number of CNTs, generated randomly, which penetrate out of the RVE and need a boundary condition to handle these outer parts, causing the changes in length distribution of CNTs as plotted in Figure 3.11 and Figure 3.12. Figure 3.13 illustrates that the “cut-and-ignore” or “cut-and-remove”, i.e., CAI, model preserves the average length better than the “cut-and-relocate”, i.e., CAR. The breakage of CNTs creates more short tubes and the “cut-and-remove” approach leaves a chance for the next generated tube to have a longer length. Although the difference in electrical conductivity is minor, the impact of modified length distribution should be considered when simulating the CPNs.

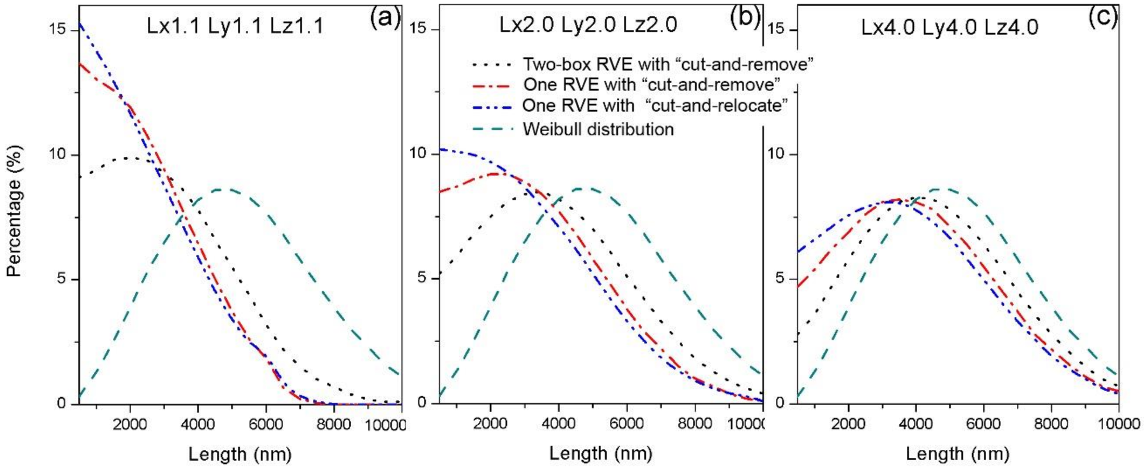

Figure 3.11 The comparisons of length distribution after generating tubes following the Weibull distribution in different scales of RVEs: (a) scale of [1.1, 1.1, 1.1], (b) [2.0, 2.0, 2.0], (c) [4.0, 4.0, 4.0]

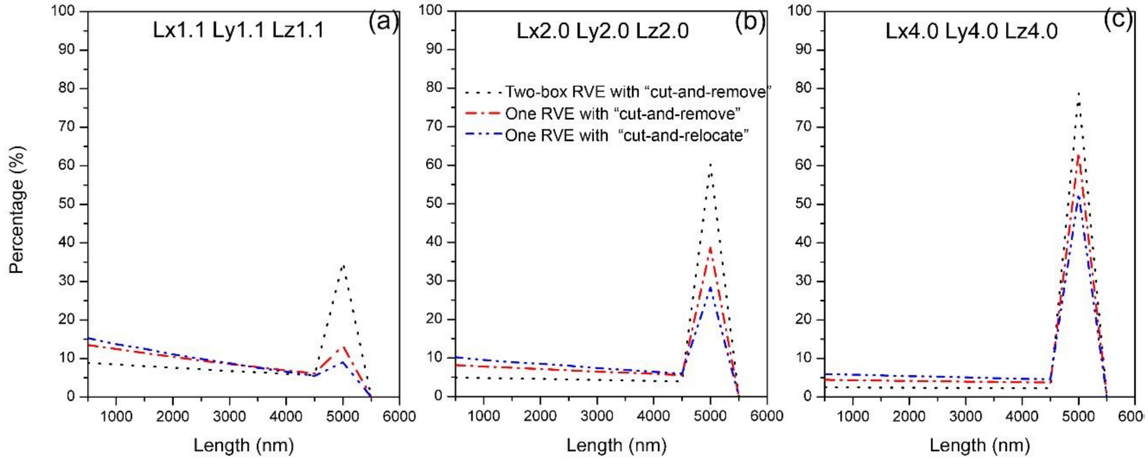

Figure 3.12 The comparisons of length distribution after generating tubes following the fixed-length distribution in different scales of RVEs:

(a) scale of [1.1, 1.1, 1.1],

(b) [2.0, 2.0, 2.0],

(c) [4.0, 4.0, 4.0].

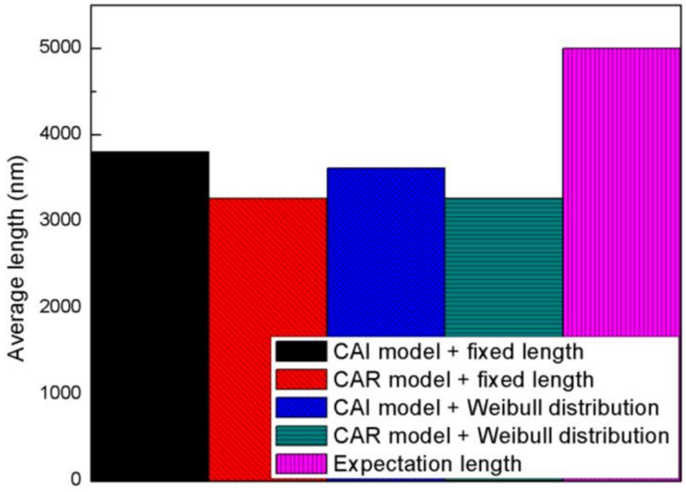

Figure 3.13 Average lengths depending on models and distributions at scale of [5.0, 2.0, 2.0]. CAI model is "cut-and-remove" model, CAR model is "cut-and-relocate" model.

Furthermore, the average value and distribution of CNT length were changed during the experiment process. For example, melt-compounding was revealed to manipulate the lengths of CNTs [77-79]. The shear forces developed during melt-mixing are enough to cause significant breakage of CNTs and reduction of length. Therefore, to accurately simulate CPNs, the length reduction of CNTs should be vigilantly considered and a new distribution of length should be established on experimental assessments.

3.6 Conclusions

A key challenge to model and simulate σ of the CNT-polymer nanocomposite is the excessive demand of computational power. This study finds that it can be eased by choosing an appropriate size of simulation volume for a particular volume fraction. This study also reveals that adopting the commonly used “cut-and-relocate” in simulation leads to the shortened CNT lengths. Nevertheless, the effects of CNT dispersion-related biases on simulation became predominant at low CNT loading. Furthermore, these biases would disregard the reliability of using numerical simulation to elucidate the structure-to-property relationship of CPNs.

Chapter 4 MODELING FOAMING OF CPNS

Summary: In this chapter, the models of foamed CPNs are constructed on the basis of the incompressibility of polymer matrices. Since the shapes of voids strongly depend on the volume-expansion ratios of the CPN foams, two models are used in the investigation. The first one, being used to simulate CPN foams with a low volume-expansion ratio, is based on an existing model reported in the literature. The second model, being used to simulate CPN foams with a high volume-expansion ratio, is newly developed in this research to fill the knowledge gap discussed in Chapter 2 of this dissertation. Furthermore, a solution to overcome the challenge caused by the high demand in computing power to conduct such studies is discussed.

4.1 Introduction

During the foaming experiment, the foam cells start from nuclei, and expand larger and larger over time due to the thermodynamic instability in the HDPE/MWCNT/ScCO2 system as illustrated in Figure 4.1. At the beginning of the expansion, the foam cells are free to grow radially. The growth is radial symmetric, leading to a spherical shape. However, as the foam cells continue to grow, they start to interfere with each other, and the expansions are constrained. Therefore, their shapes become polyhedron. These progresses were observed in images taken by scanning electron microscopy (SEM) technique for different volume-expansion ratios and also reported by other researchers

[80].

As a result, depending on the volume-expansion ratio of the polymer nanocomposite foams, different approaches would be required to realistically model and simulate them in order to predict their electrical conductivity. For foams with low volume-expansion ratios, the structures of foam cells are spherical [81]. In contrast, at high volume-expansion ratios, the structures are polyhedrons, which could be up to tetrakaidecahedron [80]. While existing literatures [1, 2, 19, 56, 57] have reported theoretical research of polymer nanocomposite foams with low volume-expansion ratios using a spherical model to represent the foam cell, theoretical research on polymer nanocomposite foams with high volume-expansion ratios has not been conducted due to the complication caused by the non-radial symmetry of the foam cells to my best knowledge. This represents a significant technology and knowledge gap to advance the understanding of the structure-to-property relationship of polymer nanocomposite foams. In other words, it leads to a strong motivation in this dissertation research to fill the knowledge gap.

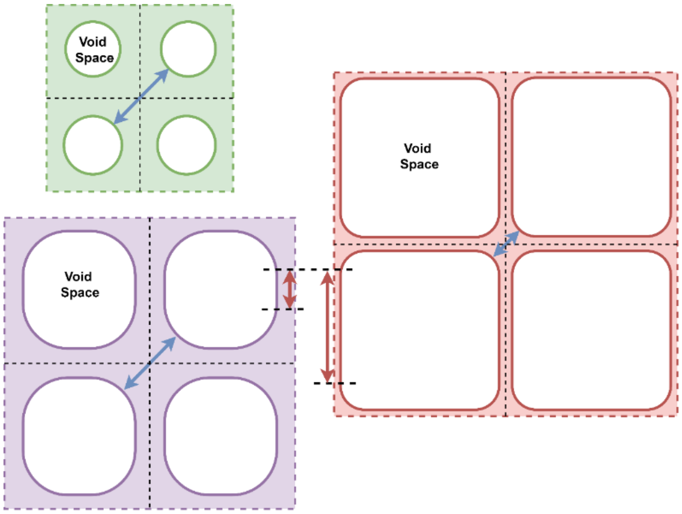

Figure 4.1 Schematic expansion of foam cells during foaming depending on the size of foam cells.

4.2 Hypothesis

For polymer nanocomposite foams with low volume-expansion ratios, the physical model (i.e., a spherical void in the polymer matrix) to represent such structures and phase morphologies and the underlying assumptions in the simulation were based on those reported in existing literatures [1, 2]. These assumptions are listed below:

(1) The tubes are rigid and do not slip over the adjacent polymer matrix during foaming;

(2) The midpoint of a tube is translated along a direction that connects the center of the spherical foam cell and the original midpoint of the tube before foaming;

(3) The new position of the tube is determined based on two modes of motion, i.e., translation of its midpoint and rotation about it;

(4) The dispersed tubes do not interact with each other during foaming;

(5) The tubes are always contained in the polymer matrix and would not penetrate into

the void after foaming;

(6) The polymer matrix is incompressible, and its volume remains unchanged during foaming;

(7) The foam cell structure is modeled as a closed structure.

It must be noted that the spherical model and the aforementioned assumptions reported in [1, 2] were only used in this dissertation for polymer nanocomposite foams with low volume-expansion ratio, in which the spherical cell possesses its radial symmetry during the foaming process. In contrast, for polymer nanocomposite foams with high volume-expansion ratios, the foam cells started to deviate from spherical shapes due to the interference of adjacent cells and become polyhedron. In order to more realistically represent such structure while keeping the simulation complexity to a manageable level, a new cubic model is developed and adopted in this dissertation. Due to the lack of radial symmetry in the cubic cell, additional assumptions would be needed to handle the simulation and the details are reported in Section 4.4 of this dissertation. Furthermore, new mathematical approaches have been developed in this work to not only simplify the simulation of the low volume expansion case but also to deal with the more complicated situation in the high-volume expansion case.

While research reported in [1, 2] only provided a proposed model to simulate the foaming-induced alignment of carbon nanotubes during the fabrication of polymer nanocomposite foams but did not predict the resultant electrical conductivity. A recent work [82] published in July 2020 (i.e., after the completion of the dissertation research) by the same research group applied the developed model to evaluate the electrical conductivity of polymer nanocomposite foams. Nevertheless, the study was restricted to polymer nanocomposite foams with low volume-expansion ratio that can be represented by the spherical model. Hence, developing a new model that can realistically simulate the case of polymer nanocomposite foams with high volume-expansion ratio represents an important research question. In other words, one key contribution in this dissertation is the development of such model to overcome the limitation of the existing models developed by other researchers. In particular, modeling polymer nanocomposite foams with high volume-expansion ratios and comparing the simulation results with experimental ones have been two of the main focuses in this dissertation.

4.3 Modeling Polymer Nanocomposite Foams at Low Volume-Expansion Ratios

At a low volume-expansion ratio, the growth of foam cells is radial symmetric. Thus, considering the incompressibility of the polymer, a CNT will be moved radially outward during foam expansion. Under this consideration, the volume of the polymer matrix remains unchanged while the spherical foam cell grows, and the outer radius of the polymer matrix increases. In the simulation, the final position of a CNT is determined by two steps [1,2]. First, the CNT is translated radially outward along a direction defined by connecting the center of the spherical RVE to the midpoint of the CNT. Then, the rotational motion of the CNT is governed by having the endpoints of the CNT to be coincident to the two concentric spherical shells that represent the boundaries of the polymer matrix with constant volume. A schematic that illustrates this idea is shown in Figure 4.2.

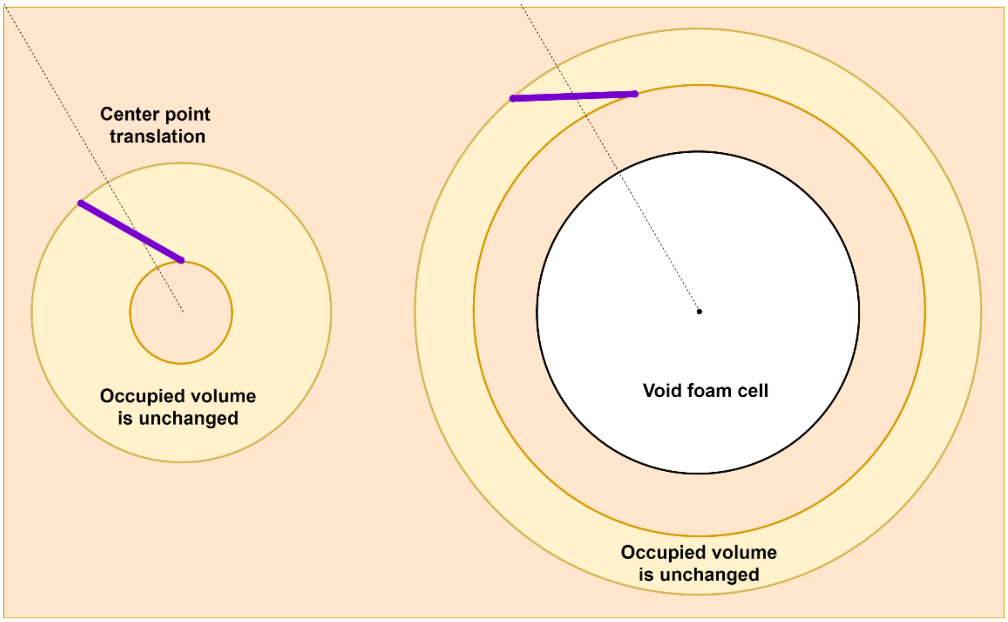

Figure 4.2 Model of spherical expansion for incompressible material at different stages.

The work reported in [1, 2] provided a mathematic solution to get the new position of a tube after foaming by considering the invariance of the polymer matrix's volume in three-dimensional space. Such approach gave a general solution yet required complicated reversal calculations to determine the new positions of CNTs. Moreover, it is not applicable to the cases of polymer nanocomposite foams with high volume-expansion ratios (i.e., polyhedron cells). Therefore, a new approach has been developed in this work to simplify the procedures to handle the mathematics and be applicable in the cubic model proposed in this work to simulate CPN foams with high volume-expansion ratios. In my approach, 3D coordinates of different characteristic points are first transformed into 2D ones. Then, the system of equations is solved in the 2D space, and the solutions are subsequently transformed back to the 3D space. The 2D plane used to solve the translational and rotational motion of the CNT contains the endpoints of CNT and the center of the foam cell (i.e., in both the spherical and cubic models). A detailed explanation of how to apply my new mathematical approach in a spherical model is described below.

Assuming the initial known parameters are the endpoints of the CNT (i.e., $\boldsymbol{P_1}$, and $\boldsymbol{P_2}$); the center of the foam cell (i.e., $\boldsymbol{P_c}$); the radius of the foam cell after foaming (i.e., $\boldsymbol{R_c}$). Based on these inputs, the final position and orientation of the tube can be determined, and these can be represented by the new endpoints of the tube (i.e., $\boldsymbol{P_{1N}}$ and $\boldsymbol{P_{2N}}$). These points are labelled in Figure 4.3.

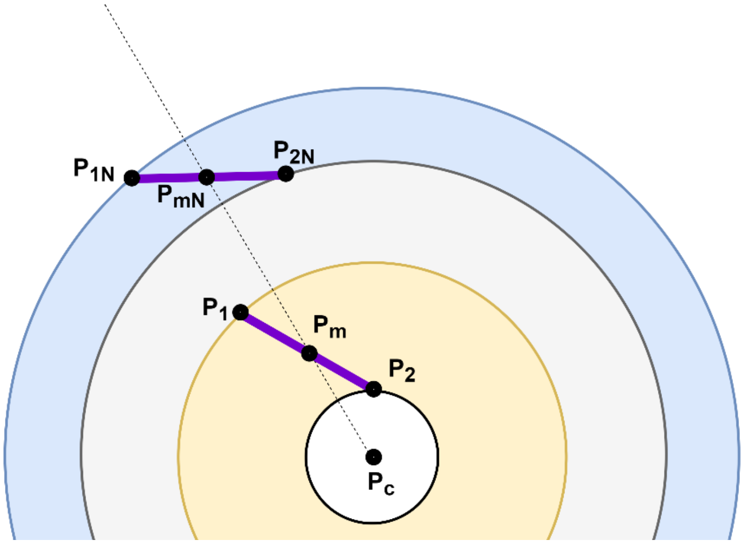

Figure 4.3 Labeled points in the spherical model.

Figure 4.4 illustrates the schematics that show a characteristic point of the spherical model before and after foam expansion. First, the midpoint of the tube can be found by

Equation **(4.3.1)**.

$$\boldsymbol{P_m = (P_1 + P_2)/2} \qquad \textbf{(4.3.1)}$$

The midpoint of the CNT is translated to the new position (i.e., $\boldsymbol{P_{mN}}$) upon foam expansion, during which the volume of the polymer matrix is unchanged. The invariant volume of the polymer matrix is described using Equation **(4.3.2)**:

$$\boldsymbol{\frac{3}{4}\pi R_{mN}^3 - \frac{3}{4}\pi R_c^3 = \frac{3}{4}\pi R_m^3} \qquad \textbf{(4.3.2)}$$

where $\boldsymbol{R_m}$ and $\boldsymbol{R_{mN}}$ are radii from the center of the foam cell to the midpoint of the tube before and after foaming, respectively.

Consequently, Equation **(4.3.2)** can be simplified and rewritten as

$$\boldsymbol{R_{mN} = \sqrt[3]{R_m^3 + R_c^3}} \qquad \textbf{(4.3.3)}$$

As a result, the new position of the CNT's midpoint (i.e., $\boldsymbol{P_{mN}}$) can be obtained from the radial translation of $\boldsymbol{P_m}$ for a distance of $\boldsymbol{R_{mN}}$.

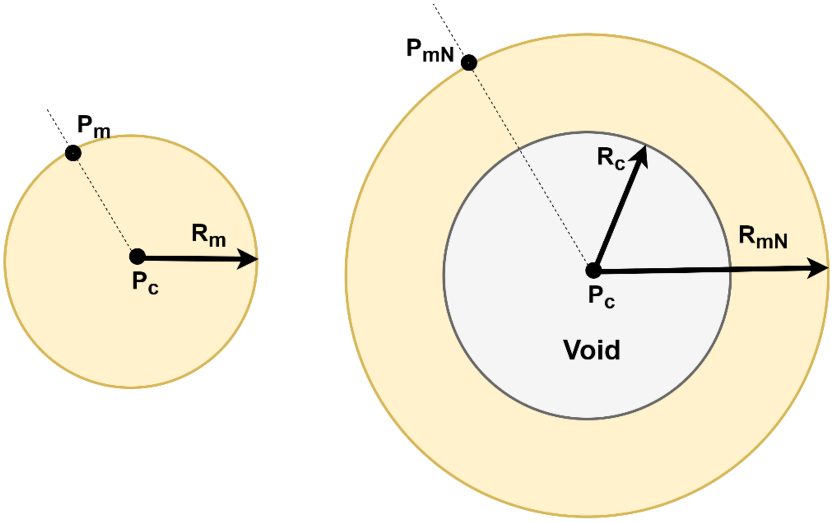

Figure 4.4 Point P_m moves when the void expands to radius R_c

Similarly, it is possible to determine the new distances of the two endpoints to the center of the foam cell using Equations **(4.3.4)** and **(4.3.5).**

$$\boldsymbol{R_{1N}} = \sqrt[3]{\boldsymbol{R_1^3} + \boldsymbol{R_c^3}} \tag{4.3.4}$$

and

$$\boldsymbol{R_{2N}} = \sqrt[3]{\boldsymbol{R_2^3} + \boldsymbol{R_c^3}} \tag{4.3.5}$$

After the determination of $\boldsymbol{R_{1N}}$ and $\boldsymbol{R_{2N}}$, the new endpoints (i.e., $\boldsymbol{P_{1N}}$ and $\boldsymbol{P_{2N}}$) of CNT after the translational and rotational motion will be located on two concentric spheres defined by $\boldsymbol{R_{1N}}$ and $\boldsymbol{R_{2N}}$ as shown in Figure 4.5.

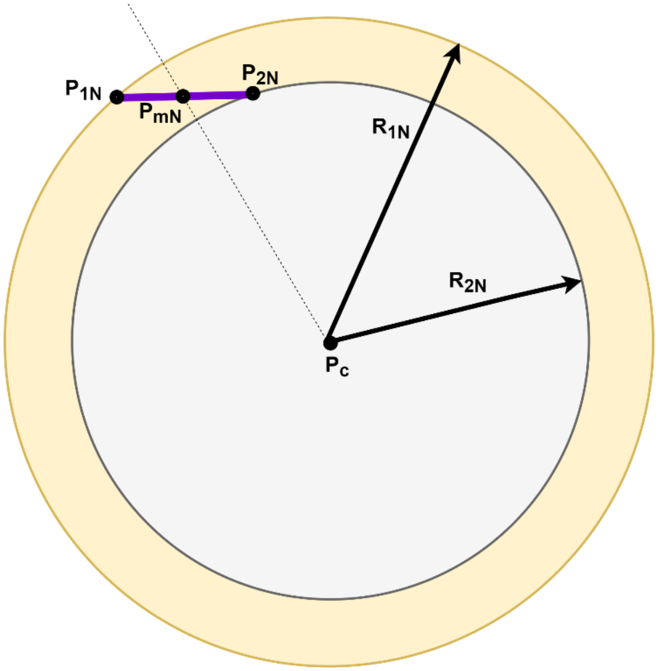

Figure 4.5 Occupied volume is unchanged during foaming expansion

It is noted that after the translational and rotational motion, the CNT will still stay on the same plane defined by $\boldsymbol{P_c}$, $\boldsymbol{P_1}$, and $\boldsymbol{P_2}$. Equivalently, $\boldsymbol{P_{1N}}$ (or $\boldsymbol{P_{2N}}$) will be on the intersection of two spheres, defined by radii from $\boldsymbol{P_c}$ to $\boldsymbol{P_{1N}}$ (or $\boldsymbol{P_{2N}}$) and that from $\boldsymbol{P_{mN}}$ to $\boldsymbol{P_{1N}}$ (or $\boldsymbol{P_{2N}}$), respectively, as illustrated in Figure 4.6. Therefore, the coordinates of $\boldsymbol{P_1}$ and $\boldsymbol{P_2}$ can be determined by finding the intersection between the aforementioned plane and these two spheres.

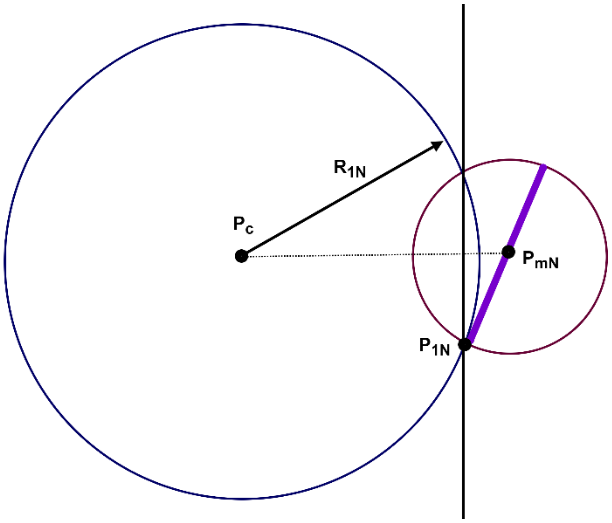

Figure 4.6 Equivalent solution to find $\boldsymbol{P_{1N}}$ *or* $\boldsymbol{P_{2N}}$

Since all the characteristic points are on the plane defined by $\boldsymbol{P_c}$, $\boldsymbol{P_1}$, and $\boldsymbol{P_2}$, it is now possible to transform the three-dimensional problem into a two-dimensional one in order to simplify the computation process. In other words, the problem is simplified to one that requires the determination of two circles. The first circle has its center at $\boldsymbol{P_c}$ and its radius of $\boldsymbol{R_{1N}}$. The second one has its center at $\boldsymbol{P_{mN}}$ and radius equals half of the length of CNT (i.e., $\boldsymbol{L_{CNT}/2}$) as demonstrated in Figure 4.7.

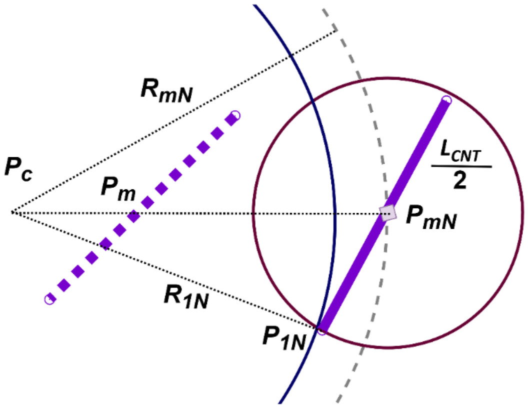

Figure 4.7 Determining a new endpoint of CNT based on two intersecting spheres.

In order to transform the 3D coordinates into 2D ones, a new coordinate system is set up where the x-axis is parallel to $\boldsymbol{P_c P_{mN}}$ and the $\boldsymbol{P_c}$ is set as the origin (0, 0) of this coordinate system. Then, the coordinates of $\boldsymbol{P_{mN}}$ are ($\boldsymbol{R_{mN}}$, 0) as illustrated in Figure 4.8.

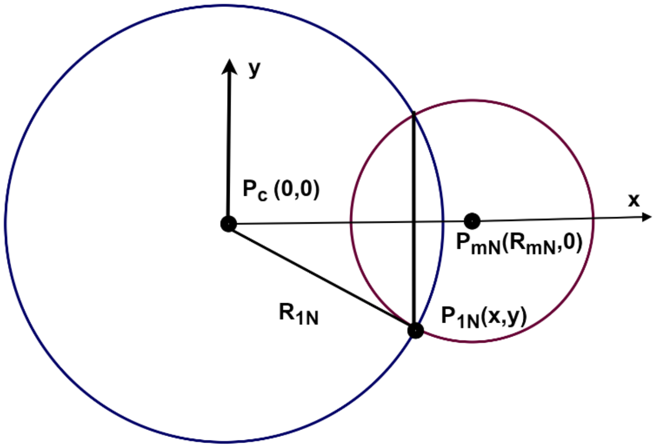

Figure 4.8 Problem of 2-sphere intersection

Under this new coordinate system, the coordinates of $\boldsymbol{P_{1N}}$ can be determined by finding the intersection of the two circles. The equations of the two circles are expressed in Equations **(4.3.6)** and **(4.3.7).**

$$\boldsymbol{x^2 + y^2 = R_{1N}^2} \tag{4.3.6}$$

and

$$\boldsymbol{(x - R_{mN})^2 + y^2 = \left(\frac{L_{CNT}}{2}\right)^2} \tag{4.3.7}$$

Solving the above system of equations, it is then possible to determine the coordinates of $\boldsymbol{P_{1N}}$, which are expressed as:

$$\boldsymbol{x} = \frac{\boldsymbol{R_{mN}}^2 - \left(\frac{\boldsymbol{L_{CNT}}}{2}\right)^2 + \boldsymbol{R_{1N}^2}}{2\boldsymbol{R_{mN}}} \tag{4.3.8}$$

and

$$\boldsymbol{y}^2 = \boldsymbol{R_{1N}^2} - \boldsymbol{x}^2 \tag{4.3.9}$$

It must be noted that there are two y coordinates when Equation **(4.3.9)** is solved. The y-coordinate of $\boldsymbol{P_{1N}}$, has the same sign as that of $\boldsymbol{P_1}$ (i.e., the corresponding endpoint before foam expansion).

After finding the coordinates of $\boldsymbol{P_{1N}}$ in this 2D coordinate system, they must be transformed to a new 3D coordinate system by setting the z-coordinates to be zero, where the positive z direction is defined by Equation **(4.3.10).**

$$\vec{\boldsymbol{z}} = \overrightarrow{\boldsymbol{P_c P_{1N}}} \times \vec{\boldsymbol{x}} \tag{4.3.10}$$

Consequently, the coordinates of each characteristic point will be transformed from this new 3D coordinate system back to the original 3D coordinate system using an approach reported in [83].

By considering the vector equation that represents a line parallel to the CNT and the length of the CNT, the other new endpoint, $\boldsymbol{P_{2N}}$, could be determined using Equations **(4.3.11)** and **(4.3.12).**

$$\boldsymbol{P_{2N}} = \boldsymbol{P_{mN}} + \frac{\boldsymbol{L_{CNT}}}{2}\vec{\boldsymbol{u}} \tag{4.3.11}$$

where

$$\vec{u} = \frac{\vec{v}}{\|\vec{v}\|} \text{ and } \vec{v} = P_{mN} - P_{1N} \quad \textbf{(4.3.12)}$$

Figure 4.9 illustrates the translational motion of CNTs as a result of foaming. The graph shows the number of tubes at a different distance from the center of the foam cell before and after the foaming process at low volume-expansion ratios. The increase in distance is consistent with the schematic shown in Figure 4.2. However, the distance of the translational motion decreases as the initial distance between the CNT and the center of the foam cell increases. The changes in the shape of histogram distributions before and after the foaming process showed the non-uniform effect of foaming expansion on the tubes. In conclusion, the further the tube is from the center, the less translational motion was induced by the foaming expansion.

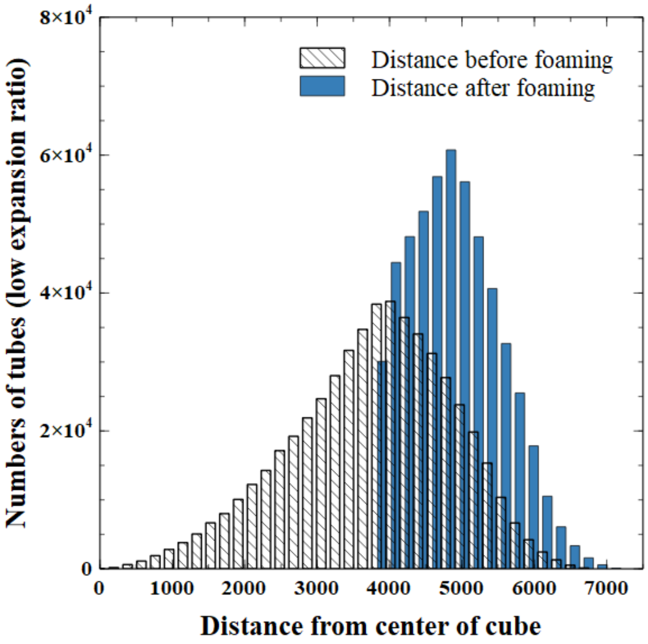

Figure 4.9 Histogram of distances from the center of foam cell to tubes were before and after

foaming process at low volume-expansion ratio.

4.4 Modeling Foaming at High Volume-Expansion Ratio

At a high expansion ratio, the shape of the foam cell is no longer spherical, and it becomes polyhedral due to the interference among adjacent cells. In order to handle the situation with manageable demand in computation power, a cubic model is adopted in this study. The midpoint of the tube is still translated radially from the center of the foam cell during foaming. The rotation of the tube is again based on the incompressible property of the polymer matrix. Figure 4.10 illustrates a schematic to describe the rotational motion of the CNT caused by foam expansion. The purple point in this figure is used to define the direction of the reoriented CNT. This point is collinear with the center of the cube and one of the endpoints of the CNT before foam expansion. Its position can be determined by the following relationship as shown in Figure 4.10:

$$\frac{\boldsymbol{L_2}}{\boldsymbol{L_1}} = \frac{\boldsymbol{R_2}}{\boldsymbol{R_1}} \qquad \textbf{(4.4.1)}$$

Once the value of $\boldsymbol{R_2}$ has been determined, the coordinates of the two endpoints of the CNT can be found by using its length and the direction defined by joining the midpoint of the CNT and the purple point.

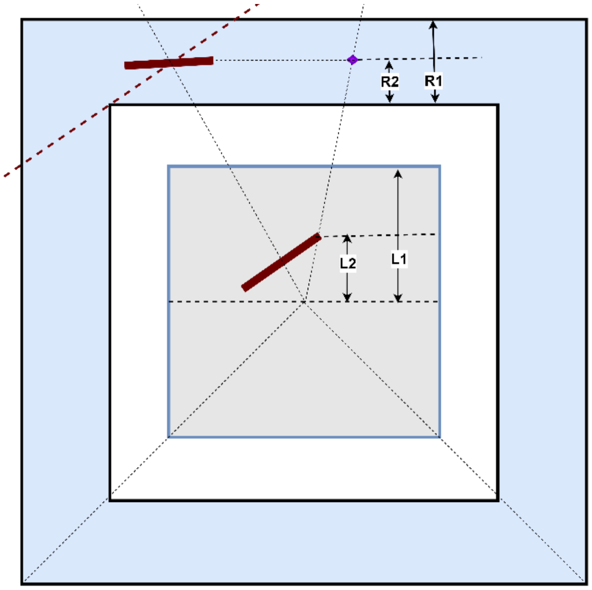

Figure 4.10 Model of cubic expansion for incompressible material at different stages.

In addition, the rotation of the tube strongly depends on the volume-expansion ratio as illustrated in Figure 4.11. It can be observed that a higher degree of reorientation would occur as the volume-expansion ratio increases. Furthermore, at a high volume-expansion ratio, the cell wall is very thin, and the CNT would become virtually parallel to the walls.

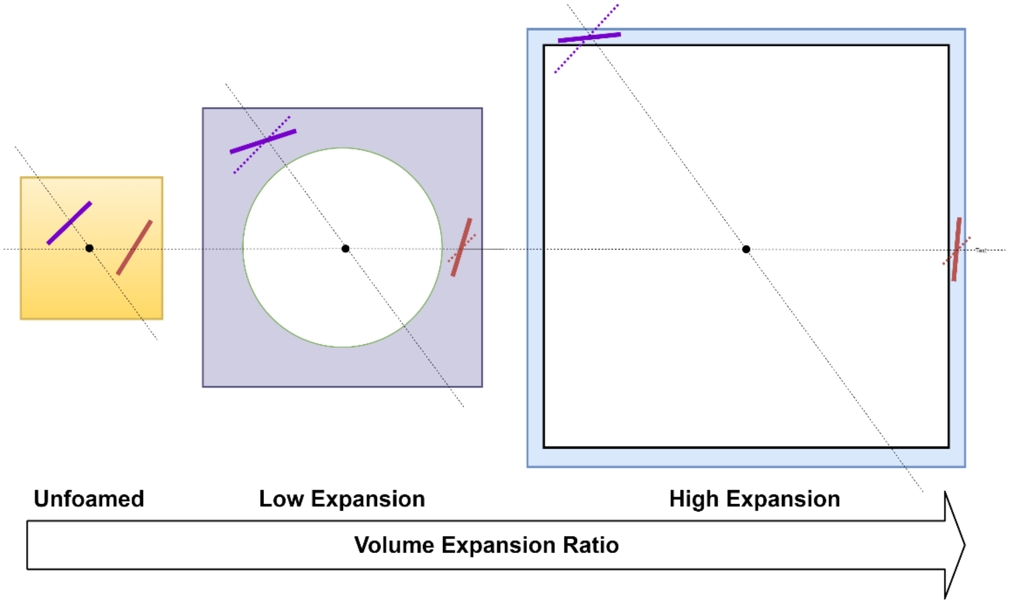

Figure 4.11 Rotational motion of CNT as a result of different degrees of volume expansion.

Figure 4.12 illustrates the number distribution of CNTs with specific **cos(θ)** (i.e., the cosine of the polar angle) and angle **φ** (i.e., the azimuthal angle) before and after the foaming process at a high volume-expansion ratio (i.e., 20 times as a case example). The large number of CNT with **cos(θ)** close to -1, 0, and 1 indicates that most CNTs have been reoriented to directions parallel to the cell walls. Furthermore, it can be observed that most CNTs have their values of angle **φ** equal to -180 ^{o}, -90^{o}, 0^{o}, 90^{o}, and 180^{o} after foam expansion. This indicates that most CNTs were aligned with the xz-plane and yz-plane. In other words, this again reveals that CNTs would preferentially align along the cell walls after the polymer nanocomposite has undergone large volume expansion.

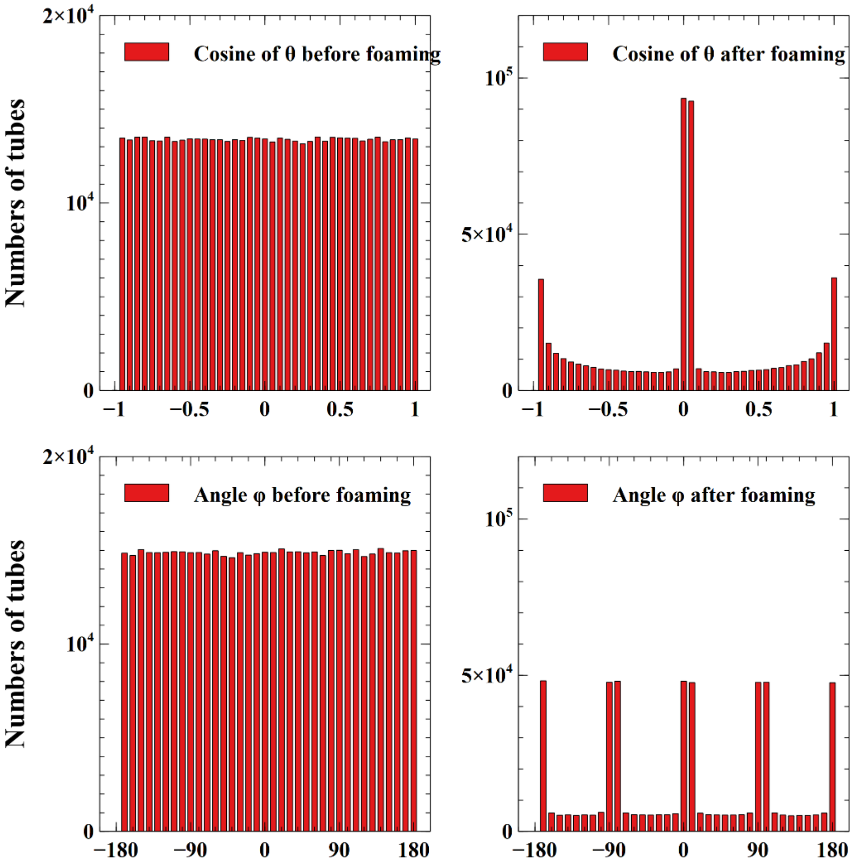

Figure 4.12 Histograms of ***cos(θ)*** *and angle* ***φ*** *before and after foaming process at high volume-expansion ratio.*

4.5 Alteration of Resistor Networks

Figure 4.13 and Figure 4.14 illustrate my work on the influence of foam expansion on the CNT conductive networks (i.e., in terms of the number of (i) nodes; (ii) nodes per cluster; and (iii) nodes per conductive path) embedded in the polymer matrix. It can be observed that regardless of the initial MWCNT loading (in vol.%), there exists a higher increase in the number of nodes after foaming relative to the original number of nodes in the unfoamed nanocomposites as the volume-expansion ratio increases. It is because the foam expansion results in the compacting of the MWCNT in the thin cell walls, enhancing the interconnectivity among them. Furthermore, the effect of foaming on the promotion of the connectivity among MWCNT is more significant for nanocomposites loaded with lower loading of MWCNT initially.

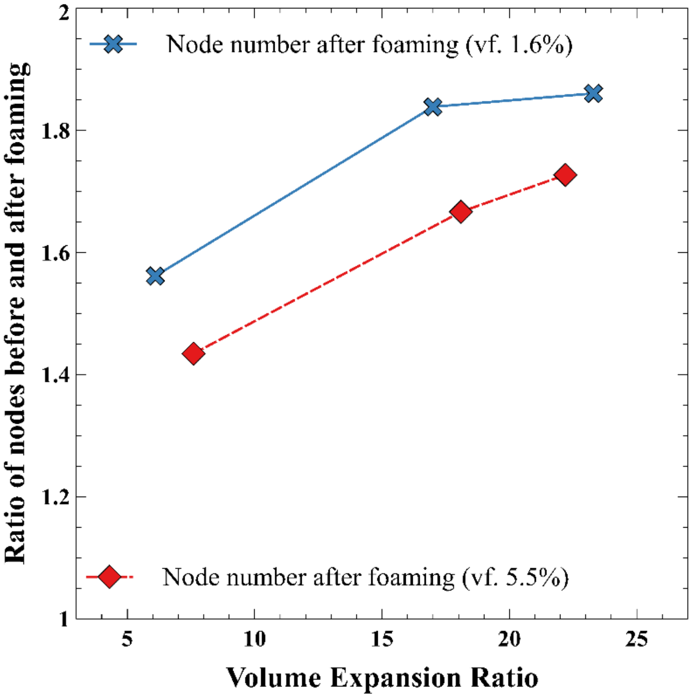

Figure 4.13 Relative increase in the number of nodes after foaming for nanocomposites with initial MWCNT loadings of 5.5 vol.% and 1.6 vol.%. (Note: Relate increase is the ratio of the number of nodes after foaming to that before foaming)

Figure 4.14 presents the relative increases of the average numbers of nodes per cluster and conductive path before and after the foaming process at different volume-expansion ratios for nanocomposites initially loaded with 5.5 vol.% and 1.6 vol.% MWCNT. The foaming process promotes both the number of nodes per cluster and that per conductive path compared to the pre-foam cases. However, when the expansion is extremely large, the numbers of nodes per conductive path reduce, meaning the foaming process breaks the conductive paths and creates more nodes per cluster. It must be noted that clusters are groups of connected CNTs, but they do not necessarily connect the two electrodes and thereby may not contribute to the equivalent conductivity. The smallest number of CNTs per cluster is two.

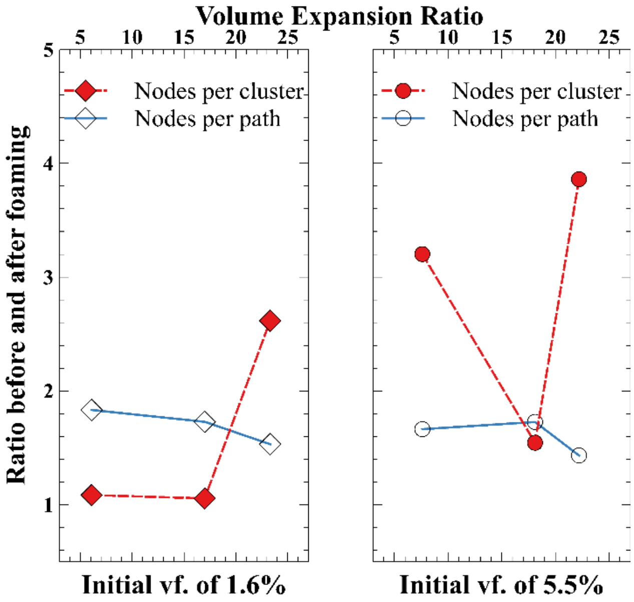

Figure 4.14 Ratios of nodes per clusters and conductive path before and after foaming process at different volume-expansion ratio for vf. of 5.5% and 1.6%.

4.6 Strategy to Overcome the High Demand of Computation Power

In order to validate the model, the simulation results were compared to the experimental data. It must be noted that some input parameters (e.g., cell size) for the simulation had to be obtained from experimental observation in order to simulate the realistic situation. Considering the nanocomposite has undergone a high-volume expansion (e.g., 20 times) as a case example, Table 4.1 summarizes the length scale of the RVE and the number of MWCNT required to simulate a nanocomposite foam with different cell sizes, ranging from approximately tens to hundreds of times of the MWCNT length (i.e., 0.8 μm). It can be observed that as the cell size increases, the length scale of the RVE must increase accordingly, this leads to a significant increase in the number of MWCNT to be generated in the RVE. Since the number of computational steps is approximately proportional to the square of the number of MWCNT in the RVE, this would dramatically increase the demand in computational power, which may go beyond the computer capacity.

Table 4.1 Estimations of numbers of CNT needed in simulations at different RVE volume scales

Length of CNT (µm)	RVE length Scale	Volume-expansion ratio	Foam-Cell size (µm)	Wall thickness (µm)	Number of CNT generated		
					Initial volume fraction (%)		
					1.60%	2.70%	5.50%
0.8	5	20	10.9	0.19	1.8E+04	3.1E+04	6.2E+04
0.8	10	20	21.7	0.37	1.4E+05	2.4E+05	5.0E+05
0.8	20	20	43.4	0.75	1.2E+06	2.0E+06	4.0E+06
0.8	30	20	65.1	1.12	3.9E+06	6.6E+06	1.3E+07
0.8	40	20	86.9	1.50	9.3E+06	1.6E+07	3.2E+07
0.8	50	20	108.6	1.87	1.8E+07	3.1E+07	6.2E+07
A sample of real measurement: Foam cell size 113 um and Expansion Ratio of 23							

One strategy to overcome this challenge is described below.

- The simulation volume is subdivided into several partitions based on the direction of current flow as shown in Figure 4.15 and these partitions have their own electrical conductivity σ_1 and σ_2 as shown in Figure 4.15 (b).

- Each partition can be considered as an individual resistor (i.e., R_1 through R_5) as shown in Figure 4.15 (a).
- R_1, R_2 and R_3 are parallel to the current flow. R_4 and R_5 are perpendicular to the current flow.
- Resistors connect to form a resistor network (as shown in Figure 4.15 (c)).
- Solve the equivalent circuit to get equivalent resistance and calculate the electrical conductivity based on the dimension of the RVE.

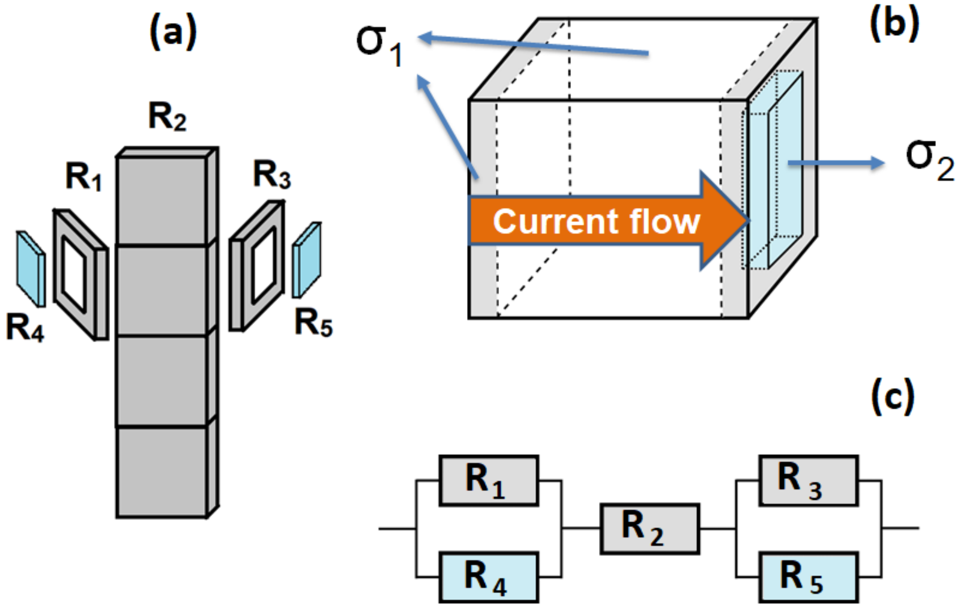

Figure 4.15 Partial simulation demonstrations for a large size of a foam cell:

(a) subdivided partitions considered as individual resistors;

(b) schematic anisotropic conductivity based on current flow;

(c) equivalent circuit.

Therefore, it is possible to generate two child RVEs (as shown in Figure 4.16), which are substantially smaller than the parent RVE, to simulate the electrical conductivity of these two cases. Consequently, the conductivity of the child RVEs can be used to determine the equivalent conductivity of the parent RVE (i.e., a unit cell of the nanocomposite foam). This strategy will significantly reduce the required computational power required by the simulation.

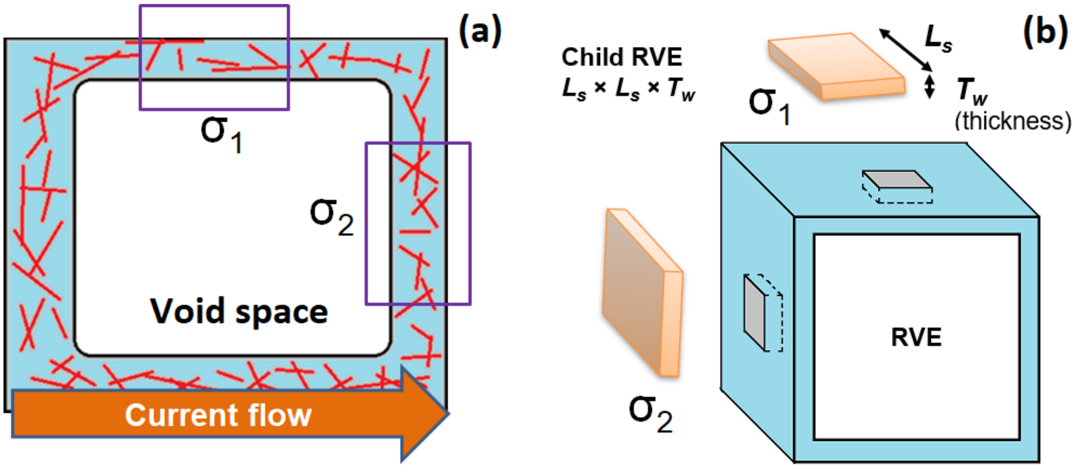

Figure 4.16 Subdivisions of RVE

In more detail, the σ_1 is extracted from the simulation of electrical conductivity of the child RVE that is parallel to the current flow direction. The dimension of the child RVE is $L_s \times L_s \times T_w$, where L_s is desired simulation size and T_w is the thickness of the cell wall as illustrated in Figure 4.16 (b). Its conductive length is L_s and cross-sectional areas is $L_s \times T_w$. This child RVE can be used to represent resistors R_1, R_2, and R_3.

R_1 and R_3 are identical which have conductive length of T_w and cross-sectional areas of $[L^2 - (L - T_w)^2]$ where L is the length of the parent RVE. Hence, their equation is the Equation **(4.6.1)**. In case of R_2, its conductive length is $L - 2T_w$ and cross-sectional areas of $[\boldsymbol{L^2 - (L - T_w)^2}]$. Therefore, its equation is the Equation **(4.6.2)**.

$$\boldsymbol{R_1 = R_3 = \frac{T_w}{\sigma_1 \times [L^2 - (L - T_w)^2]}} \quad \textbf{(4.6.1)}$$

$$\boldsymbol{R_2 = \frac{L - 2T_w}{\sigma_1 \times [L^2 - (L - T_w)^2]}} \quad \textbf{(4.6.2)}$$

Similarly, σ_2 is extracted from the simulation of electrical conductivity of the child RVE that is perpendicular to the current flow direction. The dimension of the child RVE is $\boldsymbol{T_w \times L_s \times L_s}$. Its conductive length is $\boldsymbol{T_w}$ and cross-sectional areas is $\boldsymbol{L_s \times L_s}$. This child RVE can be used to represent resistors $\boldsymbol{R_4}$ and $\boldsymbol{R_5}$ which are identical and have conductive length of $\boldsymbol{T_w}$ and cross-sectional areas of $[\boldsymbol{(L - 2T_w)^2}]$. Eventually, their resistances are presented below.

$$\boldsymbol{R_4 = R_5 = \frac{T_w}{\sigma_2 \times (L - 2T_w)^2}} \quad \textbf{(4.6.3)}$$

The equivalent resistance $\boldsymbol{R_E}$ is calculated based on the equivalent circuit as the Equation **(4.6.4)** and the equivalent electrical conductivity σ_E can be extracted as the Equation **(4.6.5).**

$$\boldsymbol{R_E = \frac{R_1 R_4}{R_1 + R_4} + R_2 + \frac{R_3 R_5}{R_3 + R_5}} \quad \textbf{(4.6.4)}$$

$$\boldsymbol{R_E = \frac{L}{\sigma_E \times L^2}} \quad or \quad \boldsymbol{\sigma_E = \frac{L}{R_E \times L^2}} \quad \textbf{(4.6.5)}$$

4.7 Conclusions

The simulation of foaming can be successfully performed in two cases. At the beginning, when the foam cell starts expanding, the shape is conserved as a sphere. In the next phase, the shape is considered as a cube with thin walls. A comparison between the simulation results and the experimental results will be presented in Chapter 6.

Chapter 5 EXPERIMENTAL SETUP & RESULTS

Summary: In this chapter, we introduce the experimental fabrication of polymer nanocomposites and their foam. The samples were characterized in terms of their electrical conductivity. The effect of foaming on the electrical conductivity of polymer nanocomposites was discussed.

5.1 Introduction

This study investigates the application of supercritical carbon dioxide ($ScCO_2$) foaming to tailor the nanostructure of high-density polyethylene (HDPE)/multi-walled carbon nanotube (MWCNT) nanocomposites. In the previous study [24], the HDPE/MWCNT nanocomposites were examined only at 15 wt.% of MWCNT loaded originally by the material provider, leading to the incomplete understanding of morphologies and electrical properties of nanocomposites and their foams. Hence, parametric studies were conducted to elucidate the processing-structure-property relationships of HDPE/MWCNT nanocomposites and their foams. The effects of initial MWCNT loading and foaming temperature on the foam morphology and the MWCNT networking of HDPE/MWCNT nanocomposites were studied. Further systematic studies of the interrelations among HDPE/MWCNT nanocomposite's foam morphology, MWCNT localization and networking, as well as the material system's electrical conductivity and percolation threshold were completed.

5.2 Material and Sample Preparations

5.2.1 Material Preparations

Commercially available HDPE/MWCNT nanocomposite masterbatch (Nanocyl, Plasticyl HDPE1501), loaded with 15 wt.% MWCNT (Nanocyl, NC7000™), and neat HDPE (NOVA Chemicals, SCLAIR® 2710) were used to prepare HDPE/MWCNT nanocomposites of different MWCNT loadings. The constituent MWCNT had an average length of 1.5 μm and an average diameter of 9.5 nm. The physical foaming agent used in this study was carbon dioxide (CO_2) (Linde Gas Inc., 99.8% purity). The physical properties of HDPE/MWCNT masterbatch, HDPE, and MWCNT are summarized in Table 5.1 to Table 5.3. All materials were used as received with no modification.

Table 5.1 Physical properties of HDPE/MWCNT masterbatch [84].

Property	Value	Unit
MWCNT Loading	15	wt.%
Density	977	kg/m^3
Melting Temperature	135	°C
Resistivity	1.0 (max)	kΩ

Table 5.2 Physical properties of neat HDPE [85].

Property	Value	Unit
Density	951	kg/m^3
Vicat Softening Temperature	125	°C

Table 5.3 Physical properties of MWCNT [86].

Property	Value	Unit
Average Diameter	9.5	nm
Average Length	1.5	μm
Carbon Purity	90	%
Surface Area	250-300	m^2/g
Volume Resistivity	10^{-4}	Ω·cm

5.2.2 Solid Sample Fabrication

The HDPE/MWCNT nanocomposites with different MWCNT loadings were prepared by diluting the HDPE/MWCNT masterbatch with calculated amounts of neat HDPE. The dilution was done by melting the mixtures using a micro-compounder (HAAKE™ MiniCTW Micro-Conical Twin Screw Compounder) in the circulating mode for 5 minutes at 215°C, with the spinning speed set at 75 rpm as drawn in Figure 5.1 (a).

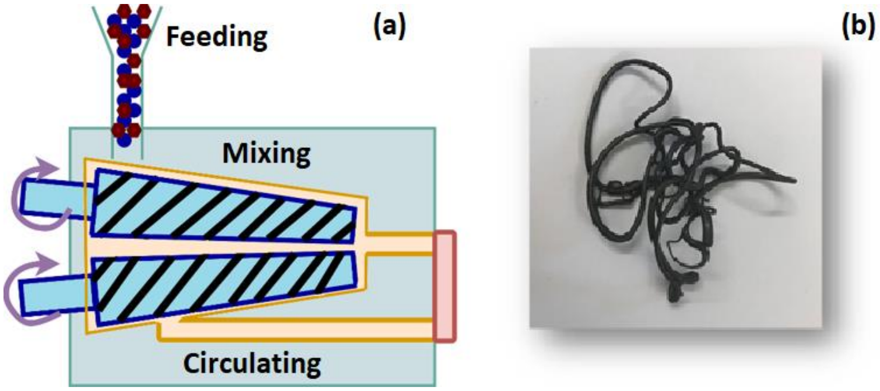

Figure 5.1 Melt-compounding of HDPE/MWCNT masterbatch and (a) neat HDPE; (b) extrudates.

The extrudates, illustrated in Figure 5.1 (b), were pelletized and compression molded into a circular disc sample of 115 mm in diameter and 0.50 mm in thickness using a compression molding machine (Craver Press, 4386 CH) as shown in Figure 5.2. The compression molding procedure is summarized below:

Step 1. A weighed amount of HDPE/MWCNT nanocomposite pellets was loaded into a circular disc mold of 115 mm in diameter and 0.50 mm in thickness.

Step 2. The compression molding machine was equilibrated at 155°C.

Step 3. The heat platens of the compression molding machine were brought into contact with the mold, which loaded with the nanocomposite pellet, for 5 minutes to ensure the complete melting of the nanocomposite pellet as illustrated in Figure 5.2 (a).

Step 4. The molding pressure was ramped up gradually to 27.6 MPa and held at this level for 6 minutes as illustrated in Figure 5.2 (b).

Step 5. The disc sample, which was still inside the mold, was transferred to a cooling module with flowing water channels to solidify the disc sample which was illustrated in Figure 5.2 (c).

Step 6. The sample was cut into rectangular specimens with dimensions of 12 mm × 10 mm × 0.50 mm. The specimens would then be characterized using an electrical conductivity analyzer or be foamed by ScCO2.

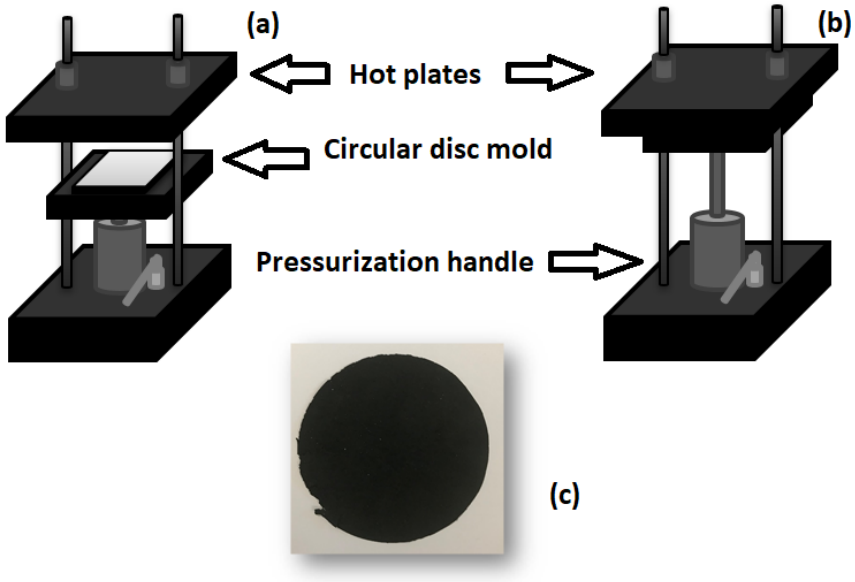

Figure 5.2 Demonstration of compression molding process: (a) preparing; (b) compressing; (c) circular disc of sample of compressed mold.

5.2.3 Foaming Sample Fabrication

HDPE/MWCNT nanocomposite foams were fabricated by a batch foaming chamber using $ScCO_2$ as the physical foaming agent as drawn in Figure 5.3. In the physical foaming process, nanocomposite specimens were saturated with $ScCO_2$ for 30 minutes at pre-set combinations of saturation pressure (P_{sat}) and saturation temperature (T_{sat}). Subsequently, an outlet valve of the batch-foaming chamber was opened to rapidly depressurize it. This led to thermodynamic instability in the HDPE/MWCNT/$ScCO_2$ system and thereby induced cell nucleation and subsequent cell growth in the HDPE matrices. Table 5.4 summarizes the key parameters being studied in the physical foaming experiments.

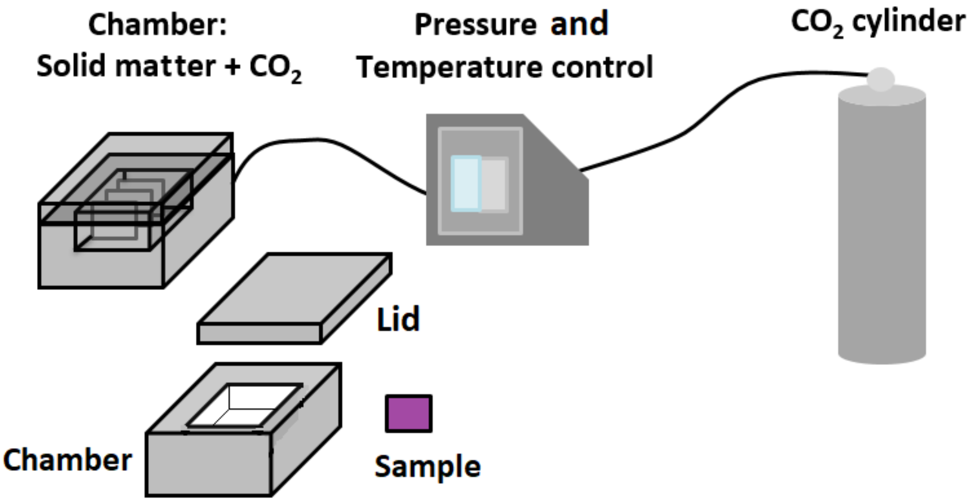

Figure 5.3 Scheme of physically foaming process.

Table 5.4 Parameters studied in physical foaming experiments

Parameter	***Value***	***Unit***
MWCNT Loading	0,1, 2, 3, 5, 7, and 10	wt.%
P_{sat}	8.3, 13.8, and 19.3	MPa
T_{sat}	123 - 135	ºC
Saturation Time	30 (fixed)	min

5.2.4 Sample Characterization

The apparent density of HDPE/MWCNT nanocomposite foams was determined in accordance with ASTM D792. After measuring their masses in the air and in water, the apparent density of a foam sample (ρ_f) and the volume-expansion ratio (ϕ) can be determined by Equations **(5.2.1)** and **(5.2.2)**, respectively [87].

$$\boldsymbol{\rho_f = \frac{m_{air}\rho_{water}}{m_{air} - m_{water}}} \tag{5.2.1}$$

$$\boldsymbol{\phi = \frac{\rho_s}{\rho_f}} \tag{5.2.2}$$

where m_{air} and m_{water} are the masses of samples measured in air and in water, respectively; ρ_{water} is the density of water, and ρ_s is the density of the solid HDPE/MWCNT nanocomposite sample.

The phase and foam morphologies of the solid and foamed HDPE/MWCNT nanocomposite samples were characterized by scanning electron microscopy (SEM) (FEI Company Quanta 3D FEG). The cross-sections of all samples were exposed by cryo-fracturing the samples under liquid nitrogen. The fractured surfaces were then sputter-coated with gold (Denton Vacuum, Desk V Sputter Coater). The cell size and cell population density of selected foam samples were obtained by analyzing the SEM micrographs of the foams using ImageJ software (National Institute of Health). The cell population density (N_0) with respect to the unfoamed volume was determined by Equation **(5.2.3)** [88].

$$\boldsymbol{N_0 = \phi \times \left[\frac{nM^2}{A}\right]^{\frac{3}{2}}} \qquad \textbf{(5.2.3)}$$

where n is the number of cells in the SEM micrograph; M is the magnification factor of the micrograph; and A is the area of the micrograph.

5.3 Micro-and-Nanostructures of CPNs and Foams

Figure 5.4 (a) through (f) show the SEM micrographs of HDPE/MWCNT loaded with 3 wt.% MWCNT before injected to ScCO$_2$ foaming at P_{sat} of 8.3 MPa and after at different T_{sat}. Experimental observation revealed that foam morphologies of

HDPE/MWCNT nanocomposite foams had a strong dependence on T_{sat}. At 123ºC, the HDPE matrix, reinforced by MWCNT, was too stiff to achieve observable foam expansion. As T_{sat} gradually increased, the foam morphologies evolved from having a high cell density with fine cells to a reduced cell density with larger cells. The foam structure finally deteriorated when T_{sat} was increased to 135°C. In other words, within the processing window, varying T_{sat} would be an effective approach to tune the cell morphologies and thereby the MWCNT network of HDPE/MWCNT nanocomposite foams.

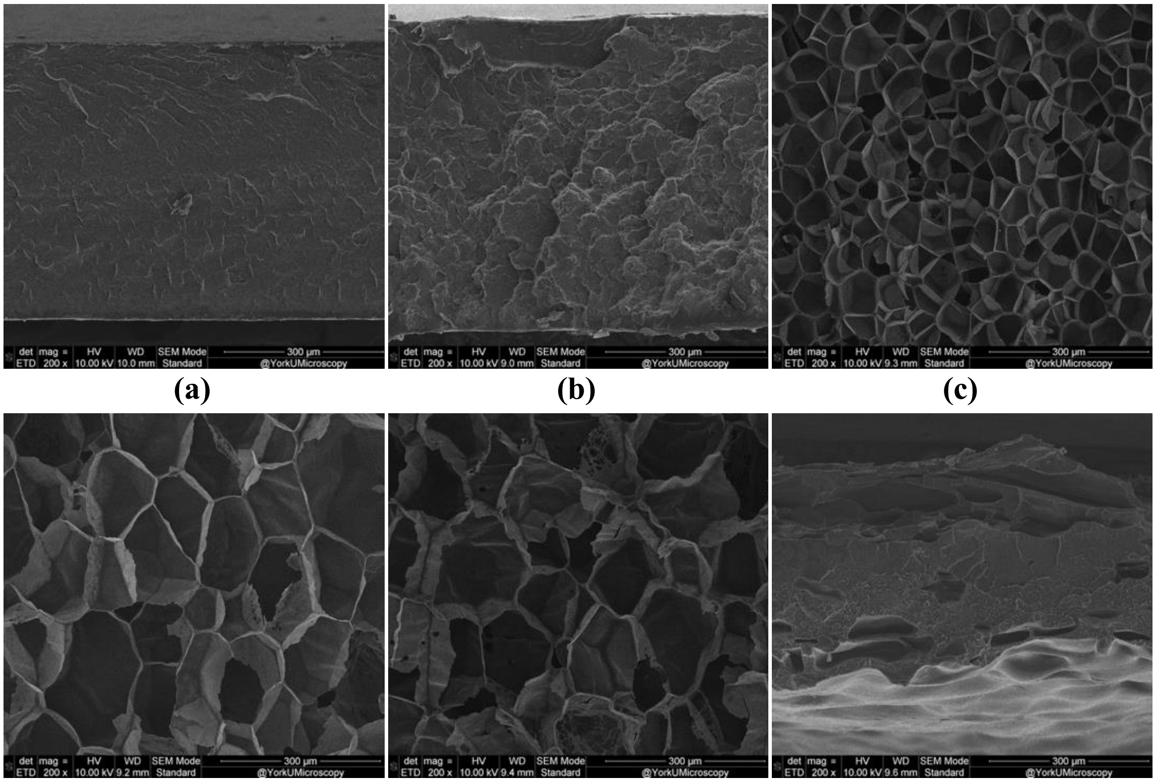

(a) **(b)** **(c)**

(d) **(e)** **(f)**

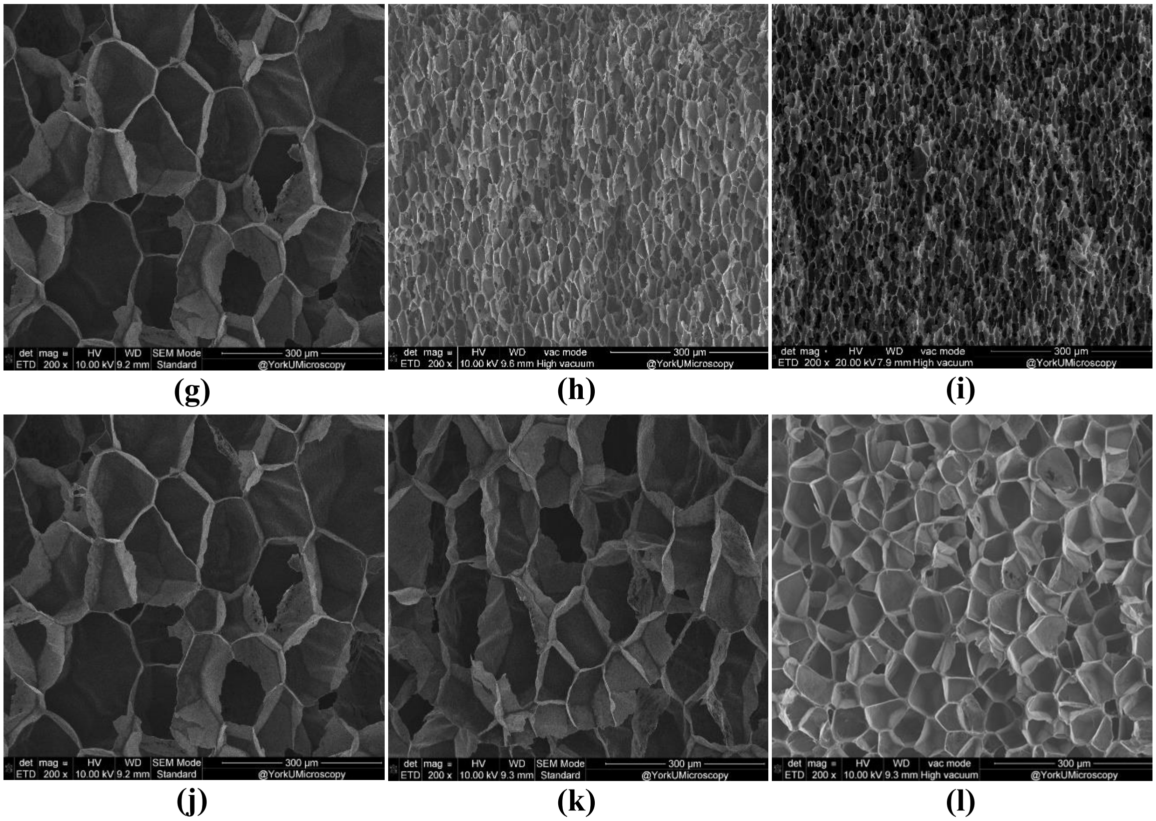

(g) (h) (i)

(j) (k) (l)

Figure 5.4 SEM micrographs of HDPE/MWCNT nanocomposites and foams loaded with 3 wt.% at P_{sat} of 8.3 MPa and different T_{sat}: (a) solid nanocomposite; and foams at (b) 123ºC, (c) 125ºC, (d) 127ºC, (e) 130ºC, and (f) 135ºC; at T_{sat} of 127ºC but different in P_{sat}: (g) 8.3 MPa, (h) 13.8 MPa, (i) 19.3 MPa; and at P_{sat} of 8.3 MPa, T_{sat} of but 127ºC different in MWCNT loadings: (j) 3 wt.%, (k) 5 wt.%, (l) 10 wt.%.

5.4 Effects of Foaming Conditions on Volume-Expansion Ratios

The results for neat HDPE polymer and different initial loadings (i.e., in wt.%) of MWCNT at two levels of P_{sat} are plotted in Figure 5.5. It can be observed that the foaming behaviors of the neat HDPE depended strongly on both P_{sat} and T_{sat}. Regardless of the P_{sat}, the optimal T_{sat} to maximize the volume-expansion ratio was 124°C. The achieved volume-expansion ratios were 17.7 and 8.7 for P_{sat} of 13.8 MPa and 8.3 MPa, respectively. For foams prepared at P_{sat} of 13.8 MPa, the higher level of dissolved CO_2 together with the higher depressurization rate contributed to a higher degree of supersaturation. This led to a more rapid foam expansion and a shorter period for gas loss to the surrounding. Both factors contributed to the higher volume-expansion ratio achieved at higher P_{sat}. However, the expansion of the neat HDPE was extremely sensitive to T_{sat}, and the narrow processing window limited the control of the foaming process. When the temperature was below the optimal T_{sat}, the polymer was too stiff and limited the expansion. In contrast, at a temperature higher than the optimal T_{sat}, the weakened cell wall together with the high diffusivity led to an increase of gas loss.

By reinforcing the HDPE matrix with MWCNTs, the stiffness of nanocomposites increased, which shifted the optimal T_{sat} to a higher level. Furthermore, the strengthening of the cell wall, which increased the melt strength also widened the processing window because of the suppression of cell rupture at high temperature. The maximum volume-expansion ratios were 6 and 23 for nanocomposite foams prepared at 13.8 MPa and 8.3 MPa, respectively. It is noted that the volume-expansion ratio of nanocomposite foams prepared at 13.8 MPa increased and achieved a plateau instead of decreasing as T_{sat} increased. This can be explained by the increase in cell nucleation rate and decrease in cell growth of individual cells, which helped to suppress the rupture of the cell wall at high T_{sat}. The minimum required T_{sat} to maximize foam expansion increased from 125°C to 127°C as MWCNT loading increased from 1 wt.% to 10 wt.%. This was caused by the increased stiffness of the matrix, which led to the need of elevated T_{sat} to soften the matrix for effective foam expansion. In contrast, for nanocomposite foams prepared at 8.3 MPa, the foaming behavior was similar to that of neat HDPE. The volume-expansion ratio increased as T_{sat} increased initially; however, when T_{sat} continued to increase above the optimal T_{sat}, the volume-expansion ratio decreased. Due to the lower level of supersaturation, cell nucleation rate decreased, and more CO_2 was used for cell growth instead of nucleation of new cells. The more substantial expansion of individual cells led to the increase in cell wall rupture at high T_{sat}. This resulted in significant gas loss and thereby the reduced volume-expansion ratio at T_{sat} higher than the optimal level.

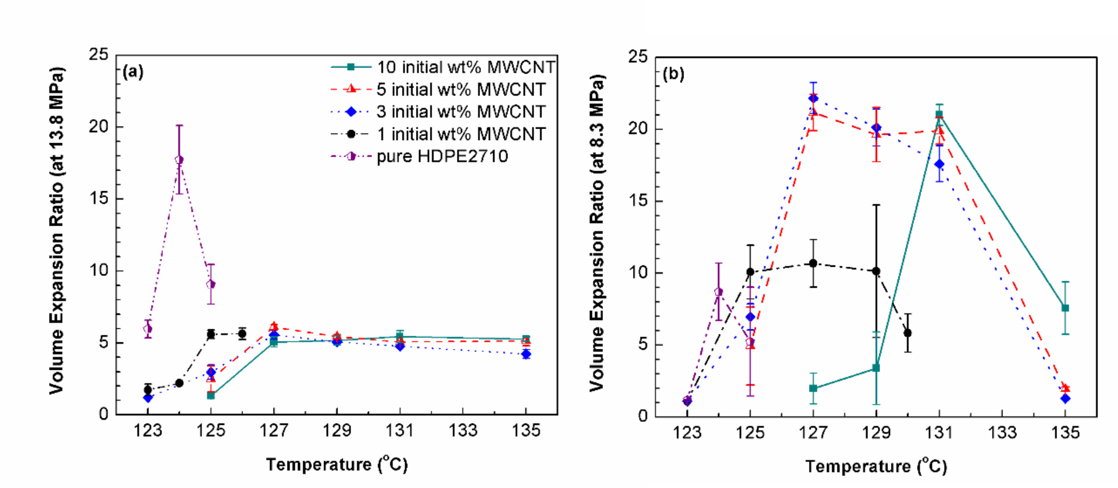

Figure 5.5 Effects of T_{sat} on volume-expansion ratio of HDPE/MWCNT nanocomposite foams with different initial MWCNT loadings at saturation pressure of (a) 13.8 MPa; and (b) 8.3 MPa.

5.5 Effects of Foaming Conditions on Foam Morphologies

The effects of foaming conditions on foam morphologies were further investigated by analyzing the cell size and the cell population density obtained under various foaming conditions. Figure 5.6 (a) illustrates the effect of P_{sat} on the cell size and cell population density of nanocomposite foams, loaded with 3 wt.% of MWCNT, prepared at 127^{o}C. As P_{sat} increased from 8.3 MPa to 19.3 MPa, the cell size reduced while the cell population density increased. At high P_{sat}, there was be a higher degree of supersaturation due to the higher level of dissolved CO_2 and higher depressurization rate. Both led to higher cell nucleation. In other words, more gas was used to form new cells instead of expanding the nucleated cells. As a result, the nanocomposite foams yielded a higher number of smaller cells.

Figure 5.6 (b) illustrates the effect of T_{sat} on the foam morphologies of nanocomposite foams, loaded with 3 wt.% of MWCNT, foamed at P_{sat} of 8.3 MPa. By increasing T_{sat} from 125^{o}C to 135^{o}C, the cell population density monotonically decreased while the cell size first increased to maximum when T_{sat} raised to the range of 127 to 131^{o}C and subsequently decreased as T_{sat} further increased to 135^{o}C. At low T_{sat}, the nanocomposite's structure was very rigid, and this restricted the cell growth and suppressed cell wall rupture. This led to a decrease in cell size and an increase in cell population density. As T_{sat} increased continuously to an optimal level, the cell size increased while the cell population density gradually decreased. This could be explained by the increase in gas diffusivity, which led to faster cell growth, more rapid gas loss to the surrounding, and an increased chance of cell wall. When T_{sat} continues to increase beyond the optimal T_{sat}, severe cell wall rupture led to a significant decrease in cell population density.

Furthermore, the cell size also decreased due to cell collapse caused by significant gas loss to the surrounding.

Figure 5.6 (c) shows that the initial loadings of MWCNT (i.e., ranging from 2 wt.% to 10wt.%) had insignificant effects on both the cell size and the cell population density for nanocomposite foams prepared at P_{sat} of 13.8 MPa and T_{sat} of 127°C. While nanocomposite foams were successfully prepared at these MWCNT loadings, neat HDPE, or nanocomposite with lower loading (i.e., 1 wt.%) were not able to foam due to the melting and collapse of the resultant foam structures after the ScCO2 foaming process at this level of 127°C. Experimental results revealed that at the optimal T_{sat} the cell size and cell population density were not substantially influenced by the initial loading of MWCNT.

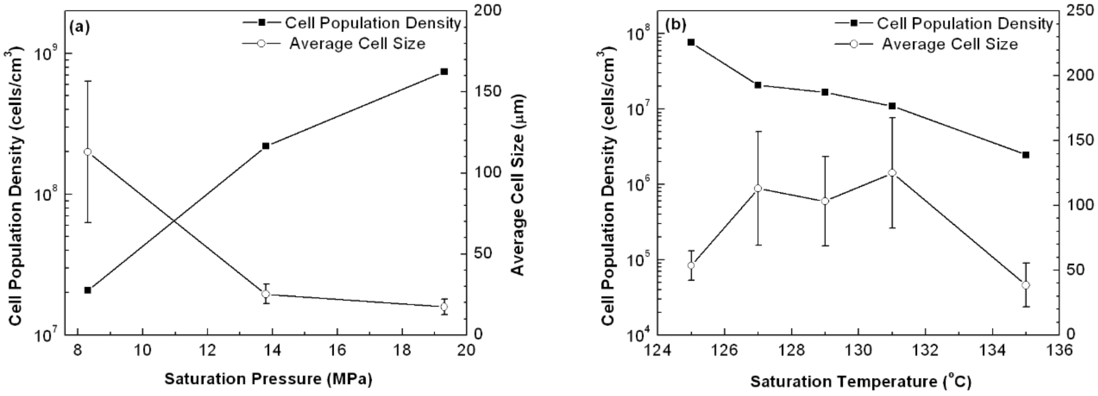

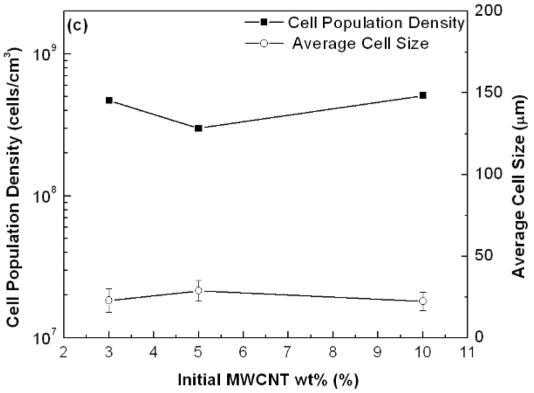

Figure 5.6 Cell size and cell population density depending on:

(a) saturation pressure at T_{sat} *of 127°C of the samples of 3 initial wt.% of MWCNT;*

(b), saturation temperature of 3 wt.% of MWCNT initially at P_{sat} *of 8.3 MPa; and*

(c) initial MWCNT wt.% at P_{sat} *of 13.8 MPa and* T_{sat} *of 127 °C.*

5.6 Measurement of Electrical Conductivity Methodologies

The electrical conductivity of solid HDPE/MWCNT nanocomposite samples was measured by the two-probe technique using a multifunctional source meter (Keithley, 2450 Source Meter). The two-probe technique was performed in accordance with the ASTM D257-07 standard. By printing conductive silver-epoxy paste as electrodes on both ends of a sample, the voltage difference was introduced through the wires and the flowing current was recorded to calculate the electrical conductivity of the nanocomposite sample. Figure 5.7 illustrates the nanocomposite samples prepared for the two-probe technique in two different directions: through-the-thickness and in-plane.

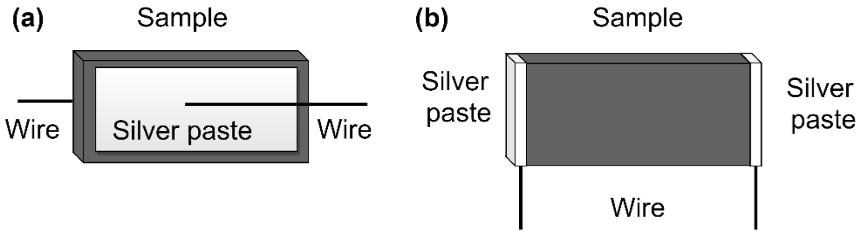

Figure 5.7 Protocol of nanocomposite samples prepared for electrical conductivity measurement by two-wire technique in: (a) through-plane; and (b) in-plane directions.

In the measurement of electrical conductivity, there are two distinct directions of current flow: in-plane and through-the-thickness of the specimen. The measured electrical conductivities of in-plane and through-the-thickness were shown in Figure 5.8. The samples demonstrated anisotropic electrical conductivity. The through-the-thickness conductivity was several orders of magnitude lower than that of the in-plane conductivity. This is in-line with previous works reported in the literature using other conductive fillers such as graphene [89], and carbon fiber [90]. This demonstrated how fabrication processing affects the electrical conductivity. Under compression-molding, the melted material flew in-plane to fill the mold. The fillers tended to align in the in-plane direction, hence promoting the electrical conductivity. Remarkably, the through-the-thickness data did not follow the expected trend as the in-plane data did. There are two sets of measurements, which have the same range of thickness but different in relative density (equivalently, different in the volume-expansion ratio), listed in Table 5.5. The through-the-thickness electrical conductivity was not only dependent on the volume-expansion ratio but also strongly relied on the thickness of the foamed samples. Therefore, to be consistent with the relative-density dependence, the electrical conductivity mentioned after this section was conducted in the in-plane direction.

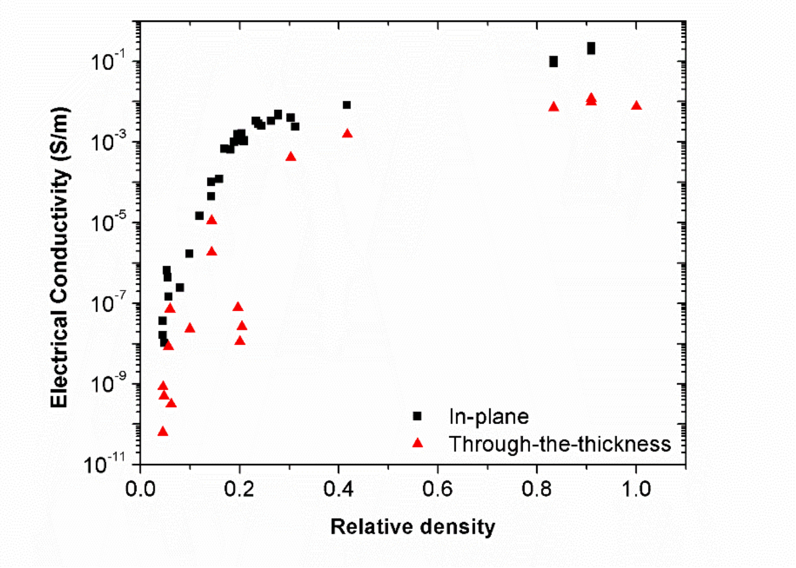

Figure 5.8 Electrical conductivity measurement by through-plane in-plane methods of 3-initial-wt.% nanocomposite foams.

Table 5.5 Electrical conductivity of thick nanocomposite foam samples.

Thickness (nm)	***Relative density***	***Through-the-thickness electrical conductivity (S/m)***	***In-plane electrical conductivity (S/m)***
2.2	0.200	1.12×10^{-8}	1.09×10^{-3}
2.0	0.204	2.61×10^{-8}	1.62×10^{-3}
2.3	0.196	7.76×10^{-8}	1.24×10^{-3}
2.1	0.045	8.45×10^{-10}	1.62×10^{-8}
2.4	0.044	6.28×10^{-11}	3.60×10^{-8}

The electrical conductivity for the rest of this study is **in-plane**.

5.7 Effects of Foaming Conditions on Electrical Conductivity

In order to compare the structure-to-property relationships of solid and foamed nanocomposites, the loadings of MWCNT were converted from weight fraction to volume fraction by considering the MWCNT density to be 1.75 g/cm^3 [43, 88]. The volume fraction of MWCNT in foamed samples was calculated with respect to the total volumes of the solid part and the voids. Figure 5.9 presents the effects of volume fractions of MWCNT on the electrical conductivity of HDPE/MWCNT nanocomposites and their foams at different initial MWCNT loadings (i.e., 3, 5, and 10 wt.%). While the weight percent of MWCNT in a nanocomposite was not affected by foam expansion, the volume percent of MWCNT decreased as the volume-expansion ratio of the foams increased. Therefore, for nanocomposite foams with the same volume percent of MWCNT, the one prepared with a higher initial weight percent of MWCNT had a higher volume-expansion ratio. Experimental results revealed that the electrical conductivity of both solid nanocomposites and foamed nanocomposites increased with the final volume fraction of MWCNT regardless of the initial weight percent of MWCNT as expected. It is most important to note that for resultant foams with the same volume percent of MWCNT (i.e., the same amount of MWCNT per unit volume of the structure), the initial weight percent of MWCNT loadings significantly affected the nanocomposite foams' electrical conductivities.

Experimental results indicated that for nanocomposite foams, with a constant resultant low volume percent of MWCNT (i.e., achieved by large volume expansion), the electrical conductivity of foamed samples was remarkably higher than the solid samples. This increase was more significant for nanocomposites with higher initial MWCNT loading in weight percent. As shown in Figure 5.9 (b), for all nanocomposite foams filled with 0.3 vol.% of MWCNT in the resultant foams, the electrical conductivity of the nanocomposite foam sample initially loaded with 10 wt.% of MWCNT (note: expanded by 18.1 times) was five orders of magnitude higher than that of the solid sample. This was also two orders of magnitude higher than that of the nanocomposite foam sample initially loaded with 3 wt.% of MWCNT (note: expanded by 5.3 times), and one orders of magnitude higher than that of the nanocomposite foam sample initially loaded with 5 wt.% of MWCNT (note: expanded by 9.1 times). In other words, at the same MWCNT vol.% in the resultant nanocomposite foams, higher initial MWCNT loading together with higher volume-expansion ratio could promote the electrical conductivity of the material system with the same loading of MWCNT per unit volume, and thereby could reduce material costs. This structure-to-property relationship can be explained by the initial phase morphology of HDPE/MWCNT nanocomposite before foaming. At high initial loading of MWCNT, uniform dispersion of MWCNT was virtually impossible. Therefore, higher degrees of local MWCNT agglomeration were unavoidable in nanocomposites with higher MWCNT loadings. Through biaxial stretching during foam expansion, these highly entangled networks of MWCNT become more compact and aligned along with the three-dimensional structures of the cell walls. This resulted in a highly interconnected three-dimensional electrically conductive network throughout the entire nanocomposite foam structure. In short, foaming nanocomposites with high initial loadings of MWCNT could serve as an effective strategy to produce light-weight polymer nanocomposite materials with a low loading of MWCNT per unit volume but enhanced electrical conductivity.

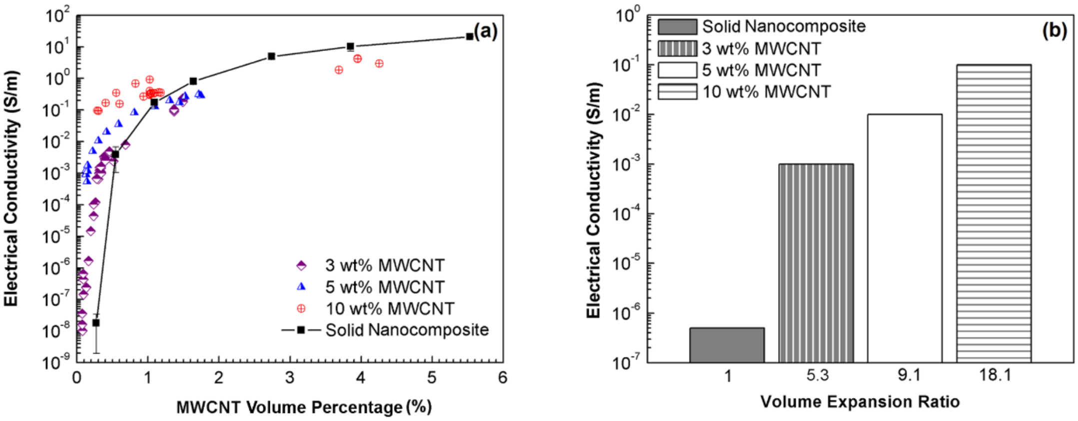

Figure 5.9 Electrical conductivity of HDPE/MWCNT composites and their foams loaded at different contents: (a) overview of all measurement; and (b) only at 0.3 vf.%.

5.8 Effects of Foaming Conditions on Percolation Threshold

Figure 5.10 illustrates the effect of the foaming process on reducing p_c of HDPE/MWCNT nanocomposites. Experimental results indicated that p_c of HDPE/MWCNT nanocomposites significantly decreased after foaming, while initial MWCNT content was a critical factor in suppressing the p_c of the nanocomposite foams. By increasing the initial MWCNT loading of the nanocomposite specimens from 3 wt.% to 10 wt.%, the nanocomposite's p_c decreased from 0.09 vol.% to 0.04 vol.%. While the solid nanocomposite's p_c was estimated to be 0.67 vol.%, which was higher than the values reported in the literature [16, 43], the p_c of nanocomposite foams was much lower. This significant reduction in p_c suggests that a lower loading of MWCNT per unit volume in nanocomposite foams was required to transform the nanocomposites from electrically insulating to conductive. Such improvements via the foaming process result in cost-

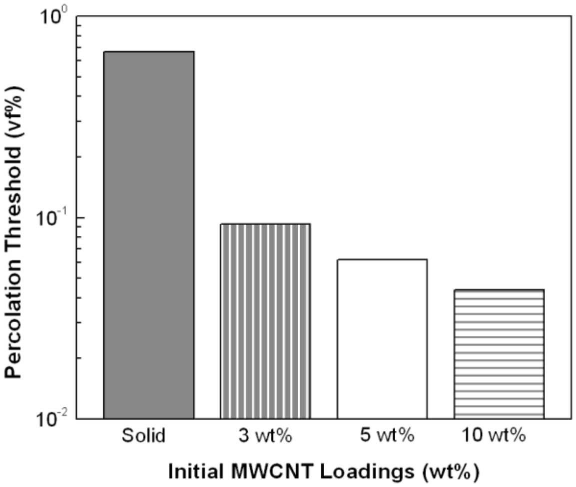

Figure 5.10 Fitted percolation threshold for nanocomposites and their foams with different initial loadings.

efficiencies for the fabrication of electrically conductive-filler-reinforced polymer-based nanocomposites.

5.9 Conclusions

In this chapter, the effects of physical foaming on the electrical conductivity and the percolation threshold of HDPE/MWCNT nanocomposites were investigated. By changing the saturation temperature, one of the governing physical foaming parameters, the effects of foam morphology and volume-expansion ratio on the electrical conductivity of the foamed samples were also explored. The foam morphology, including cell size and cell population density, and the volume-expansion ratio of nanocomposite foams were crucially dependent on both saturation temperature and initial loadings of MWCNTs in nanocomposites. The electrical conductivities of nanocomposite foams were significantly higher than their solid counterparts with the same loading of MWCNT per unit volume, especially at low MWCNT volume percent. The enhancement of the electrical conductivity was more pronounced for nanocomposites with higher initial MWCNT loadings before the material systems achieve the reduced loading of MWCNT per unit volume after foaming. This processing strategy also led to lower percolation thresholds in the material systems than their solid counterparts and thereby represented a viable path to the cost-effective fabrication of electrically conductive-filler-reinforced polymer nanocomposites.

Chapter 6 EXPERIMENTAL VALIDATION

Summary: In this chapter, the models for simulating the electrical conductivity of CPNs and their foams are verified by comparing the simulation results with the experimental data. Furthermore, possible factors that contributed to the discrepancy between simulation and experimental data are discussed.

6.1 Introduction

The models for simulating the electrical conductivity of both the polymer nanocomposites and their foams are validated against experimental results. The goal was to validate the new approaches of implementing existing models [1, 2, 53] (i.e., nanocomposites and their foams with low volume-expansion ratios) and the new model (i.e., nanocomposite foams with high volume-expansion ratios). The input parameters were obtained either from experimental measurements or from literature.

6.2 Electrical Conductivity of Polymer Nanocomposites before Foaming

The CPNs being considered in the comparison were HDPE/MWCNT nanocomposites. The input parameters for the simulation were obtained from the technical datasheet provided by the material manufacturers as well as literatures [15, 78, 79, 91]. These parameters are summarized in Table 6.1. The sensitivities of them in simulation were reported in [14, 52, 92-94], and the intrinsic electrical conductivity of CNT was found to be the most sensitive parameter and can not measure directly in our experiment. Besides the given aspect ratio, i.e., the average length and diameter of MWCNT, by the manufacturer, the other unknown parameters were chosen to be similar to other authors' simulations. Once the parameters were fitted in the simulation of CPNs before foaming, this set of configurations is transferred without any modifications to use in foaming simulation to maintain consistency.

Table 6.1 Input parameters of simulation before foaming.

Property	**Symbol**	**Value**	**Unit**
Intrinsic electric conductivity of MWCNT	$\boldsymbol{\sigma_{CNT}}$	1000	S/m
Average length of MWCNT	$\boldsymbol{L_{CNT}}$	800	nm
Average diameter of MWCNT [86]	$\boldsymbol{D}$	9.5	nm
Number of conduction channels [15]	$\boldsymbol{M}$	460	
Density of MWCNT [43, 88]	$\boldsymbol{d}$	1.75	g/cm^3
The height of energy barrier [15]	$\boldsymbol{\Delta E}$	1	eV
Cut-off distance [15]	$\boldsymbol{d_{cutoff}}$	1.4	nm
Van der Waals distance [15]	$\boldsymbol{d_{vdw}}$	0.34	nm

Figure 6.1 presents both the simulation and experimental results of the electrical conductivity of CPNs as a function of MWCNT loading of 0 to 5.5 vol.%. Three models, which were based on different boundary condition approaches, produced similar data. Based on the one-order of magnitude analysis, it can be observed that the simulation and experimental results were consistent with each other. It must be noted that the fabrication of CPNs with desired MWCNT loading was in terms of weight fraction (i.e., wt.%). In order to convert the MWCNT loading from weight fraction to volume fraction, the

MWCNT density was considered to be 1.75 g/cm^3 [43, 88]. The number of conduction channels as well as the values of the height of the energy barrier, cut-off distance, and Van der Waals distance were obtained from literatures [14, 15, 53, 61]. Because the process of diluting CNT loading broke CNTs and reduced the average length of CNTs [77, 91], the average length of CNTs used in the simulation was 800 nm, instead of the original average length of 1500 nm as stated by the masterbatch's manufacturer [86].

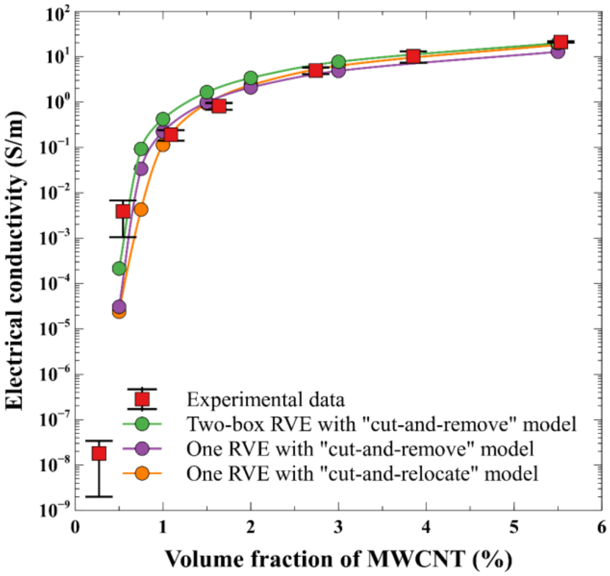

Figure 6.1 Electrical conductivity values simulated and measured experimentally.

Experimental data were used to obtain the fitting parameters of the predictive equation (i.e., Equation **(6.2.1)**) for the percolation theory. These include $\boldsymbol{\sigma_0}$ = 4077 S/m and $\boldsymbol{p_c}$ = 0.0067 or 0.67%, and t = 1.74. It must be noted that $\boldsymbol{p_c}$ represents the percolation threshold in volume fraction and the critical exponent t is related to the dimensionality of the system (note: in a three-dimensional system, the value of t is expected to be approximately 2 [64, 65]). The percolation threshold was found to be 0.67 vol.%, which was equivalent to 1.22 wt.%.

$$\boldsymbol{\sigma = 4077 \times (p - 0.0067)^{1.74}} \qquad \textbf{(6.2.1)}$$

6.3 Electrical Conductivity of Polymer Nanocomposite Foams

The input parameters for the simulation of polymer nanocomposite foams were the same as those used in the previous section. Other input parameters related to the foam structures were obtained experimentally and they are summarized in Table *6.2*. The most important parameters were the average size of foam cells, which was determined from SEM micrographs, and the volume-expansion ratio. These were important parameters and were used to calculate the dimensions of RVE, which were in the length scale as a multiple of $\boldsymbol{L_{CNT}}$, of the simulation before foaming. The last column of the table shows that the size of the unfoamed RVE was substantially larger than the average length of MWCNT. In contrast, the wall thickness of the foam cell was only a few times greater than the average length of MWCNT. The conversion from weight fraction to volume fraction was discussed in the previous section. During the foaming process, the weight fraction of MWCNT was virtually unchanged as the mass of air in the void was negligible. However, the volume fraction of MWCNT reduced as the volume-expansion ratio increased. It can be observed that different degrees of volume expansion can lead to two nanocomposites, which have significantly different initial MWCNT loadings, yield very similar post-foaming volume fraction of MWCNT.

Table 6.2 *Experimentally parameterized configuration for foaming simulation.*

		Experimental input		**Calculated input**	
w.t.%	**v.f.%**	**Volume-expansion ratio**	**Cell size (µm)**	**Wall thickness (µm)**	**RVE in scale of L_{CNT}**
5	0.301	9.1	53	2.10	32
5	0.127	21.6	125	1.99	56
10	0.728	7.6	51	2.46	32
10	0.306	18.1	105	2.01	50
10	0.249	22.2	160	2.48	71

Figure 6.2 illustrates the simulation results and experimental data of the CPN foam's electrical conductivity versus the post-foaming volume fractions of MWCNT. It can be observed that there exists a satisfactory agreement between the simulation results and the experimental data. Using the percolation theory, the fitting curves for the electrical conductivity were plotted for both sets of data. The simulation included both outcomes at low volume-expansion ratios using volume fractions from 3.5% to 5% and at high volume-expansion ratios with volume fractions below 1%. In the case of low volume-expansion ratio, the model used the size of RVE of [5.0, 5.0, 5.0] × L_{CNT} and with a spherical cell. In the case of high volume-expansion ratios, the cubic model was adopted in the simulation. The simulation data yielded a smooth transition from the low volume expansion cases to the high-volume expansion cases. They matched well with the experimentally measured electrical conductivity.

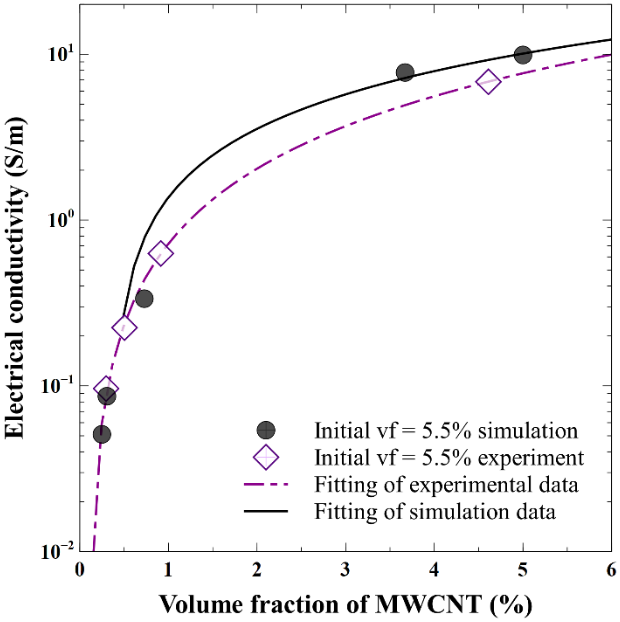

Figure 6.2 Electrical conductivity dependence of foamed CPNs on volume fractions.

As shown in Figure 6.3, there also exists a smooth transition from simulation results for foams with low volume expansion and those with high volume expansion for nanocomposites with an initial MWCNT loading of 2.7 vol.%. Although the magnitude differences between the simulation results and the experimental results are less than an order, it can be observed a more significant discrepancy when compared to the case of nanocomposites foams with an initial MWCNT loading of 5.5 vol.%. This discrepancy will be discussed in the next section.

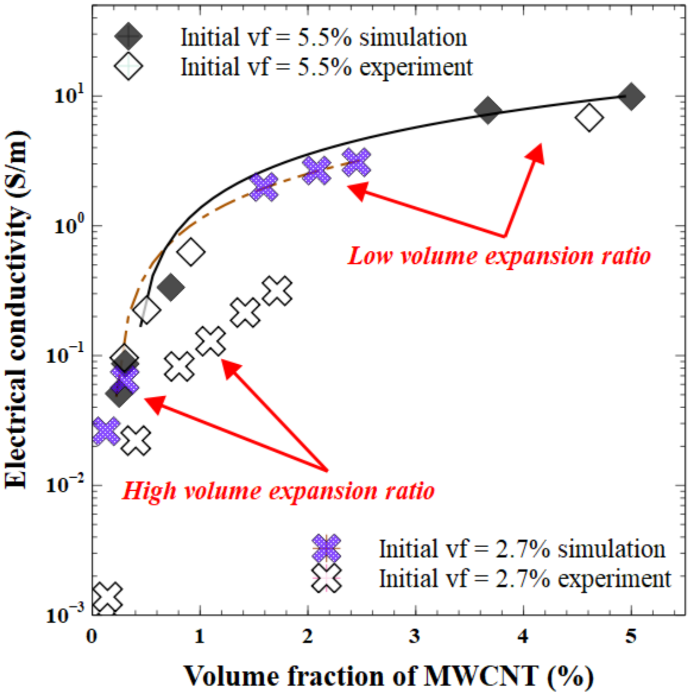

Figure 6.3 Electrical conductivity dependence of foamed CPNs on volume fractions at different initial volume fractions of 5.5% and 2.7%

6.4 Discrepancies in Electrical Conductivity after Foaming

The SEM micrograph shown in Figure 6.4 reveals that the thicknesses of the walls of foam cells were not uniform, with most of them being very thin, and few of them being abnormally thick.

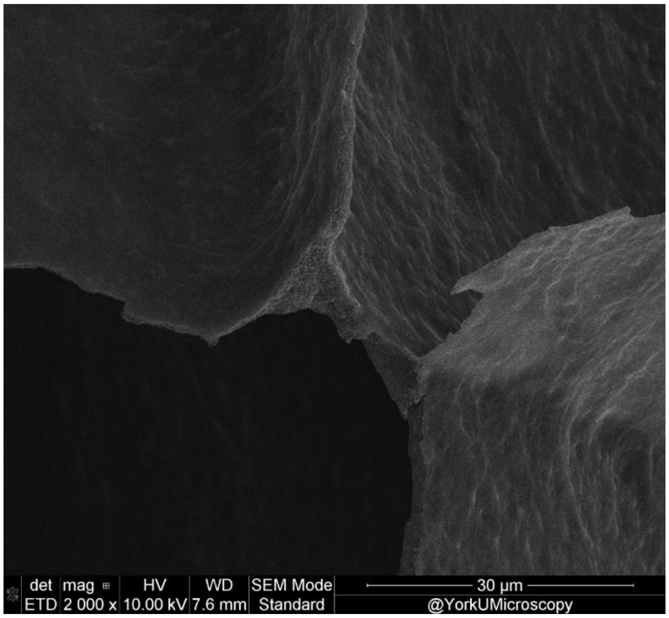

Figure 6.4 Illustration of uneven thickness of cell walls.

Table 6.3 summarized the measurements of thin and thick walls of foam cells for several initial volume fractions at various volume-expansion ratios. The range of cell wall thicknesses for the thin walls was estimated to be from 0.08 to 0.14 μm, which was extremely small compared to the average length of 1.6 μm of MWCNTs. The estimation was done roughly due to the limitation of the resolution of SEM images at the nanoscale, and some of them have high uncertainties. In comparison to the average diameter of 0.0095 μm of MWCNTs, the thin wall was stacked up approximately 10 CNTs. These conditions absolutely impacted the total electrical conductivity contributed by other normal-thickness walls of foam cells. The normal thickness is defined as the thickness calculated based on the foam-cell size and the volume-expansion ratio only, which is presented in the third last column in Table 6.3.

Table 6.3 Measurements of thin and thick walls of foam cells.

Initial CNT wt.%	Volume Expansion	Cell size (μm)		Thin wall measurement (μm)		Thick wall measurement (μm)	Estimated thickness (normal thickness) (μm)	# of walls (Estimation)	
		Average	Std Dev	Average each sample	Average whole expansion ratio			Thin walls	Thick walls
3	6.1	53	11	0.09	0.08	3 ± 1	3.3	40	20
5	6	29	6	0.11		1.5 ± 0.9	1.8	50	10
10	5.1	22	6	0.05		1.5 ± 0.5	1.7	50	15
5	9.1	54	16	0.11	0.1	N/A	2.1	40	20
10	7.6	51	14	0.09		4.4 ± 1.4	2.5	40	10
3	23.3	113	44	0.2	0.14	2 ± 1	1.7	40	10
5	21.6	125	28	0.07		3.5 ± 1.5	2	50	10
10	22.2	160	33	0.15		3 ± 0.5	2.5	40	10

The effect of thin walls on electrical conductivity was simulated in Figure 6.5 plotted together with experimental data for the case of initial volume-fraction of 1.6%. The normal thickness in simulation, in which no thin walls are considered, and the size of RVE after foaming was based on experimental measurements. The electrical conductivity in terms of normal thickness was a two-order-of-magnitude difference from the thin wall.

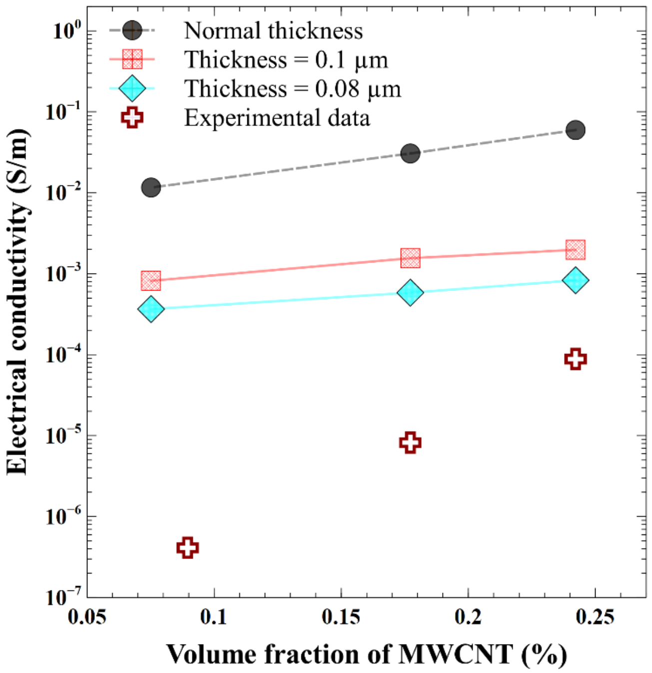

Figure 6.5 Electrical conductivity dependences on thickness of walls of foam cells of both simulation and experiment of an initial volume-fraction of 1.6%.

To determine the dependence of thickness on initial volume-fraction, the differences in the order of magnitude of electrical conductivity were calculated for cases of thin wall, referred to as normal thickness, and are illustrated in Figure 6.6. There were two major conclusions about the impact of thin wall thicknesses of foam cells on the electrical conductivity: the impact was more at lower initial volume-fraction and low volume-expansion ratio, i.e., high volume-fraction. The impact of thin-thickness foam cell is explained why the simulation of initial volume-fraction of 2.7% was less compared to the experimental result that the case of 5.5% at high volume fraction as shown in Figure 6.3.

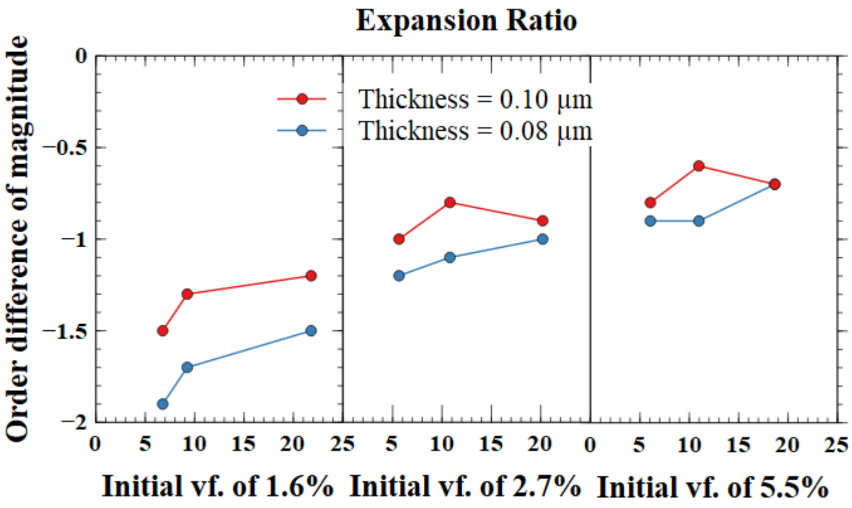

Figure 6.6 Order differences of magnitude of electrical conductivity in cases of thin wall from normal thickness for various initial volume-fraction.

6.5 Conclusions

Experimental results were used to validate the models that were used to simulate the electrical conductivity of CPNs before and after foaming. The experimental data were well matched to the simulation results. In particular, the foaming expansion of CPNs could be modeled for both low and high volume-expansion ratio. The curve-fitting percolation threshold showed a smooth transition of electrical conductivity from low to high volume-expansion ratio, which clarified the two-case model for the foaming process. In addition, the model is validated by the experimental data, especially at high initial vf. However, the thickness of the cell wall was found to be heterogeneous experimentally, which caused sharp drops of low initial vf. at the low expansion ratio. The explanation was discerned by simulating cases of thin wall with the same size of foamed RVE.

Chapter 7 PIEZORESISTIVITY OF CPNS AND FOAMS

Summary: In this chapter, the applications of CPNs and their foams as sensors are demonstrated. A dynamic mechanical analysis was conducted on the fabricated samples and experimental results were presented to highlight their piezoresistivity.

7.1 Introduction

Polymers, such as high-density polyethylene (HDPE) or thermoplastic polyurethane (TPU), are insulating but can be turned into electrically conductive material systems by dispersing more than one type of conductive fillers. The hybrid fillers are a compound of carbon nanotube (CNT) and graphene nanoplatelet (GnP). These fillers form conductive networks in a polymer matrix and the degree of networking depends on the type of filler, the structure of the polymer, and the mixing process. Furthermore, the conductive filler network can be reconfigured by applied strain and/or stress. These materials can be used in sensors such as strain gauges [95-97], or wearable strain sensor [35, 98].

The dimensions of the filler also strongly impact the electrical properties of the CPN [95]. CNT, which is one-dimensional at the nanoscale, would increase CPN’s conductivity if it is uniformly dispersed in the polymer matrix. The disadvantage of CNT has been its cost, which has limited its applications. In contrast, GnP is cheaper due to high productivity. For the nanocomposite containing hybrid filler of CNT and GnP, it has been shown that their synergistic effect helps promote the material system's electrical conductivity. For example, the electrical conductivity of CPN comprised 1% GNP and 1% CNT was found to be two orders of magnitude higher than that of nanocomposites filled with 2 wt.% GNP alone [99].

This chapter provides the findings of a comprehensive study of the piezoresistive behavior of HDPE/TPU nanocomposites filled with different loading ratios of CNT and GnP and their foams, demonstrating their potential applications in the sensor field. Furthermore, the effects of CNT-to-GnP ratio on CPN's structural morphology, foaming behavior, electrical conductivity, and piezo-resistivity were investigated. The study found that the presence of GnP had dominant influences on the foaming behavior and the gauge factors of CPN.

7.2 Material Preparations

Commercially available HDPE/MWCNT nanocomposite masterbatch (Nanocyl, Plasticyl HDPE1501), loaded with 15 wt.% MWCNT (Nanocyl, NC7000^{TM}), and neat HDPE (NOVA Chemicals, SCLAIR$^{®}$ 2710) were used to prepare HDPE/MWCNT nanocomposites of different MWCNT loadings. The constituent MWCNT had an average length of 1.5 μm and an average diameter of 9.5 nm. The physical foaming agent used in this study was carbon dioxide (CO_2) (Linde Gas Inc., 99.8% purity). Commercially available TPU (Estane® 2103-70A TPU, Lubrizol) was used as the second component in the CPN. It is a block copolymer consisting of alternating sequences of isocyanate- and polyether-based polyol. Graphene nanoplatelets (GnP, Grade 2, CheapTubes, Cambridgeport, MA, USA) were dispersed with MWCNT to desired ratios. All materials were used as received without any modification.

TPU was blended with HDPE to soften the material [100] to enhance the piezoresistive behavior. However, an extensive amount of TPU would cause challenges to create good foam structures, due to the differences in the working-temperature range. The ratio of HDPE-to-TPU ratio was maintained at 60:30 while the filler contents (i.e., GnP and/or MWCNT) was fixed at 10 wt.%. The neat HDPE was added to maintain the ratio of the blends. GnP in powder form is challenging to uniformly disperse in common polymer matrices [101, 102]. The HDPE masterbatch was used to ease the distribution of GnP in the polymer resin. The CNT-to-GnP ratios were set to 0:10, 2.5:7.5, 5:5, 7.5:2.5, 10:0 in order to determine the effects of hybrid fillers on piezoresistive behavior.

7.3 Experiment and Foaming

First, calculated amounts of HDPE/MWCNT nanocomposite masterbatch were weighed and the MWCNT content was reduced to various levels by adding different amounts of neat HDPE to maintain the sample’s HDPE-to-TPU to be 60:30 and GnP. The dilution was done by melt-compounding the mixtures using a micro-compounder (HAAKE™ MiniCTW Micro-Conical Twin Screw Compounder) in the circulating mode for 5 minutes at 215°C, with the screw speed set at 75 rpm. The extrudates were pelletized and compression molded into a circular disc sample of 115 mm in diameter and 0.50 mm in thickness using a compression molding machine (Craver Press, 4386 CH). The compression molding procedure is summarized below:

Step 1. A weighed amount of polymer-based nanocomposite pellets were loaded into a circular disc mold of 115 mm in diameter and 0.50 mm in thickness.

Step 2. The compression molding machine was equilibrated at 160^{o}C.

Step 3. The heat platens of the compression molding machine were brought into contact with the mold, which loaded with the nanocomposite pellets, for 5 minutes to ensure the complete melting of the nanocomposite pellets.

Step 4. The molding pressure was ramped up gradually to 27.6 MPa psi and held at this level for 6 minutes.

Step 5. The disc samples, which were still inside the mold, were transferred to a cooling module with flowing water channels to solidify the disc samples.

Step 6. The samples were cut into rectangular specimens with dimensions of 12 mm × 10 mm × 0.50 mm. The specimens were then characterized using an electrical conductivity analyzer or be foamed by $ScCO_2$.

After that, the nanocomposite foams were fabricated by a batch foaming chamber using CO_2 as the physical foaming agent. In the physical foaming process, nanocomposite specimens were saturated with $ScCO_2$ for 30 minutes at pre-set combinations of saturation pressure (P_{sat}) and saturation temperature (T_{sat}). Based on the theoretical calculation of saturation time, 30 minutes were enough to achieve 99% content of CO_2 in the polymer matrices. Subsequently, an outlet valve of the batch foaming chamber was opened to rapidly depressurize it. This led to thermodynamic instability in the HDPE/TPU/CNT/GnP/$ScCO_2$ system and induced cell nucleation and subsequent cell growth in the polymer matrices. Table 7.1 summarizes the key parameters being studied in the physical foaming experiments.

Table 7.1 Physical foaming experiment parameters.

Property	**Value**	**Unit**
CNT:TPU	0:10, 2.5:7.5, 5:5, 7.5:2.5, 10:0	wt.%
P_{sat}	8.3, 11, 13.7	MPa
T_{sat}	126 - 136	^{o}C
Saturation Time	30 (fixed)	min

Last, all the samples were characterized as in Section 5.2.4 Sample Characterization.

7.4 Characterizations of CPNs and Foams

Figure 7.1 presents the comparisons of samples before (a, c, e) and after (b, d, f) foaming at different CNT-to-GnP ratios. More GnP resulted in agglomeration, hence, preventing the cell expansion during the foaming period, eventually disordered the cell structure of the foamed samples. The GnP amount also influenced the volume expansion of the samples. In Figure 7.2 (a), high loading of GnP constrained the expansion of foamed nanocomposites. When the CNT-to-GnP ratio was higher than 0.5, the volume-expansion ratio increased dramatically. In the extreme case, the volume-expansion ratio of CPN consisted of only CNT was 10 times larger than that comprised of only GnP. Therefore, to achieve the desired expansion, the maximum loading of GnP needed to be controlled.

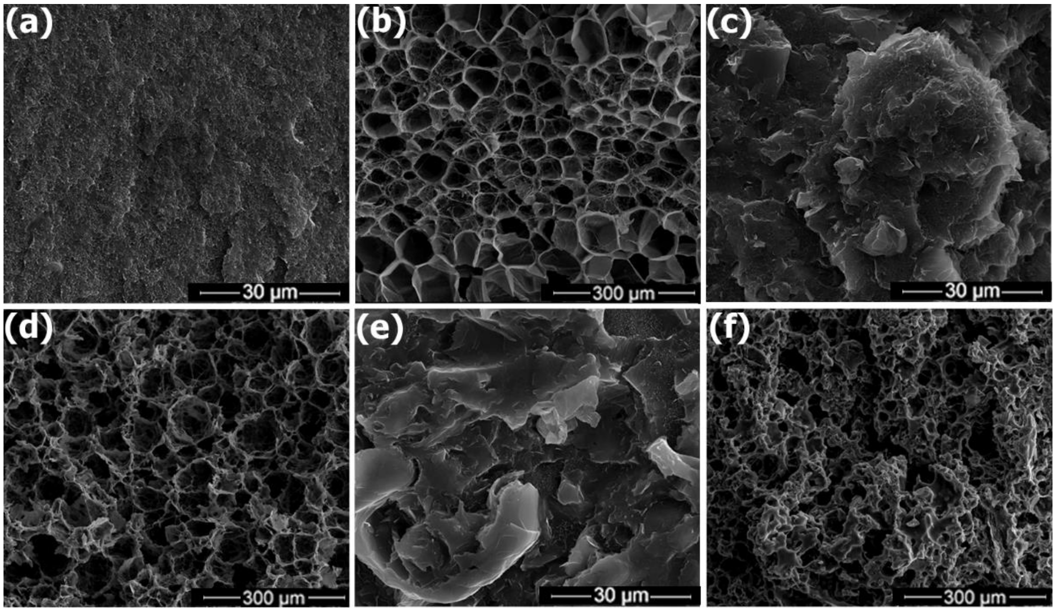

Figure 7.1: SEM Micrographs of nanocomposites (left column) and their foams (right column) with HDPE:TPU ratio of 60:30 and CNT:GnP ratio of (a, b) 10:0, (c, d): 5:5, and (e, f) 0:10.

Foaming temperature significantly affected the foam expansion, which was consistent with findings in other studies [103]. There is a critical temperature at which the volume-expansion ratio reached its maximum. As shown in Figure 7.2 (b), with CNT-to-GnP ratio of 5:5, the optimal foaming temperature was found to be 128^{o}C. When the temperature was too low, the structure of matrices was too stiff for foam expansion. In contrast, when the foaming temperature was too high, the structure was too weak to hold the gas, and the gas loss was elevated due to high diffusivity. Contrary to temperature influence, the saturation pressure had only slight impacts on the volume-expansion ratio as shown in Figure 7.2 (c).

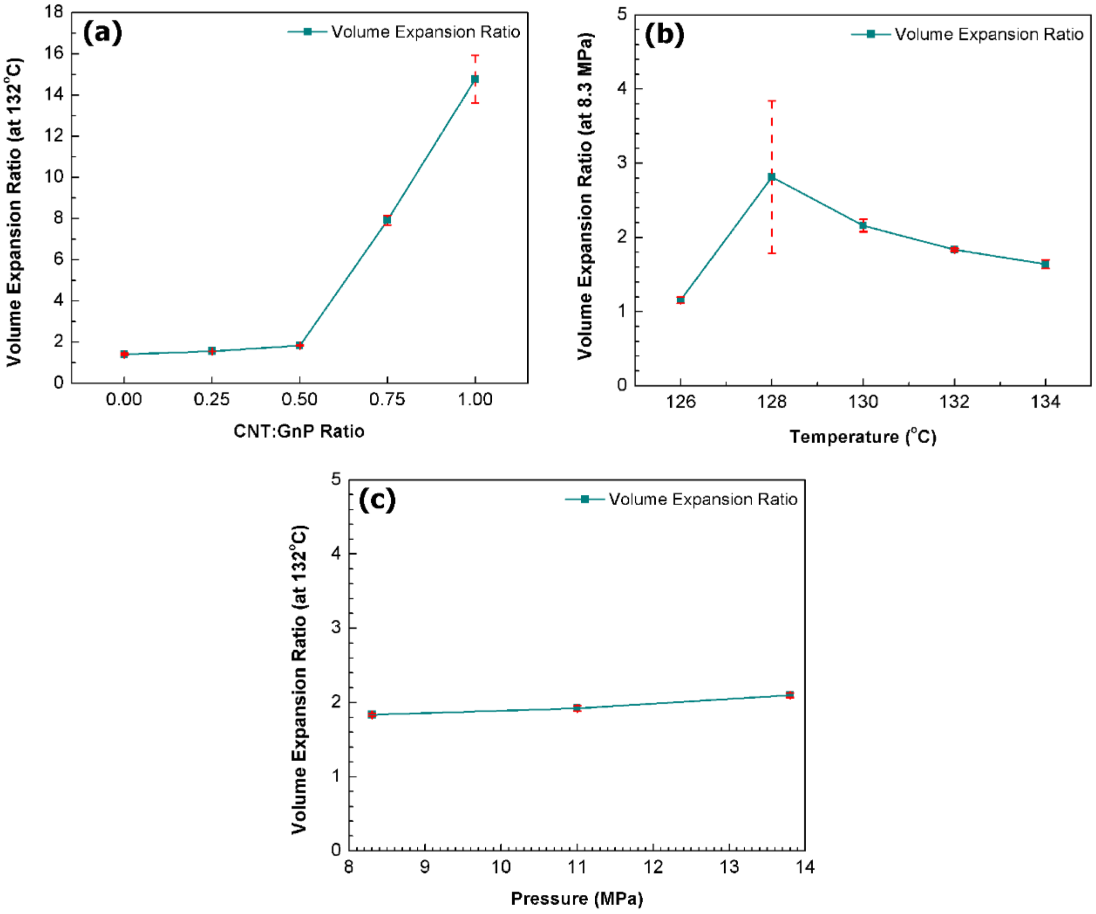

Figure 7.2 Volume-expansion ratio depends on (a) CNT:GnP Ratio at 132°C, (b) saturation temperature in case of CNT:GnP of 5:5, and (c) saturation pressure in case of CNT:GnP of 5:5.

Next, the cell population density and average cell size values were estimated for the different CNT ratios at the same saturation temperature of 132°C and pressure of 8.3MPa (Figure 7.3). A higher content of GnP decreased the cell size but increased the cell density. The GnP agglomerated and prevented gas to flow freely, consequently, created intervening structure as captured in Figure 7.1 (d) and (f).

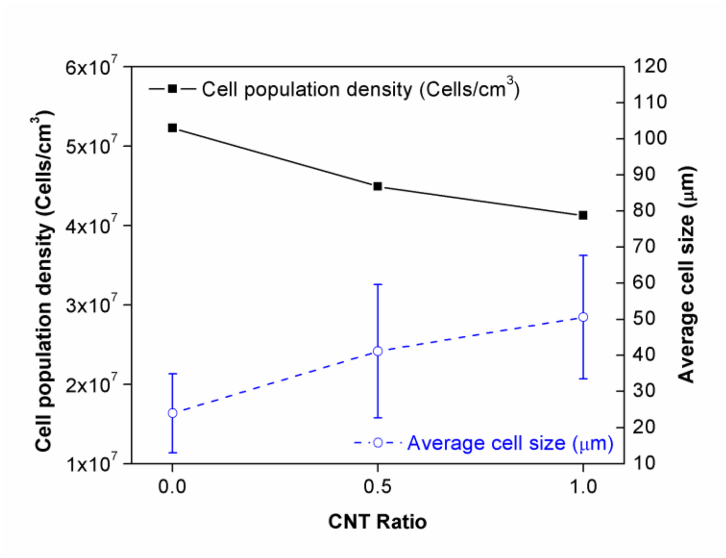

Figure 7.3 Cell population density and average cell size dependences on CNT ratio.

7.5 Piezoresistive Behavior

In the next step, the samples were characterized by a rheometer and the changes in resistance were tracked by a source meter. An example of relative resistance change over time was plotted (Figure 7.4) and compared to the strain applied to the sample. The resistance change was greatest in the first cycle, decreasing after, and the relative change in resistance plateaued after 50 cycles.

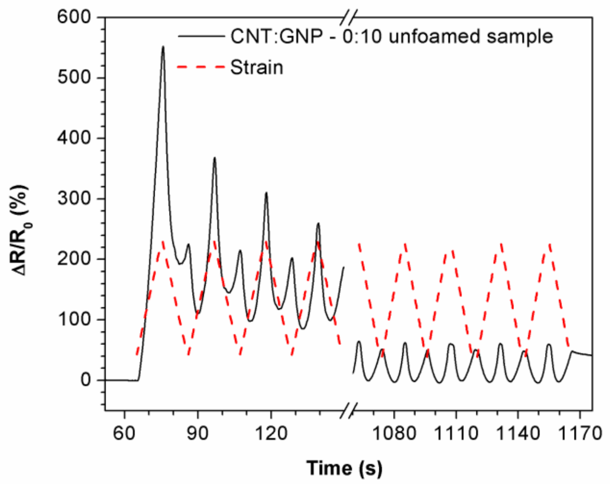

Figure 7.4: Relative resistance changes by time in comparison to strain applied.

In addition, experimental results show the existence of a second peak in the graph of relative change in resistance. This second peak was found between the loading-unloading cycle and is usually known as the “shoulder peak” [96, 104-106]. The “shoulder peak” was mainly caused by the conflict between the destruction and reconstruction of conductive networks formed by fillers during the loading-unloading cycle. In spite of that, the impact of the conflict was suppressed by foaming the CPN as demonstrated in Figure 7.5.

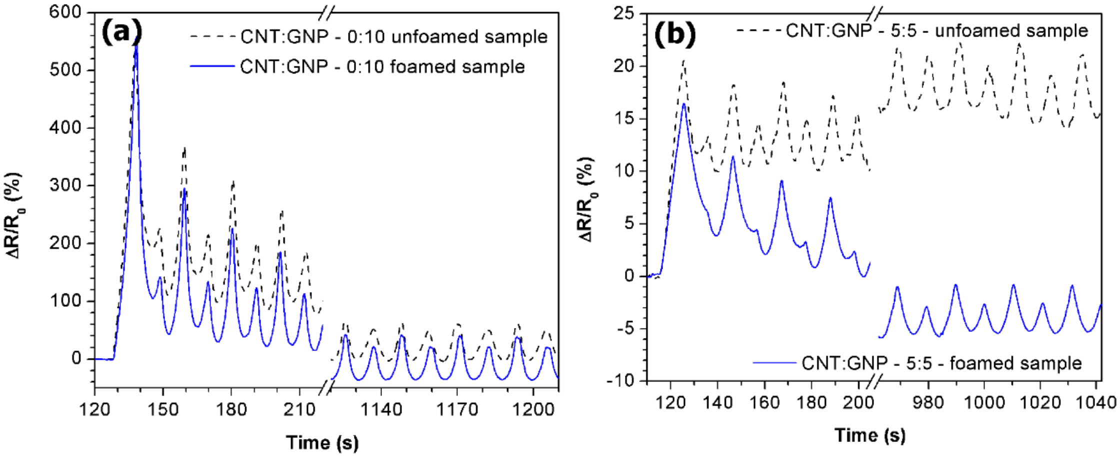

Figure 7.5. Relative resistance changes of materials before and after foaming at different CNT:GnP ratios of (a) 0:10 and (b) 5:5.

In summary, the average gauge factors were calculated for each CNT-to-GnP ratio and the data is reported in Figure 7.6. The study found that the gauge factor increased with GnP content. This may be explained by the uneven dispersion of the GnP fillers in the CNT connections which weakened the conductive network formed by conductive fillers.

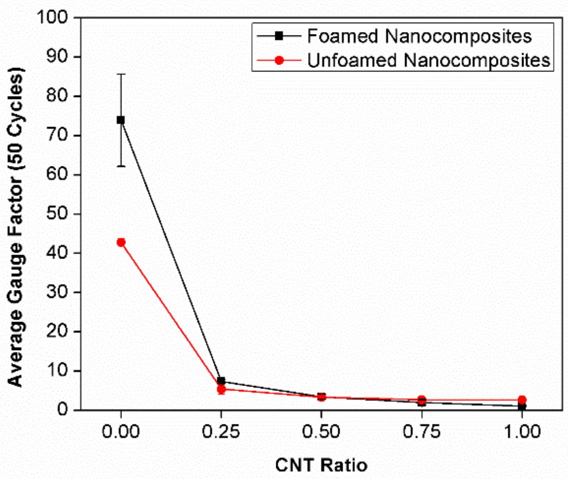

Figure 7.6 Average gauge factor after 50 cycles of strain.

7.6 Demonstrations of Applications as Sensors

Samples were used as sensors to track the change of current output while external strains were applied to the samples. The first demonstration, illustrated in Figure 7.7, is the tracking of a finger when it is bending. A sample sensor was stuck to the finger and connected with electrical probes to track the change in resistance while bending the finger. The output of the screen in the Figure 7.7 (a) shows the signal before bending the finger and the change of the resistance was captured after the finger was bent in Figure 7.7 (b). The demonstration was successful to prove the application of the material as a strain sensor and presented quick responses of output signal between movements.

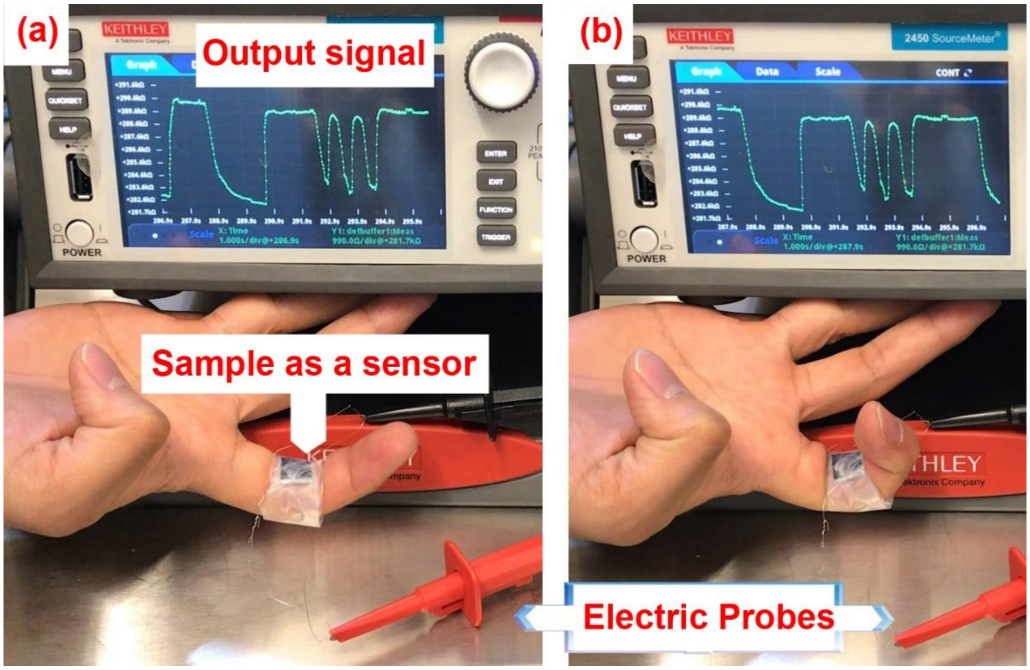

Figure 7.7 Demonstration of bending finger

Next, the material was demonstrated as a step-counting sensor. The setup is shown in Figure 7.8. The sample sensor was stuck underneath a shoe, and the output signal when the shoe was stepping on the floor was illustrated in Figure 7.9. The repeated pattern of the change in the resistance can be used to determine the steps and measure the frequency of steps.

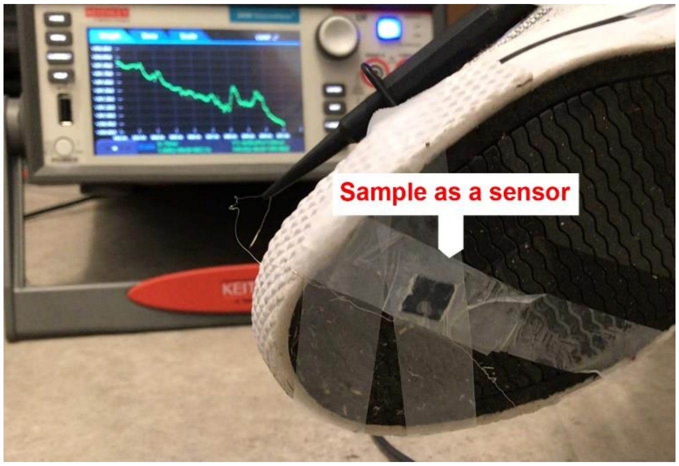

Figure 7.8 Setup of sensor which was stuck underneath the shoe.

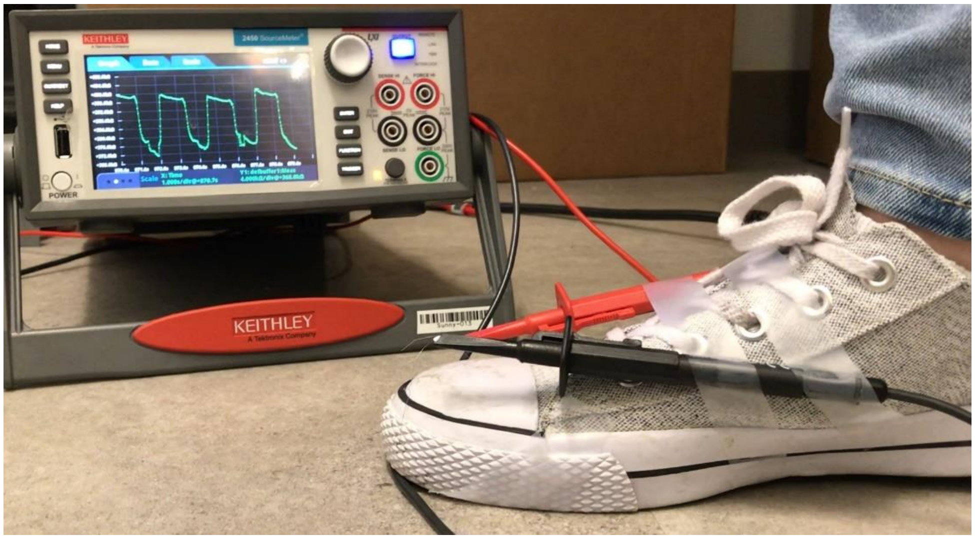

Figure 7.9 Output signal while stepping on the floor.

7.7 Conclusions

In this chapter, the effect of CNT-to-GnP ratio in CPN on its structural morphology, foaming behavior, and piezoresistivity was researched, followed by a demonstration of its suitability for use with sensors or various kinds. GnP was found to be the crucial factor in these properties, especially, in the gauge factor. Nonetheless, the GnP content dragged the electrical conductivity and required highly sensitive measurement. The agglomeration of GnP also restricted foam expansion because of the rigidity of the polymer matrix, leading to the formation of nonuniform cell morphology. The foaming did alleviate the “shoulder peak” and elevated the gauge factor in cases where the contents of GnP were more than CNT.

Chapter 8 CONCLUSIONS AND FUTURE WORK

Summary: This chapter summarizes the conclusions, contributions, and future research directions for the continuation of the current work.

8.1 Summary of Conclusions

The objectives of this research were to model the CPNs and foams and simulate their electrical conductivity. The models were verified experimentally by fabricating samples in both solid and foamed forms and characterized their electrical conductivity.

(i) Firstly, unfoamed CPNs were modeled and the simulation of their electrical conductivity was conducted. Parametric studies were done on factors including the size of the simulation volume, the boundary condition, and the distribution of length of MWCNTs with a view to understand the underlying mechanisms that govern electrical and mechanical properties of CPN. Past research assumed particular theoretical configurations, and the differences from the real situation contributed to the observed uncertainties in simulation. This research studied these common biases in simulation generally existed in models reported in the literature, then discussed and suggested improvements. It was demonstrated that the direction of the current flow needs enlarging to a sufficient but not infinite expansion, and that the 'cut-and-remove' was the best approach for boundary condition.

(ii) In the second phase of this research, CPN foams were modeled based on the incompressible property of a polymer matrix. The fillers were considered to move with the expanded volume and be constrained in the same unchanged volume, followed by the radial translation of the middles of the fillers from the central point of the foam cell. Based on the existing model reported in literature [1, 2], the foaming simulation performed at low volume-expansion ratios where the shapes of foam cells were spherical because the foam cells were free to expand and did not interfere with the neighboring cells kept growing symmetrically. Recently the distribution of fillers after foaming has been investigated and a newly published paper [82] in July 2020 also reported the use of such model to simulate the electrical conductivity and conductive network formation. Nevertheless, the model, due to the consideration of the spherical cell, was limited to cases where the volume-expansion ratio of the foam was low. This dissertation revealed the limitation of the existing model and developed a new model that can be applied for cases where the volume-expansion ratios are large enough for the adjacent cells to interfere with each other. Furthermore, a new mathematical scheme to solve the equations that describe the motion of CNT during expansion has been developed to simplify the simulation using the existing spherical model and also be applicable in the newly developed cubic model.

(iii) A state-of-the-art model was constructed by taking into consideration the underlying mechanisms that govern the electrical and mechanical properties of CPN at high volume-expansion ratios. It provided a model that can be applied in the extreme cases where the size of foam cells was greater than the average length of MWCNTs in several orders of magnitude. Large cells did not retain a spherical shape but interacted with adjacent cells and possessed distorted cell walls, leading to a polyhedral shape. As a result, one of the challenges for the theoretical studies of CPN foams with high volume-expansion ratios is the high-performance computing resources arising when the content of fillers exceeded the capacity of the computer. A new simulation scheme that subdivides a unit representative volume element into sub-units was implemented to overcome the difficulty. It simulates two different parts of the foam cell and the results can be combined to determine the effective electrical conductivity.

(iv) Ultimately, experiments were carried out and the characterization of CPNs was conducted to validate the theoretical models and suggested modifications. Initially, the samples were successfully fabricated in both foamed and unfoamed forms and their nano-and-microstructures, morphologies, and electrical conductivity behavior were analysed. Finally, the inputs for simulation were parameterized based on the experimental findings, and the model was tuned until it satisfied the actual configuration. There were uncertainties in electrical conductivity for different initial loadings of MWCNTs. These were explained by the uneven thickness of cell walls and it was noted that the impact was worse at lower initial content of fillers.

(v) Another contribution of this work is the study of the piezoresistive behaviors of

CPNs. The fabricated samples were oscillated by the dynamic stretching and compressing periods. These results demonstrated that the potential applications of CPNs and foams in the field of strained/pressure sensors.

8.2 Summary of Contributions

My first publication discussed the common biases in modeling the electrical conductivity of carbon nanotube–polymer nanocomposites and how to eliminate them. The findings provided insights into the uncertainties in simulation of CPNs, and investigations combining underestimation and overestimation using different hypothesized input parameters. The outcomes led to higher precision in the simulation of CPNs without excessive high-performance computing requirements.

Further research was undertaken [107] to enhance the electrical conductivity and determine the percolation threshold of microcellular HDPE/MWCNT nanocomposite foams. Experimental studies were conducted to fabricate samples of CPNs and foams, which were then characterized for morphology structures and electrical properties. Detailed investigation on foaming was completed in various experimental conditions including saturation temperature, pressure and the initial loading of MWCNTs. Extremely high volume-expansion ratios were achieved under low saturation pressure and adequate temperature, leading to a challenge in simulation to mimic the actual dimensions of a foam cell. This challenge has never been studied as a consequence of limited computing resources and the methods of handling foaming expansion.

This challenge was solved in this research using a state-of-the-art approach to the introduction of expanding fillers during the foaming process and using simulation of subdivided partition of the unit cell and later combined the result to determine the effective electrical conductivity. This approach would be able to reduce the costs of computing. The approach that addressed filler movements caused by cell growth during foaming was proved to be suitable and was validated experimentally for both low and high volume-expansion ratios. The low expansion cases were simpler due to the symmetric expansion of the spherical model, which was based on an existing model reported in the literatures [1, 2]. The cases at high expansion ratios were considered to have foam cells with cubic shapes, leading to asymmetric movements of fillers during foaming expansion. Simulated results for both the low and high expansion ratio cases were comparable to experimental measurements. The closest match was for CPN foams with higher initial filler loadings. The discrepancy found at lower initial filer loadings could be due to the impact of uneven thickness of the cell walls. The heterogeneous thickness of walls in foam cells was clearly observed in SEM micrographs. They illustrate some cell walls were very thick and many of the others were exceptionally thin and could be in the same magnitude of the diameter of MWCNTs.

Finally, an assessment of potential applications of CPNs and foams were studied and presented in the summer-research conference organized by Lassonde School of Engineering at York University, then the detailed work was published [108] at ANTEC conference held in Detroit, USA. The study proved that CPNs and foams were suitable for use in fields of force and pressure sensors from their greater conductivity and a more cost-effective form.

8.3 Scholarly Publication

(i) L.T. Hoang, Kyra, M., Leung, S.N., Zheng, H. Z., "Piezoresistive polymer nanocomposites and their foams as smart sensing materials", SPE, ANTEC, Conference Papers, Paper #261, Detroit, MI, USA, March 18-21, 2019.

(ii) L.T. Hoang, Siu N. Leung, and Zheng H. Zhu, “Enhanced Conductive Network Formation in Carbon Nanotube-Polymer Nanocomposites via Supercritical Carbon Dioxide Foaming”, 2018 6th International Conference on Mechanical, Automotive, and Materials Engineering held in the Hong Kong Polytechnic University

(iii) L.T. Hoang, S.N. Leung, Z.H. Zhu, Eliminating Common Biases in Modelling Electrical Conductivity of Carbon Nanotubes-Polymer Nanocomposites, PCCP (2018).

(iv) L.T. Hoang, M. Aghelinejad, S.N. Leung, Z.H. Zhu, High density polyethylene/carbon nanotube nanocomposite foams: electrical conductivity and percolation threshold, CSME international congress, York University, 2018.

(v) L.T. Hoang, Leung, S.N., Zheng, H. Z. Strategies to Enhance Electrical Conductivity and Suppress Percolation Threshold of HDPE/MWCNT Nanocomposite through Supercritical Carbon Dioxide Foaming. Composites Part C: Open Access, 2020. submitted.

8.4 Future Work

The research can be extended and continued addressing the following unresolved issues:

(i) The effects of the curvature of fillers on electrical conductivity behaviors after foaming. When the foam cells are expanding, the CNTs would be curved along the adjacent cell wall.

(ii) The shapes of foam cells would be more complicated than the cubic shape being considered in this study. The polyhedral structures can be octahedral, dodecahedral. The structures of the foam cells have been shown to influence by the expansion of CPNs and the distribution of conductive fillers.

(iii) Foaming and piezo-resistive behavior could be simulated for hybrid fillers, including CNTs and GNPs. Separate types of fillers have been widely studied [109] but the consequence of hybrid fillers has not been theoretically studied yet. Because CNT is 1D filler and GNP is 2D filler, it is therefore a much more complicated case that requires much more effort to develop a feasible model that demands reasonable computational power.

(iv) Besides this Finite-Element analysis, a recent study [110] took advantage of an artificial neural network to make predictions of the bulk conductivity of CPNs which shows very promising for future works.

BIBLIOGRAPHY

1. Shaayegan, V., A. Ameli, S. Wang, and C.B. Park, *Experimental observation and modeling of fiber rotation and translation during foam injection molding of polymer composites.* Composites Part A: Applied Science and Manufacturing, 2016. **88**: p. 67-74.
2. Wang, S., A. Ameli, V. Shaayegan, Y. Kazemi, Y. Huang, E.H. Naguib, and B.C. Park, *Modelling of Rod-Like Fillers' Rotation and Translation near Two Growing Cells in Conductive Polymer Composite Foam Processing.* Polymers, 2018. **10**(3).
3. Shaffer, M.S.P. and A.H. Windle, *Fabrication and Characterization of Carbon Nanotube/Poly(vinyl alcohol) Composites.* Advanced Materials, 1999. **11**(11): p. 937-941.
4. Kuilla, T., S. Bhadra, D. Yao, N.H. Kim, S. Bose, and J.H. Lee, *Recent advances in graphene based polymer composites.* Progress in Polymer Science, 2010. **35**(11): p. 1350-1375.
5. Li, J., P.C. Ma, W.S. Chow, C.K. To, B.Z. Tang, and J.K. Kim, *Correlations between Percolation Threshold, Dispersion State, and Aspect Ratio of Carbon Nanotubes.* Advanced Functional Materials, 2007. **17**(16): p. 3207-3215.
6. Gong, S., Z.H. Zhu, and Z. Li, *Electron tunnelling and hopping effects on the temperature coefficient of resistance of carbon nanotube/polymer nanocomposites.* Physical Chemistry Chemical Physics, 2017. **19**(7): p. 5113-5120.
7. Kim, H.M., K. Kim, S.J. Lee, J. Joo, H.S. Yoon, S.J. Cho, S.C. Lyu, and C.J. Lee, *Charge transport properties of composites of multiwalled carbon nanotube with metal catalyst and polymer: application to electromagnetic interference shielding.* Current Applied Physics, 2004. **4**(6): p. 577-580.
8. Leung, S.N., M.O. Khan, H. Naguib, and F. Dawson, *Multifunctional polymer nanocomposites with uniaxially aligned liquid crystal polymer fibrils and graphene nanoplatelets.* Applied Physics Letters, 2014. **104**(8): p. 081904.
9. He, T., X. Liao, Y. He, and G. Li, *Novel electric conductive polylactide/carbon nanotubes foams prepared by supercritical CO2.* Progress in Natural Science: Materials International, 2013. **23**(4): p. 395-401.
10. Rizvi, R. and H. Naguib, *Porosity and composition dependence on electrical and piezoresistive properties of thermoplastic polyurethane nanocomposites.* Journal of Materials Research, 2013. **28**(17): p. 2415-2425.
11. Alamusi, N. Hu, H. Fukunaga, S. Atobe, Y. Liu, and J. Li, *Piezoresistive Strain Sensors Made from Carbon Nanotubes Based Polymer Nanocomposites.* Sensors, 2011. **11**(11): p. 10691.
12. Obitayo, W. and T. Liu, *A Review: Carbon Nanotube-Based Piezoresistive Strain Sensors.* Journal of Sensors, 2012. **2012**: p. 15.
13. Imran, S.M., G.N. Shao, M.S. Haider, H.J. Hwang, Y.-H. Choa, M. Hussain, and H.T. Kim, *Carbon nanotube-based thermoplastic polyurethane-poly(methyl methacrylate) nanocomposites for pressure sensing applications.* Polymer Engineering & Science, 2016. **56**(9): p. 1031-1036.
14. Bao, W., S. Meguid, Z. Zhu, and M. Meguid, *Modeling electrical conductivities of*

nanocomposites with aligned carbon nanotubes. Nanotechnology, 2011. **22**(48): p. 485704.

15. Gong, S., Z.H. Zhu, and E.I. Haddad, *Modeling electrical conductivity of nanocomposites by considering carbon nanotube deformation at nanotube junctions.* Journal of Applied Physics, 2013. **114**(7): p. 074303.
16. Gong, S., Z.H. Zhu, J. Li, and S.A. Meguid, *Modeling and characterization of carbon nanotube agglomeration effect on electrical conductivity of carbon nanotube polymer composites.* Journal of Applied Physics, 2014. **116**(19): p. 194306.
17. Fang, W. and S.N. Leung, *Elucidation of structure-to-property relationships of piezoresistive polymer-carbon nanotube nanocomposites.* Journal of Applied Physics, 2015. **118**(4): p. 044907.
18. Gong, S. and Z.H. Zhu, *On the mechanism of piezoresistivity of carbon nanotube polymer composites.* Polymer, 2014. **55**(16): p. 4136-4149.
19. Maxian, O., D. Pedrazzoli, and I. Manas-Zloczower, *Conductive polymer foams with carbon nanofillers – Modeling percolation behavior.* eXPRESS Polymer Letters, 2017. **11**(5): p. 406-418.
20. Behbahani, A.F., G.H. Motlagh, M. Ziaee, and G. Nikravan, *Electrical percolation behavior of carbon fiber and carbon nanotube polymer composite foams: Experimental and computational investigations.* Journal of Applied Polymer Science, 2015. **132**(42).
21. Thomassin, J.M., C. Pagnoulle, L. Bednarz, I. Huynen, R. Jerome, and C. Detrembleur, *Foams of polycaprolactone/MWNT nanocomposites for efficient EMI reduction.* Journal of Materials Chemistry, 2008. **18**(7): p. 792-796.
22. Yang, Y., M.C. Gupta, K.L. Dudley, and R.W. Lawrence, *Novel Carbon Nanotube−Polystyrene Foam Composites for Electromagnetic Interference Shielding.* Nano Letters, 2005. **5**(11): p. 2131-2134.
23. Park, D.H., Y.K. Lee, S.S. Park, C.S. Lee, S.H. Kim, and W.N. Kim, *Effects of hybrid fillers on the electrical conductivity and EMI shielding efficiency of polypropylene/conductive filler composites.* Macromolecular Research, 2013. **21**(8): p. 905-910.
24. Aghelinejad, M. and S.N. Leung, *Enhancement of thermoelectric conversion efficiency of polymer/carbon nanotube nanocomposites through foaming-induced microstructuring.* Journal of Applied Polymer Science, 2017. **134**(28): p. 45073.
25. Aghelinejad, M. and S.N. Leung, *Fabrication of open-cell thermoelectric polymer nanocomposites by template-assisted multi-walled carbon nanotubes coating.* Composites Part B: Engineering, 2018. **145**: p. 100-107.
26. Hu, R., B.A. Cola, N. Haram, J.N. Barisci, S. Lee, S. Stoughton, G. Wallace, C. Too, M. Thomas, A. Gestos, M.E.d. Cruz, J.P. Ferraris, A.A. Zakhidov, and R.H. Baughman, *Harvesting Waste Thermal Energy Using a Carbon-Nanotube-Based Thermo-Electrochemical Cell.* Nano Letters, 2010. **10**(3): p. 838-846.
27. Peng, C., S. Zhang, D. Jewell, and G.Z. Chen, *Carbon nanotube and conducting polymer composites for supercapacitors.* Progress in Natural Science, 2008. **18**(7): p. 777-788.
28. Sun, L., X. Wang, Y. Wang, and Q. Zhang, *Roles of carbon nanotubes in novel energy storage devices.* Carbon, 2017. **122**: p. 462-474.
29. Quang, N.H., M. Van Trinh, B.-H. Lee, and J.-S. Huh, *Effect of NH_3 gas on the electrical*

properties of single-walled carbon nanotube bundles. Sensors and Actuators B: Chemical, 2006. **113**(1): p. 341-346.

30. Leung, S.N., M.O. Khan, E. Chan, H.E. Naguib, F. Dawson, V. Adinkrah, and L. Lakatos-Hayward, *Synergistic effects of hybrid fillers on the development of thermally conductive polyphenylene sulfide composites.* Journal of Applied Polymer Science, 2013. **127**(5): p. 3293-3301.
31. Feng, W., M. Qin, and Y. Feng, *Toward highly thermally conductive all-carbon composites: Structure control.* Carbon, 2016. **109**: p. 575-597.
32. Biercuk, M.J., M.C. Llaguno, M. Radosavljevic, J.K. Hyun, A.T. Johnson, and J.E. Fischer, *Carbon nanotube composites for thermal management.* Applied Physics Letters, 2002. **80**(15): p. 2767-2769.
33. Gau, C., H.S. Ko, and H.T. Chen, *Piezoresistive characteristics of MWNT nanocomposites and fabrication as a polymer pressure sensor.* Nanotechnology, 2009. **20**(18): p. 185503.
34. Gong, S., D. Wu, Y. Li, M. Jin, T. Xiao, Y. Wang, Z. Xiao, Z. Zhu, and Z. Li, *Temperature-independent piezoresistive sensors based on carbon nanotube/polymer nanocomposite.* Carbon, 2018. **137**: p. 188-195.
35. Long, W. and J.L. Kenneth, *Wearable carbon nanotube-based fabric sensors for monitoring human physiological performance.* Smart Materials and Structures, 2017. **26**(5): p. 055018.
36. Yamada, T., Y. Hayamizu, Y. Yamamoto, Y. Yomogida, A. Izadi-Najafabadi, D.N. Futaba, and K. Hata, *A stretchable carbon nanotube strain sensor for human-motion detection.* Nature Nanotechnology, 2011. **6**: p. 296.
37. Kim, H. and S.J. Kim, *High toughness of bio-inspired multistrand coiled carbon nanotube yarn.* Carbon, 2018. **131**: p. 60-65.
38. Xue, L., W. Wang, Y. Guo, G. Liu, and P. Wan, *Flexible polyaniline/carbon nanotube nanocomposite film-based electronic gas sensors.* Sensors and Actuators B: Chemical, 2017. **244**: p. 47-53.
39. Hsieh, G.-W., F.M. Li, P. Beecher, A. Nathan, Y. Wu, B.S. Ong, and W.I. Milne, *High performance nanocomposite thin film transistors with bilayer carbon nanotube-polythiophene active channel by ink-jet printing.* Journal of Applied Physics, 2009. **106**(12): p. 123706.
40. Okamoto, M., P.H. Nam, P. Maiti, T. Kotaka, T. Nakayama, M. Takada, M. Ohshima, A. Usuki, N. Hasegawa, and H. Okamoto, *Biaxial Flow-Induced Alignment of Silicate Layers in Polypropylene/Clay Nanocomposite Foam.* Nano Letters, 2001. **1**(9): p. 503-505.
41. Haiyan, S., X. Zhen, and G. Chao, *Multifunctional, Ultra-Flyweight, Synergistically Assembled Carbon Aerogels.* Advanced Materials, 2013. **25**(18): p. 2554-2560.
42. Qin, Y., Q. Peng, Y. Ding, Z. Lin, C. Wang, Y. Li, F. Xu, J. Li, Y. Yuan, X. He, and Y. Li, *Lightweight, Superelastic, and Mechanically Flexible Graphene/Polyimide Nanocomposite Foam for Strain Sensor Application.* ACS Nano, 2015. **9**(9): p. 8933-8941.
43. Ameli, A., M. Nofar, C.B. Park, P. Pötschke, and G. Rizvi, *Polypropylene/carbon nanotube nano/microcellular structures with high dielectric permittivity, low dielectric loss, and low percolation threshold.* Carbon, 2014. **71**: p. 206-217.
44. Ding, H., Y. Guo, and S.N. Leung, *Development of thermally conductive polymer matrix*

composites by foaming-assisted networking of micron- and submicron-scale hexagonal boron nitride. Journal of Applied Polymer Science, 2016. **133**(4).
45. Cui, Y., C. Liu, S. Hu, and X. Yu, *The experimental exploration of carbon nanofiber and carbon nanotube additives on thermal behavior of phase change materials.* Solar Energy Materials and Solar Cells, 2011. **95**(4): p. 1208-1212.
46. Ghariniyat, P. and S.N. Leung, *Development of thermally conductive thermoplastic polyurethane composite foams via CO2 foaming-assisted filler networking.* Composites Part B: Engineering, 2018. **143**: p. 9-18.
47. Hao, D., G. Yanting, and L.S. Ning, *Development of thermally conductive polymer matrix composites by foaming-assisted networking of micron- and submicron-scale hexagonal boron nitride.* Journal of Applied Polymer Science, 2016. **133**(4).
48. Gong, S., Z. Zhu, and S. Meguid, *Carbon nanotube agglomeration effect on piezoresistivity of polymer nanocomposites.* Polymer, 2014. **55**(21): p. 5488-5499.
49. Khan, S.U., J.R. Pothnis, and J.-K. Kim, *Effects of carbon nanotube alignment on electrical and mechanical properties of epoxy nanocomposites.* Composites Part A: Applied Science and Manufacturing, 2013. **49**: p. 26-34.
50. Ayatollahi, M.R., S. Shadlou, M.M. Shokrieh, and M. Chitsazzadeh, *Effect of multi-walled carbon nanotube aspect ratio on mechanical and electrical properties of epoxy-based nanocomposites.* Polymer Testing, 2011. **30**(5): p. 548-556.
51. Maiti, S., N.K. Shrivastava, and B.B. Khatua, *Reduction of percolation threshold through double percolation in melt-blended polycarbonate/acrylonitrile butadiene styrene/multiwall carbon nanotubes elastomer nanocomposites.* Polymer Composites, 2013. **34**(4): p. 570-579.
52. Hu, N., Z. Masuda, C. Yan, G. Yamamoto, H. Fukunaga, and T. Hashida, *The electrical properties of polymer nanocomposites with carbon nanotube fillers.* Nanotechnology, 2008. **19**(21): p. 215701.
53. Fang, W., H.W. Jang, and S.N. Leung, *Evaluation and modelling of electrically conductive polymer nanocomposites with carbon nanotube networks.* Composites Part B: Engineering, 2015. **83**: p. 184-193.
54. Dai, W., J. Reimann, D. Hanaor, C. Ferrero, and Y. Gan, *Modes of wall induced granular crystallisation in vibrational packing.* Granular Matter, 2019. **21**(2).
55. Gauss, C.F., *Discussion of L. A. Seeber's book: Studies on the characteristics of positive ternary quadratic forms etc.* 1831.
56. Foroozani, B.A., M.G. Hashemi, Z. Morteza, and N. Goolia, *Electrical percolation behavior of carbon fiber and carbon nanotube polymer composite foams: Experimental and computational investigations.* Journal of Applied Polymer Science, 2015. **132**(42).
57. TabkhPaz, M., K. Parmar, A.M. Ali, and S. Park, *Effects of foaming through leaching on the electrical behavior of polystyrene/carbon nanotube composites.* Journal of Thermoplastic Composite Materials, 2014. **29**(6): p. 735-753.
58. Hu, N., Z. Masuda, G. Yamamoto, H. Fukunaga, T. Hashida, and J. Qiu, *Effect of fabrication process on electrical properties of polymer/multi-wall carbon nanotube nanocomposites.* Composites Part A: Applied Science and Manufacturing, 2008. **39**(5): p. 893-903.
59. Wang, C., V. Shaayegan, M. Ataei, F. Costa, S. Han, M. Bussmann, and C.B. Park, *Accurate*

theoretical modeling of cell growth by comparing with visualized data in high-pressure foam injection molding. European Polymer Journal, 2019. **119**: p. 189-199.

60. Balberg, I. and N. Binenbaum, *Cluster structure and conductivity of three-dimensional continuum systems.* Physical Review A, 1985. **31**(2): p. 1222-1225.
61. Hoang, L.T., S.N. Leung, and Z.H. Zhu, *Eliminating common biases in modelling the electrical conductivity of carbon nanotube–polymer nanocomposites.* Physical Chemistry Chemical Physics, 2018. **20**(19): p. 13118-13121.
62. Bauhofer, W. and J.Z. Kovacs, *A review and analysis of electrical percolation in carbon nanotube polymer composites.* Composites Science and Technology, 2009. **69**(10): p. 1486-1498.
63. Coleman, J.N., S. Curran, A.B. Dalton, A.P. Davey, B. McCarthy, W. Blau, and R.C. Barklie, *Percolation-dominated conductivity in a conjugated-polymer-carbon-nanotube composite.* Physical Review B, 1998. **58**(12): p. R7492-R7495.
64. Stauffer, D. and A. Aharony, *Introduction to percolation theory*. 1992: Taylor & Francis.
65. Sahimi, M., *Applications of percolation theory*. 1994: Taylor & Francis.
66. Wang, S., Z. Liang, B. Wang, and C. Zhang, *Statistical characterization of single-wall carbon nanotube length distribution.* Nanotechnology, 2006. **17**(3): p. 634.
67. Bohm, D., *Quantum Theory*. 1989, New York: New York: Dover.
68. Simmons, J.G., *Generalized Formula for the Electric Tunnel Effect between Similar Electrodes Separated by a Thin Insulating Film.* Journal of Applied Physics, 1963. **34**(6): p. 1793-1803.
69. Kim, D. and J. Nam, *Systematic analysis for electrical conductivity of network of conducting rods by Kirchhoff's laws and block matrices.* Journal of Applied Physics, 2018. **124**(21): p. 215104.
70. Balberg, I., *The physical fundamentals of the electrical conductivity in nanotube-based composites.* Journal of Applied Physics, 2020. **128**(20): p. 204304.
71. Willcox, K. and Q. Wang, *16.90 Computational Methods in Aerospace Engineering*. 2014, Massachusetts Institute of Technology: MIT OpenCourseWare.
72. Ono, Y., T. Aoki, and T. Ogasawara, *Mechanical and electrical properties of carbon-nanotube composites*, in *Proceedings of the 48th Conference on Structural Strength*. 2006: Japan. p. 141.
73. Grossiord, N., J. Loos, L. van Laake, M. Maugey, C. Zakri, C.E. Koning, and A.J. Hart, *High-Conductivity Polymer Nanocomposites Obtained by Tailoring the Characteristics of Carbon Nanotube Fillers.* Advanced Functional Materials, 2008. **18**(20): p. 3226-3234.
74. Ziegler, K.J., U. Rauwald, Z. Gu, F. Liang, W.E. Billups, R.H. Hauge, and R.E. Smalley, *Statistically Accurate Length Measurements of Single-Walled Carbon Nanotubes.* Journal of Nanoscience and Nanotechnology, 2007. **7**(8): p. 2917-2921.
75. Streit, J.K., S.M. Bachilo, A.V. Naumov, C. Khripin, M. Zheng, and R.B. Weisman, *Measuring Single-Walled Carbon Nanotube Length Distributions from Diffusional Trajectories.* ACS Nano, 2012. **6**(9): p. 8424-8431.
76. Parra-Vasquez, A.N.G., J.G. Duque, M.J. Green, and M. Pasquali, *Assessment of length and bundle distribution of dilute single-walled carbon nanotubes by viscosity measurements.* AIChE Journal, 2014. **60**(4): p. 1499-1508.

77. Vasileiou, A.A., M. Kontopoulou, H. Gui, and A. Docoslis, *Correlation between the Length Reduction of Carbon Nanotubes and the Electrical Percolation Threshold of Melt Compounded Polyolefin Composites.* ACS Applied Materials & Interfaces, 2015. **7**(3): p. 1624-1631.
78. Guo, J., N. Briggs, S. Crossley, and B.P. Grady, *A new finding for carbon nanotubes in polymer blends: Reduction of nanotube breakage during melt mixing.* Journal of Thermoplastic Composite Materials, 2016. **31**(1): p. 110-118.
79. Krause, B., R. Boldt, and P. Pötschke, *A method for determination of length distributions of multiwalled carbon nanotubes before and after melt processing.* Carbon, 2011. **49**(4): p. 1243-1247.
80. Xu, Z.-M., X.-L. Jiang, T. Liu, G.-H. Hu, L. Zhao, Z.-N. Zhu, and W.-K. Yuan, *Foaming of polypropylene with supercritical carbon dioxide.* The Journal of Supercritical Fluids, 2007. **41**(2): p. 299-310.
81. Ramesh, N.S., D.H. Rasmussen, and G.A. Campbell, *Numerical and experimental studies of bubble growth during the microcellular foaming process.* Polymer Engineering & Science, 1991. **31**(23): p. 1657-1664.
82. Wang, S., Y. Huang, C. Zhao, E. Chang, A. Ameli, H.E. Naguib, and C.B. Park, *Theoretical modeling and experimental verification of percolation threshold with MWCNTs' rotation and translation around a growing bubble in conductive polymer composite foams.* Composites Science and Technology, 2020. **199**: p. 108345.
83. Hearn, D., *Computer graphics with OpenGL*. 4th ed. ed, ed. M.P. Baker and W.R. Carithers. 2011, Boston: Prentice Hall.
84. Nanocyl, *PLASTICYL HDPE1501: High Density Polyethylene – carbon nanotubes masterbatches.* Technical Data Sheet, 2016. **V07**.
85. NOVA-Chemicals, *SCLAIR 2710 polyethylene resins.* Technical Data Sheet, 2013.
86. Nanocyl, *NANOCYL NC7000 multiwall carbon nanotubes.* Technical Data Sheet, 2016. **V08**.
87. ASTM-D792-20, *Standard Test Methods for Density and Specific Gravity (Relative Density) of Plastics by Displacement*. Vol. 08.01. 2020, West Conshohocken, PA: ASTM International.
88. Vipin, K. and S.N. P., *A process for making microcellular thermoplastic parts.* Polymer Engineering & Science, 1990. **30**(20): p. 1323-1329.
89. Ramirez, C., F.M. Figueiredo, P. Miranzo, P. Poza, and M.I. Osendi, *Graphene nanoplatelet/silicon nitride composites with high electrical conductivity.* Carbon, 2012. **50**(10): p. 3607-3615.
90. G.H., M., H. A.N., and T. M.R., *Improved through-plane electrical conductivity in a carbon-filled thermoplastic via foaming.* Polymer Engineering & Science, 2008. **48**(4): p. 687-696.
91. Krause, B., T. Villmow, R. Boldt, M. Mende, G. Petzold, and P. Pötschke, *Influence of dry grinding in a ball mill on the length of multiwalled carbon nanotubes and their dispersion and percolation behaviour in melt mixed polycarbonate composites.* Composites Science and Technology, 2011. **71**(8): p. 1145-1153.
92. Hu, N., Y. Karube, C. Yan, Z. Masuda, and H. Fukunaga, *Tunneling effect in a polymer/carbon nanotube nanocomposite strain sensor.* Acta Materialia, 2008. **56**(13): p. 2929-2936.

93. Bao, W.S., S.A. Meguid, Z.H. Zhu, Y. Pan, and G.J. Weng, *Effect of carbon nanotube geometry upon tunneling assisted electrical network in nanocomposites.* Journal of Applied Physics, 2013. **113**(23): p. 234313.
94. Bao, W.S., S.A. Meguid, Z.H. Zhu, Y. Pan, and G.J. Weng, *A novel approach to predict the electrical conductivity of multifunctional nanocomposites.* Mechanics of Materials, 2012. **46**: p. 129-138.
95. Gupta, T.K., M. Choosri, K.M. Varadarajan, and S. Kumar, *Self-sensing and mechanical performance of CNT/GNP/UHMWPE biocompatible nanocomposites.* Journal of Materials Science, 2018. **53**(11): p. 7939-7952.
96. Wang, N., Z. Xu, P. Zhan, K. Dai, G. Zheng, C. Liu, and C. Shen, *A tunable strain sensor based on a carbon nanotubes/electrospun polyamide 6 conductive nanofibrous network embedded into poly(vinyl alcohol) with self-diagnosis capabilities.* Journal of Materials Chemistry C, 2017. **5**(18): p. 4408-4418.
97. Myounggu, P., K. Hyonny, and P.Y. Jeffrey, *Strain-dependent electrical resistance of multi-walled carbon nanotube/polymer composite films.* Nanotechnology, 2008. **19**(5): p. 055705.
98. Huang, C.-T., C.-L. Shen, C.-F. Tang, and S.-H. Chang, *A wearable yarn-based piezo-resistive sensor.* Sensors and Actuators A: Physical, 2008. **141**(2): p. 396-403.
99. Li, J., P.-S. Wong, and J.-K. Kim, *Hybrid nanocomposites containing carbon nanotubes and graphite nanoplatelets.* Materials Science and Engineering: A, 2008. **483-484**: p. 660-663.
100. Merlin, T., K.A. D., and J. Neetha, *Investigations of the Influence of Compatibilizer and TiO2 Filler on the Properties of Thermoplastic Polyurethane/Polyolefins Blends.* International Journal of Research in Chemistry and Environment, 2012. **2**(3): p. 56-62.
101. Kim, H., A.A. Abdala, and C.W. Macosko, *Graphene/Polymer Nanocomposites.* Macromolecules, 2010. **43**(16): p. 6515-6530.
102. Kim, H., Y. Miura, and C.W. Macosko, *Graphene/Polyurethane Nanocomposites for Improved Gas Barrier and Electrical Conductivity.* Chemistry of Materials, 2010. **22**(11): p. 3441-3450.
103. Hoang, T.L., M. Aghelinejad, S.N. Leung, and Z.H. Zhu, *High density polyethylene/carbon nanotube nanocomposite foams: electrical conductivity and percolation threshold*, in *CSME international congress*. 2018: York University.
104. Zheng, Y., Y. Li, K. Dai, Y. Wang, G. Zheng, C. Liu, and C. Shen, *A highly stretchable and stable strain sensor based on hybrid carbon nanofillers/polydimethylsiloxane conductive composites for large human motions monitoring.* Composites Science and Technology, 2018. **156**: p. 276-286.
105. Duan, L., S. Fu, H. Deng, Q. Zhang, K. Wang, F. Chen, and Q. Fu, *The resistivity–strain behavior of conductive polymer composites: stability and sensitivity.* Journal of Materials Chemistry A, 2014. **2**(40): p. 17085-17098.
106. Liu, H., Y. Li, K. Dai, G. Zheng, C. Liu, C. Shen, X. Yan, J. Guo, and Z. Guo, *Electrically conductive thermoplastic elastomer nanocomposites at ultralow graphene loading levels for strain sensor applications.* Journal of Materials Chemistry C, 2016. **4**(1): p. 157-166.
107. Hoang, L.T., S.N. Leung, and Z.H. Zhu, *Strategies to Enhance Electrical Conductivity and Suppress Percolation Threshold of HDPE/MWCNT Nanocomposite through Supercritical*

Carbon Dioxide Foaming. Composites Part C: Open Access, 2020. **submitted**.

108. Hoang, T.L., K. McLellan, S.N. Leung, and Z.H. Zhu, *Piezoresistive polymer nanocomposites and their foams as smart sensing materials*, in *ANTEC conference*. 2019: Detroit.
109. Fang, C., J. Zhang, X. Chen, and G.J. Weng, *Calculating the Electrical Conductivity of Graphene Nanoplatelet Polymer Composites by a Monte Carlo Method.* Nanomaterials (Basel), 2020. **10**(6).
110. Matos, M.A.S., S.T. Pinho, and V.L. Tagarielli, *Predictions of the electrical conductivity of composites of polymers and carbon nanotubes by an artificial neural network.* Scripta Materialia, 2019. **166**: p. 117-121.